

NORTHWESTERN UNIVERSITY

Investigation of Stable Ca and Sr Isotopes as Proxies for Ocean Acidification in Deep Time:
Neoproterozoic, Permian-Triassic, and Cretaceous Case Studies

A DISSERTATION

SUBMITTED TO THE GRADUATE SCHOOL
IN PARTIAL FULFILLMENT OF THE REQUIREMENTS

for the degree

DOCTOR OF PHILOSOPHY

Field of Earth and Planetary Sciences

By

Jiuyuan Wang

EVANSTON, ILLINOIS

March 2021

© Copyright by Jiuyuan Wang 2021

All Rights Reserved

ABSTRACT

Investigation of Stable Ca and Sr Isotopes as Proxies for Ocean Acidification in Deep Time:
Neoproterozoic, Permian-Triassic, and Cretaceous Case Studies

Jiuyuan Wang

The studies presented in this dissertation integrate stable calcium (Ca) and radiogenic and stable strontium (Sr) isotope geochemistry to understand how the Earth system responds to significant perturbations in the global carbon cycle. The primary focus is on the effects of massive releases of volcanic CO₂ for ocean carbonate geochemistry and the incorporation of Ca and Sr isotopes into carbonate-bearing minerals. The main tools used in these studies are $\delta^{44/40}\text{Ca}$ and $\delta^{88/86}\text{Sr}$, which collectively represent recent advances in non-traditional stable isotope measurements. Analysis of $\delta^{88/86}\text{Sr}$ necessarily includes measurement of traditional radiogenic Sr isotope ratios ($^{87}\text{Sr}/^{86}\text{Sr}$). Large and rapid releases of CO₂ are expected to cause ocean acidification, which encompasses short-lived decreases in seawater pH, $[\text{CO}_3^{2-}]$, saturation states with respect to carbonate minerals, and carbonate burial. These changes exert fundamental controls on the fractionation of Ca and Sr isotopes between seawater and carbonate minerals, and thus, can be recorded by variations in the $\delta^{44/40}\text{Ca}$ and $\delta^{88/86}\text{Sr}$ signatures of carbonate sediments and rocks. Moreover, carbonate $^{87}\text{Sr}/^{86}\text{Sr}$ ratios are sensitive to changes in continental weathering driven by elevated atmospheric CO₂ levels, and transient mass-flux imbalances between weathering inputs and carbonate burial outputs can alter seawater $\delta^{44/40}\text{Ca}$ and $\delta^{88/86}\text{Sr}$ values. I investigate these mechanisms during three times in Earth history proposed as ocean acidification events. First, I present $\delta^{44/40}\text{Ca}$, $^{87}\text{Sr}/^{86}\text{Sr}$, and $\delta^{88/86}\text{Sr}$ records across the end-Permian mass extinction and argue that CO₂ release from the Siberian Traps Large Igneous Province (LIP) eruption, as well as

contemporaneous sea-level fall, enhanced carbonate weathering and lowered seawater $\delta^{44/40}\text{Ca}$ and $\delta^{88/86}\text{Sr}$ values. Next, I apply the same tools to shallow-water carbonates that formed in the mid-Pacific Ocean during the early Cretaceous Oceanic Anoxic Event (OAE) 1a, which is associated with eruption of the Ontong Java Plateau LIP. Precipitation rate-dependent changes in fractionation best explain the strong correlation between $\delta^{44/40}\text{Ca}$ and $\delta^{88/86}\text{Sr}$. The data suggest that biocalcifiers actively responded to changes in seawater carbonate chemistry and further reveal that shallow-water carbonates can preserve primary geochemical signals. Finally, I use the $\delta^{44/40}\text{Ca}$ - $^{87}\text{Sr}/^{86}\text{Sr}$ - $\delta^{88/86}\text{Sr}$ multi-proxy to decipher the “cap carbonate precipitation mystery” of the Neoproterozoic Marinoan deglaciation. to decipher the “cap carbonate precipitation mystery” of the Neoproterozoic Marinoan deglaciation. I argue that the basal cap dolostone rapidly precipitated in a freshwater-dominated environment and that the overlying limestone formed in a meltwater-seawater mixed environment. In conclusion, these studies provide critical new insights into how the Earth system responds to rapid CO_2 additions and demonstrate that the $\delta^{44/40}\text{Ca}$, $^{87}\text{Sr}/^{86}\text{Sr}$, and $\delta^{88/86}\text{Sr}$ proxies powerfully trace global carbon cycle perturbations throughout Earth history.

Acknowledgements

This work represents my attempts to synthesize and build upon the scientific perspectives of my advisors at Northwestern. My primary advisor, Bradley Sageman, deserves my deepest gratitude for his supportiveness and encouragement over the years. No matter what I encountered, he was the one I turned to and he was always there with solutions. He kept my mind on the big picture. I cherish his illuminating lectures, the Midwest field trip, and every moment we worked together. I am extremely grateful to my secondary advisor, Andrew Jacobson. He taught me to be a serious scientist. Over the past few years, he has become from an advisor to a mentor and friend, and without his guidance, this dissertation would not have been possible. Matthew Hurtgen offered me lots of invaluable advice and constructive feedbacks. Those ideas from him helped me clarify my thoughts and inspired me along the path.

I have greatly benefited from my interactions with graduate students in the department whom I consider to be both colleagues and friends. These people include Matt Jones, Ben Linzmeier, Luca Podrecca, Gabby Kitch, Nilou Sarvian, Annie Nelson, Greg Lehn, Grace Andrews, Eddie Brooks, Jimmy Neely, Jamie McFarlin, Pete Puleo, Howard Chen, Vivian Tang, Chijun Sun, Yuxi Suo, Hao Zhang, and Fei Wang. Thank you all for your supports, for our delightful conversations, and for your company. I thank Meagan Ankney, Grace Schellinger, and Andrew Masterson for their help and assistance in the laboratory. I also would like to thank all the staff in the departmental office: Lisa Collins, Richard Dodd, Robin Stark, and Tia Groce. I am indebted to my longtime friends, Ying Cui, Xin Gu, Yixin Dong, Shuang Zhang, Wei Cheng, Tony Tong, Fan Yang, and many others for their friendship and help. I am also very grateful to many Chinese students and scholars at Northwestern for their encouragement and for their trust during

my two-year tenure as the community leader. The names are too many to be listed here, and they have all greatly improved my time here at Northwestern.

To Michael Arthur, thank you for opening the door of science for me.

To my family, my mother and father, thank you for your unconditional love.

To my partner, Sin U Lam, thank you for helping me become a better person.

Table of Contents

Abstract.....	3
Acknowledgements.....	5
Table of Contents.....	7
List of Figures.....	8
Chapter 1 Introduction.....	9
Chapter 2 Coupled $\delta^{44/40}\text{Ca}$, $\delta^{88/86}\text{Sr}$, and $^{87}\text{Sr}/^{86}\text{Sr}$ geochemistry across the end-Permian mass extinction.....	20
Chapter 3 Stable Ca and Sr isotopes support volcanically-triggered biocalcification crisis during oceanic anoxic event 1a.....	63
Chapter 4 Ca and Sr isotopic constraints on the origin of the Marinoan cap carbonate.....	73
Chapter 5 Conclusions.....	86
Appendix I.....	89
Appendix II.....	103
Appendix III.....	118
References.....	131

List of Figures

Figure 2-1 Lithofacies map in South China and locations of the Meishan and Dajiang sections, south China.	23
Figure 2-2 Stratigraphic correlation of (A) $\delta^{13}\text{C}$, (B) $\delta^{44/40}\text{Ca}$, (C) $\delta^{88/86}\text{Sr}$, and (D) $^{87}\text{Sr}/^{86}\text{Sr}$ records across the latest Permian to the earliest Triassic from the Meishan and Dajiang sections, south China.	27
Figure 2-3 Comparison of $\delta^{44/40}\text{Ca}$ records across the Permian–Triassic transition from this study (colored) and published (grey) data for the (A) Meishan and (B) Dajiang sections.....	34
Figure 2-4 Elemental data of carbonate samples from the Meishan and Dajiang sections.....	40
Figure 2-5 Sequential leaching results for selected samples from Meishan (left) and Dajiang (right) sections.....	41
Figure 2-6 Cross-plots of (A) Sr/Ca vs $\delta^{44/40}\text{Ca}$ and (B) $\delta^{13}\text{C}$ vs $\delta^{44/40}\text{Ca}$	49
Figure 2-7 Cross-plot of $\delta^{44/40}\text{Ca}$ vs Sr concentrations (logarithmic scale).....	53
Figure 3-1 Paleogeographic location of Resolution Guyot during the Early Cretaceous and its $\delta^{13}\text{C}$, $\delta^{44/40}\text{Ca}$, $\delta^{88/86}\text{Sr}$, and $^{87}\text{Sr}/^{86}\text{Sr}$ records.....	65
Figure 3-2 Cross-plots of (A) $\delta^{44/40}\text{Ca}$ vs. [Sr] and (B) $\delta^{44/40}\text{Ca}$ vs. $\delta^{88/86}\text{Sr}$	68
Figure 3-3 Stratigraphic correlation of geochemical proxy data across OAE 1a.....	71
Figure 4-1 Lithofacies map of Namibia (A and B), locations of studied sections (shown in red circles), and stratigraphic column of the Otavi Group.....	75
Figure 4-2 Isotope geochemistry records of the Maieberg Formation from the Arbeitsgenot and Ombaatjie sections, Namibia.....	76
Figure 4-3 Cross-plots of $\delta^{44/40}\text{Ca}$ and $\delta^{88/86}\text{Sr}$ overlain with $^{87}\text{Sr}/^{86}\text{Sr}$ ratios.....	80
Figure 4-4 Compilation of $\delta^{13}\text{C}$ and $\delta^{44/40}\text{Ca}$ records from sections across the Otavi platform (A and B) and its foreslope (C and D).....	84

CHAPTER 1

INTRODUCTION

1.1 Introduction

Over the past 250 years, anthropogenic emissions of carbon dioxide (CO₂) have increased atmospheric CO₂ levels by over 40%, from a preindustrial level of ~280 ppmv (parts per million volume) to over 400 ppmv as of 2020. Proxy records and models suggest that CO₂ levels were at least this high in the geologic past (Breecker et al., 2010). However, the rate of increase happening now appears unprecedented (Zeebe et al., 2016) and is predicted to have severe consequences for future climate (Pachauri et al., 2014). Before the industrial revolution, the oceans were a source of CO₂ to the atmosphere (Zeebe and Wolf-Gladrow, 2001). In the modern-day, they have become a sink. Estimates indicate that seawater has taken up nearly a third of the anthropogenic carbon added to the atmosphere (Sabine et al. 2004; Sabine and Feely 2007). When CO₂ dissolves in seawater, it forms carbonic acid. The dissociation of carbonic acid decreases pH, [CO₃²⁻], and carbonate mineral saturation states. These processes collectively define ocean acidification (OA) – “the other CO₂ problem” (Turley 2005; Henderson 2006; Doney et al., 2009) and are widely expected to impact biocalcification (Doney et al., 2009).

The geologic record is imprinted with numerous catastrophic emissions of CO₂, mostly derived from the eruption of Large Igneous Provinces (LIPs). Ocean acidification during LIP eruptions may have caused mass extinctions and evolutionary turnovers throughout Earth history (cf. Kump et al., 2010; Hönisch et al., 2012). Therefore, “deep time” OA events provide a crucial analog for understanding future effects. Recent advances in mass spectrometry have made a variety of elemental and isotopic tools available for reconstructing seawater carbonate chemistry through

the analysis of geologic archives. Among these, increasing attention has focused on the high-precision analysis of stable calcium (Ca) and strontium (Sr) isotope abundance variations, as these elements form major components of carbonate-bearing minerals precipitated from seawater. Moreover, these elements and their isotopes behave similarly during most biogeochemical reactions, but a few key instances exist where strong discrimination occurs. These properties make stable Ca and Sr isotope ratios especially attractive tracers of Earth system phenomena. Stable Ca and Sr isotope ratios are expressed in delta notation, $\delta^{44/40}\text{Ca} = [({}^{44}\text{Ca}/{}^{40}\text{Ca})_{\text{sample}}/({}^{44}\text{Ca}/{}^{40}\text{Ca})_{\text{standard}} - 1] \times 1000$ and $\delta^{88/86}\text{Sr} = [({}^{88}\text{Sr}/{}^{86}\text{Sr})_{\text{sample}}/({}^{88}\text{Sr}/{}^{86}\text{Sr})_{\text{standard}} - 1] \times 1000$, respectively.

The Ca and Sr cycles intersect the C cycle through chemical weathering and carbonate precipitation, which are two key processes that regulate climate and seawater carbonate chemistry over geological timescales. Calcium occurs as six stable isotopes, ${}^{40}\text{Ca}$ (96.98%), ${}^{42}\text{Ca}$ (0.642%), ${}^{43}\text{Ca}$ (0.133%), ${}^{44}\text{Ca}$ (2.056%), ${}^{46}\text{Ca}$ (0.003%), and ${}^{48}\text{Ca}$ (0.182%). In the modern ocean, Ca has a concentration of 10.27 mmol/kg and a residence time of ~1.1 Myr (Broecker and Peng, 1982). Riverine, hydrothermal, and groundwater fluxes deliver Ca ions to seawater, while carbonate mineral formation removes them (Christina and DePaolo, 2000; Fantle, 2010; Fantle and Tipper, 2014; Milliman, 1993). Carbonate minerals preferentially incorporate lighter Ca isotopes (e.g., Gussone et al., 2003; Lemarchand et al., 2004; Marriott et al., 2004; Sime et al., 2005; Böhm et al., 2006). The fractionation factor ($\Delta^{44/40}\text{C}_{\text{carbonate-seawater}}$), which describes the apportionment of Ca isotopes between carbonate minerals and seawater is hypothesized to vary as function of several environmental parameters (Gusson et al., 2003; Fantle and Depaolo, 2007; Jacobson and Holmden, 2008; Tang et al., 2008; Fantle et al., 2015; Gussone et al., 2016; Higgins et al., 2018). Chief among these is $[\text{CO}_3^{2-}]$, which controls the rate of carbonate mineral precipitation. Numerous experiments and models concerning inorganic calcite have demonstrated that $\Delta^{44/40}\text{C}$ depends on

precipitation rate, with faster rates yielding lower $\delta^{44/40}\text{Ca}$ values and vice versa for slower rates (Tang et al., 2008; AlKhatib and Eisenhauer, 2017; Mejía et al., 2018). Calcium isotope fractionation during biomineralization is predicted to resemble that for inorganic calcite (Gussone et al., 2003). Some culturing studies suggest this is true (e.g., Mejía et al., 2018), but results from others are more ambiguous (e.g., Kısakürek et al., 2011). This dissertation was conducted partly to address the question whether kinetic isotope effects attributed to inorganic calcite also apply to natural biogenic carbonates.

Strontium traces calcium because Sr^{2+} readily substitutes for Ca^{2+} due to its identical charge and similar ionic radius, although carbonate mineral recrystallization and authigenic carbonate formation are two mechanisms that efficiently separate Sr from Ca (e.g., Brand and Veizer, 1980; Richter and Depaolo, 1993). Strontium occurs as four stable isotopes, ^{84}Sr (0.56%), ^{86}Sr (9.86%), ^{87}Sr (7.0%) and ^{88}Sr (82.58%). The isotope ^{87}Sr is also formed from the radioactive decay of ^{87}Rb , with a half-life of 4.88×10^9 years, indicating that the abundance of ^{87}Sr (conventionally expressed as the $^{87}\text{Sr}/^{86}\text{Sr}$ ratio) is higher in old, Rb-rich minerals and rocks. In the modern ocean, Sr has a concentration of Sr 90 $\mu\text{mol}/\text{kg}$ and a residence time of ~ 2.4 Myr (Beck et al., 2013). Because of its long residence time, the radiogenic Sr isotope composition of seawater is homogenous throughout the ocean basins. However, significant gradients can exist at continental margins, where river runoff mixes with seawater (e.g., Holmden et al., 1998; Peucker-Ehrenbrink and Fiske, 2019; Meknassi et al., 2020). Continental riverine discharge with elevated (more radiogenic) $^{87}\text{Sr}/^{86}\text{Sr}$ ratios is the largest source of Sr to seawater, followed by submarine hydrothermal inputs with lower (less radiogenic) $^{87}\text{Sr}/^{86}\text{Sr}$ ratios (Palmer and Edmond, 1989; Davis et al., 2003; Vance et al., 2009; Allegre et al., 2010; Beck et al., 2013; Peucker-Ehrenbrink and Fiske, 2019). Secular changes in the marine Sr isotope record largely reflect changes in the relative dominance of these

principal Sr inputs. While $^{87}\text{Sr}/^{86}\text{Sr}$ ratios are useful in assessing changes in Sr inputs to the ocean, they are ineffective for quantifying Sr output fluxes. This is because the normalization procedure employed to account for mass-fractionation during instrumental analysis also eliminates any naturally occurring mass-dependent fractionation (Faure and Mensing, 2005). The measurement of $\delta^{88/86}\text{Sr}$ therefore provides a new means to interrogate the Sr output flux by carbonate burial (Krabbenhöft et al., 2009; Krabbenhöft et al., 2010; Vollstaedt et al., 2014; Pearce et al., 2015; Andrews et al., 2016). Similar to the Ca isotope system, carbonate precipitation preferentially incorporates lighter Sr isotopes, with a fractionation factor that inversely correlates with precipitation rate (Fietzke and Eisenhauer, 2006; Halicz et al., 2008; Böhm et al., 2012; Raddatz et al., 2013; Stevenson et al., 2014). Therefore, the stable Sr isotope system should also be sensitive to changes in aqueous carbonate chemistry during OA. The $\delta^{44/40}\text{Ca}$ - $^{87}\text{Sr}/^{86}\text{Sr}$ - $\delta^{88/86}\text{Sr}$ multi-proxy enables us to comprehensively analyze the global Ca and Sr cycles and thereby understand interactions between continental weathering, carbonate burial rates, and ocean carbonate chemistry, as well as their relationships to environmental change across critical events in Earth's history.

The objective of this dissertation is to investigate the behavior of Ca and Sr isotopes during severe biological and environmental perturbations, as well as explore how the $\delta^{44/40}\text{Ca}$ - $^{87}\text{Sr}/^{86}\text{Sr}$ - $\delta^{88/86}\text{Sr}$ multi-proxy can help elucidate the responses of seawater chemistry and biocalcifiers to massive CO_2 injections. Theoretically, perturbations to input/output fluxes, changes in fractionation, local cycling processes, and diagenetic alteration can affect the stable Ca and Sr isotope composition of carbonate sediments and rocks. In this dissertation, I consider these factors by generating and examining $\delta^{44/40}\text{Ca}$, $^{87}\text{Sr}/^{86}\text{Sr}$, and $\delta^{88/86}\text{Sr}$ records across three turning points in Earth's history that are associated with large CO_2 releases: the Cretaceous Oceanic Anoxic Event

(OAE) 1a, the end-Permian mass extinction (EPME), and the Marinoan deglaciation. Chapter 2 analyzes the EPME records and evaluates how a variety of primary and secondary processes contributed to the observed patterns. It also summarizes the methodology for measuring $\delta^{44/40}\text{Ca}$, $^{87}\text{Sr}/^{86}\text{Sr}$, and $\delta^{88/86}\text{Sr}$ in the Radiogenic Isotope Geochemistry Clean Laboratory at Northwestern University. Chapter 3 presents the OAE1a study. Here, the data show that biocalcifiers adjusted to changing seawater carbonate chemistry in a way that directly mimics patterns for inorganic calcite. The results also challenge the widely-held hypothesis that platform carbonates are inherently susceptible to diagenetic overprinting. Chapter 4 focuses on the Marinoan deglaciation and illustrates how the $\delta^{44/40}\text{Ca}$ - $^{87}\text{Sr}/^{86}\text{Sr}$ - $\delta^{88/86}\text{Sr}$ multi-proxy can resolve primary versus secondary mechanisms of isotopic change. The data provide evidence for the primary origin of “cap dolostone” deposits and further support a conceptual model where the heterogeneous geochemistry of “cap carbonate sequences” is a direct consequence of water-mass mixing between meltwater runoff and seawater. The final chapter summarizes the main conclusions of this work. Two of these chapters are published. Chapter 2 and Appendix I were published in *Geochimica et Cosmochimica Acta* as Wang et al. (2019), and Chapter 3 and Appendix II were published in *Geology* as Wang et al. (2021).

1.2 Chapter 2: Coupled $\delta^{44/40}\text{Ca}$, $\delta^{88/86}\text{Sr}$, and $^{87}\text{Sr}/^{86}\text{Sr}$ geochemistry across the end-Permian mass extinction event

The marine Ca cycle can be represented by simple mass-balance equations. The change in the number of moles of Ca in the ocean (M_{Ca}) over time (t) is given by the equation:

$$\frac{dM_{\text{Ca}}}{dt} = F_{\text{r}}^{\text{Ca}} + F_{\text{h}}^{\text{Ca}} + F_{\text{g}}^{\text{Ca}} - \frac{M_{\text{Ca}}}{\tau_{\text{ca}}} \quad (1),$$

where F_{r}^{Ca} , F_{h}^{Ca} , and F_{g}^{Ca} refer to riverine, hydrothermal, and groundwater input fluxes (mol/yr)

and τ_{Ca} is the residence time of Ca in seawater (yr). The corresponding equation for the isotope composition of Ca in seawater (δ_{sw}^{Ca}) is given by the equation:

$$M_{Ca} * \frac{d\delta_{sw}^{Ca}}{dt} = F_r^{Ca}(\delta_r^{Ca} - \delta_{sw}^{Ca}) + F_h^{Ca}(\delta_h^{Ca} - \delta_{sw}^{Ca}) + F_g^{Ca}(\delta_g^{Ca} - \delta_{sw}^{Ca}) - \frac{M_{Ca}}{\tau_{Ca}}(\delta_c^{Ca} - \delta_{sw}^{Ca}) \quad (2),$$

where δ_r^{Ca} , δ_h^{Ca} , and δ_g^{Ca} represent the isotope composition of the riverine, hydrothermal, and submarine groundwater inputs, and δ_c^{Ca} is the isotope composition of marine carbonate.

The marine Sr cycle can be represented by a similar set of equations:

$$\frac{dM_{Sr}}{dt} = F_r^{Sr} + F_h^{Sr} + F_d^{Sr} - \frac{M_{Sr}}{\tau_{Sr}} \quad (3),$$

$$M_{Sr} \frac{d\left(\frac{{}^{87}\text{Sr}}{{}^{86}\text{Sr}}_{sw}\right)}{dt} = F_r^{Sr} \left(R_{86}^{87} \text{Sr}_r - R_{86}^{87} \text{Sr}_{sw} \right) + F_h^{Sr} \left(R_{86}^{87} \text{Sr}_h - R_{86}^{87} \text{Sr}_{sw} \right) + F_d^{Sr} \left(R_{86}^{87} \text{Sr}_d - R_{86}^{87} \text{Sr}_{sw} \right) \quad (4),$$

$$M_{Sr} * \frac{d\delta_{sw}^{Sr}}{dt} = F_r(\delta_r^{Sr} - \delta_{sw}^{Sr}) + F_h(\delta_h^{Sr} - \delta_{sw}^{Sr}) + F_d(\delta_d^{Sr} - \delta_{sw}^{Sr}) - \frac{M_{Sr}}{\tau_{Sr}}(\delta_c^{Sr} - \delta_{sw}^{Sr}) \quad (5),$$

where F_r^{Sr} , F_h^{Sr} , F_d^{Sr} , $R_{86}^{87} \text{Sr}_r$, $R_{86}^{87} \text{Sr}_h$, $R_{86}^{87} \text{Sr}_d$, δ_r^{Sr} , δ_h^{Sr} , and δ_d^{Sr} refer to riverine, hydrothermal, and diagenetic Sr fluxes (mol/yr) and their respective ${}^{87}\text{Sr}/{}^{86}\text{Sr}$ and $\delta^{88/86}\text{Sr}$ values. δ_c^{Sr} represents the $\delta^{88/86}\text{Sr}$ value of marine carbonate. The amount of Sr in the ocean, as well as seawater ${}^{87}\text{Sr}/{}^{86}\text{Sr}$ and $\delta^{88/86}\text{Sr}$ values, are represented by M_{Sr} , $R_{86}^{87} \text{Sr}_{sw}$, and δ_{sw}^{Sr} . In equations (2) and (5), $\delta_c^{Ca} - \delta_{sw}^{Ca}$ and $\delta_c^{Sr} - \delta_{sw}^{Sr}$ represent the stable calcium and strontium isotope fractionation factors between marine carbonate and seawater, expressed as $\Delta_{\text{carbonate-seawater}}^{Ca}$ and $\Delta_{\text{carbonate-seawater}}^{Sr}$.

Both Ca and Sr have long residence times in seawater. It is widely recognized that geologically-reasonable changes to the input fluxes can produce large variations in ${}^{87}\text{Sr}/{}^{86}\text{Sr}_{sw}$ because the end-members have appreciable isotopic contrast (Palmer and Edmond, 1992).

However, neither $\delta^{44/40}\text{Ca}_{\text{sw}}$ nor $\delta^{88/86}\text{Sr}_{\text{sw}}$ display this behavior because the stable isotopic end-members have much less contrast (Fantle and Tipper, 2014; Pearce et al., 2015). Calcium isotope observations suggest that input and output fluxes balance over very long timescales (Blättler and Higgins, 2017). However, OA-driven perturbations occur over short timescales (Honisch et al., 2012). Over timescales shorter than the residence times of Ca and Sr, imbalances between input and output fluxes are hypothesized to produce relatively large variations in $\delta^{44/40}\text{Ca}_{\text{sw}}$ and $\delta^{88/86}\text{Sr}_{\text{sw}}$. For example, a decrease in carbonate burial relative to weathering inputs can produce negative $\delta^{44/40}\text{Ca}_{\text{sw}}$ excursions (Payne et al., 2010, Blättler et al., 2011, Du Vivier et al., 2015). Nonetheless, the magnitude of the effect is model-dependent. The traditional “one-box” model equations presented above parameterize carbonate output as a function of seawater [Ca] only, but $[\text{CO}_3^{2-}]$ exerts greater control because $[\text{CO}_3^{2-}]$ significantly smaller (e.g., Komar and Zeebe, 2016). According to “Earth System Models” that track both seawater [Ca] and $[\text{CO}_3^{2-}]$, flux imbalances are minor and do not significantly affect $\delta^{44/40}\text{Ca}_{\text{sw}}$ (e.g., Komar and Zeebe, 2016).

Early diagenesis represents another mechanism that can produce Ca isotope variability in the carbonate rock record. It proceeds through two main pathways: recrystallization and neomorphism. Recrystallization describes the process where new calcite crystals form from existing ones, whereas neomorphism represents the transformation of aragonite to calcite. The slow recrystallization of calcite during early marine diagenesis negligibly fractionates Ca isotopes, which results in secondary calcite having higher $\delta^{44/40}\text{Ca}$ values than primary carbonate, especially when the recrystallization occurs under fluid-buffered (open system) conditions (Fantle and DePaolo, 2007; Fantle and Higgins, 2014; Higgins 2018). Similarly, Sr isotope fractionation approaches zero at chemical equilibrium (Böhm et al., 2012; Stevenson et al., 2014; AlKhatib and Eisenhauer, 2017). However, bulk carbonate $\delta^{88/86}\text{Sr}$ values are less susceptible to diagenetic

overprinting because recrystallizing calcite crystals expel Sr with minimal uptake from surrounding pore fluids (Richter and DePaolo, 1988; Richter and Liang, 1993; Voigt et al., 2015). Different degrees of neomorphism can also affect bulk carbonate $\delta^{44/40}\text{Ca}$ values because aragonite and calcite have different fractionation factors (e.g., Jost et al., 2015; Gussone et al., 2016; Lau et al., 2017).

The end-Permian mass extinction provides an exciting opportunity to examine these and other complexities, as it represents a time period in Earth history characterized by severe biological and environmental perturbations, including a major mass extinction, flood basalt volcanism, ocean acidification, and sea level fluctuations. The second chapter of this dissertation reports high-resolution, high-precision $\delta^{44/40}\text{Ca}$, $\delta^{88/86}\text{Sr}$, and $^{87}\text{Sr}/^{86}\text{Sr}$ records spanning the Permian-Triassic boundary (PTB) from the Meishan and Dajiang carbonate successions in south China. Dajiang displays negative $\delta^{44/40}\text{Ca}$ and $\delta^{88/86}\text{Sr}$ excursions and invariant $^{87}\text{Sr}/^{86}\text{Sr}$ ratios in the <60 kyr timeframe between the main extinction horizon and the PTB. The Meishan $\delta^{44/40}\text{Ca}$ and $\delta^{88/86}\text{Sr}$ records are generally shifted to higher values and display both synchronous and asynchronous trends relative to Dajiang. In addition, $^{87}\text{Sr}/^{86}\text{Sr}$ ratios at Meishan are significantly elevated and do not define a clear secular pattern. We reconcile diverse conceptual models for the dataset with the aid of supporting elemental and isotope measurements (e.g., Sr/Ca, $\delta^{13}\text{C}$, and $\delta^{18}\text{O}$), as well as sequential leaching experiments. The combined body of evidence indicates that Dajiang sediments experienced recrystallization and neomorphism under rock-buffered conditions that preserved primary signals. In contrast, the Meishan records display influences from both primary and secondary processes, including local differences in fractionation, fluid-buffered early marine diagenesis, and late stage diagenetic overprinting. The three isotopic records for Dajiang, and to some extent, the $\delta^{44/40}\text{Ca}$ and $\delta^{88/86}\text{Sr}$ records for Meishan, preserve information about the

geochemistry of end-Permian seawater. We find that enhanced weathering of shelf carbonates during sea level fall provides the best explanation for rapidly decreasing seawater $\delta^{44/40}\text{Ca}$ and $\delta^{88/86}\text{Sr}$ values without affecting $^{87}\text{Sr}/^{86}\text{Sr}$ ratios.

1.3 Chapter 3: Stable Ca and Sr isotopes support volcanically-triggered biocalcification crisis during Oceanic Anoxic Event 1a

Isotope fractionation during primary carbonate mineral formation also controls $\delta^{44/40}\text{Ca}$ and $\delta^{88/86}\text{Sr}$ signals archived in the rock record. Nearly all models assume that fractionation factors are invariant, but a wide variety of observations suggest that they vary as a function of carbonate precipitation rates (e.g., Gussone et al., 2003; Tang et al., 2008; Böhm et al., 2012; Mejía et al., 2018). In general, elevated CO_2 is expected to decrease precipitation rates, diminish the magnitude of Ca and Sr isotope fractionation, and yield higher carbonate $\delta^{44/40}\text{Ca}$ and $\delta^{88/86}\text{Sr}$ values. This chapter examines stable Ca and Sr isotope ratios (and radiogenic Sr isotope ratios) for biogenic carbonate collected from a core drilled in Resolution Guyot, mid-Pacific Ocean (IODP Leg 143 Hole 866a). The samples span OAE 1a, which is hypothesized as an ancient OA event. The measured section of the core comprises ~1200 m of shallow-water carbonate facies spanning the Barremian (~126 Ma) to the Albian (~99 Ma; Jenkyns and Wilson, 1999). The rocks comprise cyclic packstone–wackestones and oolitic/peloidal grainstones. At this point in Earth history, Resolution Guyot was in the southern tropical Pacific (Blakey, 2010). The depositional environment characterizes an open marine carbonate platform that was minimally influenced by coastal processes.

The $\delta^{44/40}\text{Ca}$ and $\delta^{88/86}\text{Sr}$ secular trends mimic each other. $\delta^{44/40}\text{Ca}$ range from -0.74‰ to -1.16‰ with an average of -0.94‰, which represents the upper range for primary carbonate producers (Gussone et al., 2016) and bulk marine sediments (Fantle and Tipper, 2014). $\delta^{88/86}\text{Sr}$

range from 0.25‰ to 0.37‰, with an average of 0.29‰. Both records exhibit positive shifts that begin before OAE 1a and negative shifts immediately after the OAE 1a interval. The $^{87}\text{Sr}/^{86}\text{Sr}$ record begins at ~ 0.70751 and gradually decreases to a minimum of 0.70727. It is consistent with the global record (Paull et al., 1995) but markedly differs from the $\delta^{44/40}\text{Ca}$ and $\delta^{88/86}\text{Sr}$ records. $\delta^{44/40}\text{Ca}$ and [Sr], as well as $\delta^{44/40}\text{Ca}$ and $\delta^{88/86}\text{Sr}$, strongly correlate, and the slopes of their regression lines are identical to those predicted for kinetic control (Tang et al., 2008; Böhm et al., 2012). The results of this study demonstrate that variable mass-dependent fractionation rather than end-member mixing dominated the isotopic relationship between carbonates and seawater. The results also suggest that models describing the fractionation of Ca and Sr isotopes during inorganic calcite precipitation to some degree apply to biologically-produced calcite. Positive $\delta^{44/40}\text{Ca}$ and $\delta^{88/86}\text{Sr}$ shifts during OAE 1a are consistent with reduced precipitation rates, and negative shifts after OAE 1a point to biological compensation as the dampening mechanism to OA (e.g., Boudreau, 2018). In general, variable mass-dependent fractionation appears to reflect the dynamic interplay between LIP eruptions and biocalcification feedbacks.

1.4 Chapter 4: Ca and Sr isotopic constraints on the origin of the Marinoan cap carbonate

Finally, in this chapter, I applied the $\delta^{44/40}\text{Ca}$ - $^{87}\text{Sr}/^{86}\text{Sr}$ - $\delta^{88/86}\text{Sr}$ multi-proxy to one of the most dramatic events in Earth's history – the Marinoan deglaciation – with the aim of better understanding the origin of the “cap carbonate” sequence. The cap carbonate consists of a basal cap dolostone unit overlain by limestone (e.g., Hoffman et al., 2011). The cap carbonates have received considerable attention, but the precipitation mechanism remains poorly understood (e.g., Hoffman et al., 2002). Numerous models have been proposed, but none explain all sedimentary and geochemical observations (e.g., Yu et al., 2020). The models generally fall into two categories: primary precipitation and diagenetic alteration. The primary model is supported by abundant

observations of well-preserved primary structures (e.g., peloidal dolarenite, Kennedy, 1996; Hoffman et al., 2011). The diagenetic model is supported by the presence of aragonite fan pseudomorphs and dolomitized vents (Gammon et al., 2012). Recently, Ahm et al. (2019) utilized $\delta^{44/40}\text{Ca}$ and Mg isotopes ($\delta^{26}\text{Mg}$) to identify different diagenetic regimes (fluid- versus rock-buffered) and argued that aragonite was the precursor mineral of the cap dolostone and that dolomitization occurred during early diagenesis. The studies described in Chapters 2 and 3 reveal that $\delta^{88/86}\text{Sr}$ can test these hypotheses. Thus, we measured $\delta^{44/40}\text{Ca}$, $\delta^{88/86}\text{Sr}$, and $^{87}\text{Sr}/^{86}\text{Sr}$ in two Namibian cap carbonate sections. Both sections mark negative excursions in $\delta^{44/40}\text{Ca}$ and $\delta^{88/86}\text{Sr}$, and positive shifts in $^{87}\text{Sr}/^{86}\text{Sr}$ ratios, within the Keilberg cap dolostone. However, non-trivial differences still exist in the whole of the cap carbonate sequence. One cap dolostone (Arbeitsgenot section) gives the “kinetic slope” also measured for the OAE1a rocks analyzed in Chapter 3, whereas the other (Ombaatjie section) does not. The overlying limestone in both sections shows large variations in $\delta^{88/86}\text{Sr}$ but minimal variations in $\delta^{44/40}\text{Ca}$. These patterns can be explained by a combination of freshwater-seawater mixing and kinetic isotope effects during carbonate formation. These results do not preclude diagenetic overprinting, but it is not needed to explain the dataset. Overall, the data suggest that deposition of the cap carbonate sequence involved several processes, including intensified continental weathering, enhanced riverine alkalinity inputs to shelf environments, and mixing between meltwater and seawater. Water-mass mixing can explain the strong spatial heterogeneity commonly observed in cap carbonate sequences. These findings also have implications for understanding $\delta^{13}\text{C}$ excursions within the cap dolostones.

CHAPTER 2

COUPLED $\delta^{44/40}\text{Ca}$, $\delta^{88/86}\text{Sr}$, AND $^{87}\text{Sr}/^{86}\text{Sr}$ GEOCHEMISTRY ACROSS THE END-PERMIAN MASS EXTINCTION EVENT

This chapter was published in Geochimica et Cosmochimica Acta: Wang, J., Jacobson, A.D., Zhang, H., Ramezani, J., Sageman, B.B., Hurtgen, M.T., Bowring, S.A., Shen, S.-Z., 2019. Coupled $\delta^{44/40}\text{Ca}$, $\delta^{88/86}\text{Sr}$, and $^{87}\text{Sr}/^{86}\text{Sr}$ geochemistry across the end-Permian mass extinction event. Geochim. Cosmochim. Acta 262, 143–165.

2.1 Introduction

Calcium and stable strontium isotope ratios ($\delta^{44/40}\text{Ca}$ and $\delta^{88/86}\text{Sr}$) offer potential to trace the drivers and regulators of environmental change in deep time. Recent Ca isotope studies examining modern marine systems and ancient carbonate rocks have revealed a rich array of mechanisms that control primary sedimentary signals and impact their preservation before, during, and after lithification (e.g., De La Rocha and DePaolo, 2000; Fantle and DePaolo, 2005; Farkaš et al., 2007; Sime et al., 2007; Blättler et al., 2012; Holmden et al., 2012; Fantle and Higgins, 2014; Du Vivier et al., 2015; Griffith et al., 2015; Gussone et al., 2016; Lau et al., 2017; Higgins et al., 2018; Ahm et al., 2019; Wei et al., 2019). Analysis of stable Sr isotope ratios can help refine understanding of biogeochemical records because Ca and Sr behave similarly during most reactions, experience complementary isotopic fractionation phenomena, and share mass fluxes that intersect the global C cycle (e.g., Fietzke and Eisenhauer, 2006; Halicz et al., 2008; Krabbenhöft et al., 2009, 2010; Böhm et al., 2012; Stevenson et al., 2014; Vollstaedt et al., 2014; Voigt et al., 2015; AlKhatib et al., 2017a, b; Andrews et al., 2016; Andrews and Jacobson, 2017).

Carbonate successions spanning the end-Permian are ideal for further developing the $\delta^{44/40}\text{Ca}$ and $\delta^{88/86}\text{Sr}$ proxies. The end-Permian mass extinction (ca. 251.9 Ma) represents the most significant loss of biodiversity during the Phanerozoic Eon (Erwin, 1994; Clapham and Payne,

2011; Shen et al., 2011; Burgess et al., 2014). High-precision geochronological measurements applied to rocks in China indicate that the event occurred rapidly, with the main phase in the latest Permian decimating ~60% of all marine species within 60 kyr (Burgess et al., 2014) or shorter (Shen et al., 2019). Eruption of the Siberian Traps may have triggered the mass extinction (e.g., Svensen et al., 2009; Payne and Clapham, 2012; Burgess et al., 2017), along with several other perturbations expected to impact the cycling of Ca and Sr isotopes, including changes in seawater circulation (Knoll et al., 1996), widespread anoxia (Wignall and Twitchett, 1996), climate warming (Sun et al., 2012), and ocean acidification (Clapham and Payne, 2011). The end-Permian also coincides with one of the largest marine regressions in Earth history (Forney, 1975; Haq et al., 1987; Haq and Schutter, 2008; Campbell et al., 1992).

Pronounced negative carbon isotope ($\delta^{13}\text{C}$) excursions globally recorded in bulk carbonate and organic matter deposited during the end-Permian point to severe C cycle disruption, presumably due to CO_2 injection from the Siberian Traps (e.g., Grice et al., 2005; Payne and Kump, 2007; Xie et al., 2007; Svensen et al., 2009; Korte and Kozur, 2010; Shen et al., 2011; Erwin, 2015; Clapham and Renne, 2019). End-Permian carbonate rocks and hydroxyapatite microfossils also display contemporaneous negative $\delta^{44/40}\text{Ca}$ excursions, although their exact interpretation remains equivocal. Pioneering studies by Payne et al. (2010) and Hinojosa et al. (2012) attributed the negative excursions to an input/output flux imbalance resulting from reduced carbonate deposition during ocean acidification, but numerical modeling advances have challenged whether significant imbalances in the marine Ca cycle can occur (Komar and Zeebe, 2016). More recent studies have variably attributed the Ca isotope composition of end-Permian rocks to local changes in the mineralogy of carbonate sediment (Silva-Tamayo et al., 2018) and diagenetic overprinting (Lau et al., 2017). To date, no studies have measured $\delta^{88/86}\text{Sr}$ values for end-Permian rocks.

Here, we report high-precision Ca and stable Sr isotope records for two well-documented marine carbonate sections in China that span the latest Permian to earliest Triassic. High-precision methods are particularly advantageous for evaluating small isotopic variations in context with larger ones to constrain how sources of heterogeneity manifest in the rock record across a spectrum of spatial and temporal scales. Our study also includes radiogenic Sr isotope ratios ($^{87}\text{Sr}/^{86}\text{Sr}$) determined as part of the stable Sr isotope technique (Krabbenhöft et al., 2009; Andrews et al., 2016), complementary elemental and stable isotope data (e.g., Sr/Ca, $\delta^{13}\text{C}$, and $\delta^{18}\text{O}$), and leaching experiments designed to examine the fidelity of the proxies. Our effort to interpret the dataset focuses on testing diverse hypotheses that best explain similarities and differences between the Meishan and Dajiang $\delta^{44/40}\text{Ca}$, $\delta^{88/86}\text{Sr}$, and $^{87}\text{Sr}/^{86}\text{Sr}$ records, with an emphasis on discriminating primary and secondary signals.

2.2 Geological background

We examined two sections located in south China (Figure 2-1). The Meishan section, the Global Stratotype Section and Point (GSSP) for the Permian-Triassic boundary (PTB), lies within the Lower Yangtze Basin and was located northeast of the paleo-Tethys sea at $\sim 20^\circ\text{N}$ paleolatitude (e.g., Yin et al., 2001). The late Permian-early Triassic Meishan sequence developed in an intra-platform depression (Yin et al., 2001; Zheng et al., 2013). The Dajiang section represents an isolated shallow marine carbonate platform that formed as part of the Great Bank of Guizhou in the Nanpanjiang Basin. The site lies southeast of the Yangtze Block and was located $\sim 12^\circ\text{N}$ during early Triassic time (Lehrmann et al., 2003).

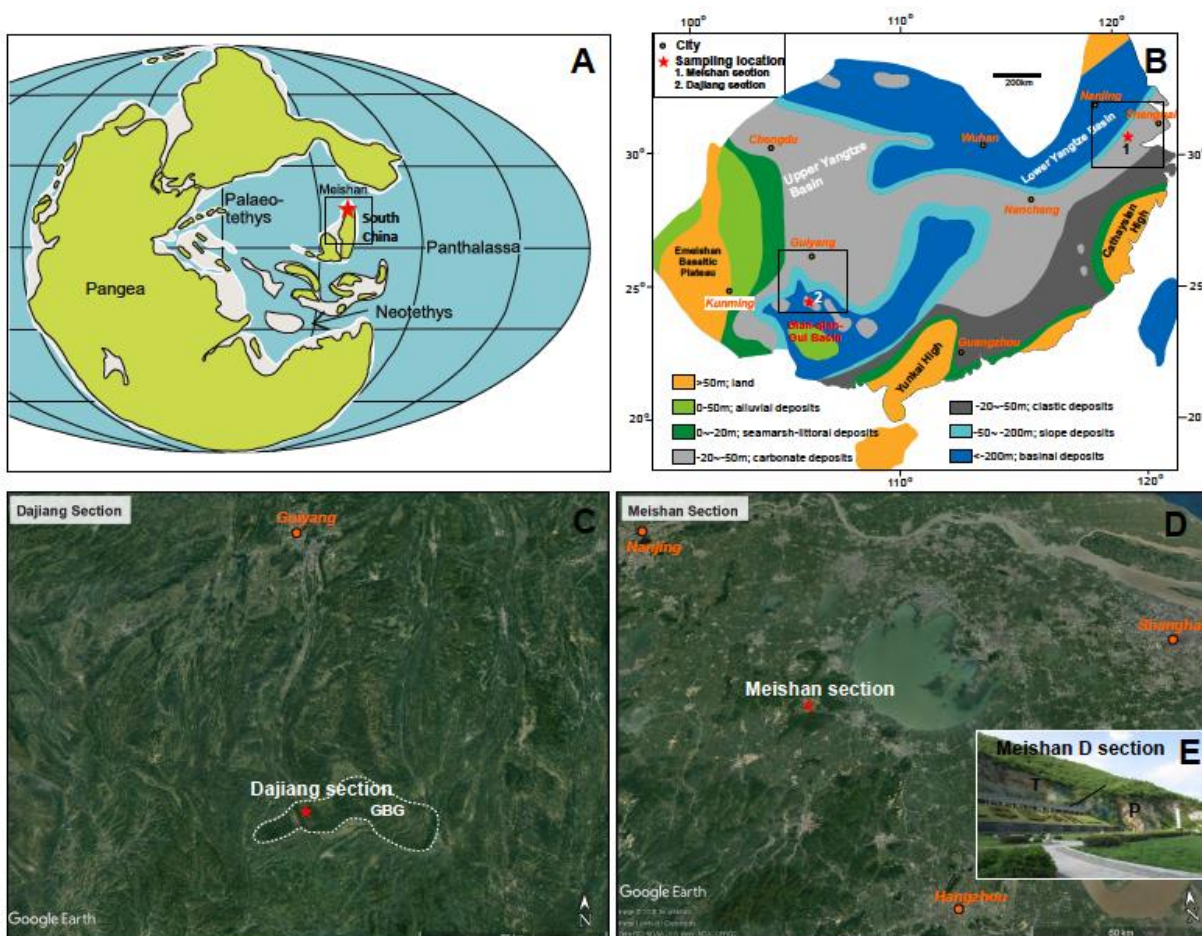


Figure 2-1 (A) Paleogeographic location of South China during the Permian–Triassic transition (modified from Ziegler et al., 1997); (B) Lithofacies map in South China showing the current location of the Meishan and Dajiang sections (after Shen et al., 2011; Zhang et al., 2016); (C) Modern location of the Dajiang section, GBG = Great Bank of Guizhou; (D) Modern location of the Meishan section; (E) Picture of Meishan D section.

2.2.1 Meishan

The lithological and paleontological records of the Meishan section have been studied extensively (e.g., Zhang et al., 1996; Yin et al., 2001; Cao and Zheng, 2007, 2009; Zhao and Tong, 2010; Zheng et al., 2013) and recently reviewed (Chen et al., 2015). The Permian-Triassic (P-Tr) succession at Meishan comprises the latest Changhsingian Changhsing Formation (Fm.) (Beds 2-24) and the early Griesbachian Yinkeng Fm. (Beds 25-60). The Changhsing Fm. is composed of

skeletal packstones and wackestones, while the Yinkeng Fm. mostly contains dark calcareous mudstone, micrite, and muddy limestone (Yin et al., 2001; Zheng et al., 2013). In this study, 49 samples from upper Bed 24 (Changhsing Fm.) to lower Bed 29 (Yinkeng Fm.) were collected (Figure 2-2). Bed 24e is a dark grey bioclastic wackestone containing a diverse assemblage of Ca-bearing fossils, including foraminifers, brachiopods, ammonites, bryozoans, gastropods, macroalgae, ostracods, rugose corals, and calcareous sponges (Chen et al., 2015). However, the abundance and diversity of fossils dramatically decrease toward the uppermost part of Bed 24e, indicating the first biotic perturbation associated with the mass extinction (Jin et al., 2000; Song et al., 2012). Bed 24e displays vertical burrows and wavy laminae, with the depositional environment interpreted as a lowstand platform margin near a fair-weather wave base (Zhang et al., 1996; Yin et al., 2014). Bed 25 is a white-grey altered volcanic ash layer consisting of illite-montmorillonite, with small amounts of gypsum, quartz, and pyrite, but no fossils (Shen et al., 2007; Shen et al., 2012). High-precision U-Pb zircon geochronology of the interstratified ash beds has established a detailed chronostratigraphy of the P-Tr transition at Meishan (Burgess et al., 2014), which provides the necessary time control for this study. Accordingly, Bed 25 has an age of 251.941 ± 0.037 Ma (2σ internal uncertainty) and is widely calibrated as the onset of the main phase of the mass extinction (Shen et al., 2011), hereafter designated as “EXT.” This bed grades upward into black calcareous mudstone composing Bed 26, which also includes higher concentrations of total organic carbon (wt.% TOC) and total inorganic carbon (wt.% CaCO_3). Fossil fragments are extremely rare in the lower parts of Bed 26 but increase upward. The very top of Bed 26 includes fragments of foraminifers, ostracods, echinoids, bryozoans, and brachiopods (Chen et al., 2015). A lack of evidence for calcareous algae, rugose corals, sponges, and radiolarians suggests a significant extinction and shift in species diversity (Jin et al., 2000; Shen

et al., 2011; Song et al., 2012, 2015; Wang et al., 2014). The fine-grained, clay-rich lithofacies with abundant framboidal pyrite indicate that Bed 26 was deposited in a low-energy anoxic environment, consistent with rising sea level upsection (Shen et al., 2007; Yin et al., 2014; Chen et al., 2015). A substantial lithologic change occurs in Bed 27, which comprises packstone to wackestone and also displays a reoccurrence of foraminifers, brachiopods, echinoids, and ostracods (Chen et al., 2015). Petrological analyses show enlarged crystal sizes, moldic porosity, and concave-convex boundaries between grains, consistent with a series of dissolution-recrystallization processes (Li and Jones, 2017). Detailed elemental analyses further show increasing dolomitization toward the upper part of Bed 27. The first appearance datum (FAD) of the conodont *Hindeodus parvus*, defined as the PTB, occurs in the middle of Bed 27 (Yin et al., 2001). Bed 28 is a yellow volcanic ash layer having a mineral composition similar to Bed 25, with no fossils documented, and has been dated at 251.880 ± 0.031 Ma (Burgess et al., 2014). Bed 29 comprises wackestone to micrite and muddy limestone with very rare fossil fragments, and its base may represent the end of the mass extinction at Meishan (Shen et al., 2011; Burgess et al., 2014) or another episode of mass extinction (Song et al., 2013). Bed 29 contains abundant pyrite framboids and laminated stratification, consistent with a transition from slope to basin facies due to continued sea level rise and transgression (Zheng et al., 2013; Yin et al., 2014; Chen et al., 2015).

2.2.2 Dajiang

Unlike the condensed section of Meishan, the P-Tr succession at Dajiang is an expanded carbonate succession comprising the Wuchiaping Fm. (Wuchiapingian to Changhsingian) and the Daye Fm. (Changhsingian to Griesbachian). In this study, we collected 67 samples spanning 80 m from the uppermost Wuchiaping Fm. to the lowermost Daye Fm., with a focus on the P-Tr

transition. The upper Permian Wuchiaping Fm. consists of thick skeletal packstone. The fossil assemblage is similar to that of the Changhsing Fm. (Bed 24) at Meishan, including (in order of decreasing abundance): foraminifers, brachiopods, bivalves, gastropods, echinoids, crinoids, dasycladacean algae, and rugose corals (Lehrmann et al., 2003; Payne et al., 2006). However, large skeletal fossils become absent at the top of the Wuchiaping Fm., indicating a sudden decrease in the diversity of marine taxa correlatable to the EXT level in Bed 25 of the Meishan section (Lehrmann et al., 2003; Payne et al., 2006). The Daye Fm. overlies the Wuchiaping Fm. with ~20 m of microbialite across a sharp contact. The deposition of the Wuchiaping Fm. likely occurred within a lowstand system tract, and the basal contact of the Daye Fm. has been interpreted as a sequence boundary (Yin et al., 2014). The microbialite has a distinctive stromatolitic structure and consists of irregular arches and black patches of microbial carbonate generating cavities filled with dark micrite and lime mud (Lehrmann et al., 2003). Unlike the reoccurrence of some fossils at the top of Bed 26 at Meishan, this microbialite biostrome exhibits distinct microfossil assemblages (similar to *Renalcis*, Lehrmann et al., 2003) with no recognizable Permian macrofossils. Biostratigraphic analysis has identified the FAD of *Hindeodus parvus* within the microbialite (Lehrmann et al., 2003), thus correlating with the PTB at Meishan. Several layers of skeletal packstone with variable thicknesses overlie the microbialite. The packstone contains gastropods and bivalve fossils (Lehrmann et al., 2003). The lithofacies of Dajiaing include a large fraction of micritic matrix and microcrystalline cement, indicating progressive recrystallization (Yang et al., 2011; Kershaw et al., 2012; Lehrmann et al., 2015; Lau et al., 2017). The microbialite shows a pervasive recrystallized texture. Enlarged anhedral to subhedral grains merge together, forming larger crystals with concave-convex boundaries. Some fine-grained muds are intimately intermixed with individual crystals of calcite showing a progressive coarsening to micrite (Yang

et al., 2011; Lehrmann et al., 2015). In the absence of direct age constraints, chemostratigraphic mapping of the well-calibrated Meishan $\delta^{13}\text{C}$ record onto the Dajiang $\delta^{13}\text{C}$ record, together with assumptions about the sediment accumulation rate at Dajiang, provides the necessary temporal framework for correlating the two sections (see Section 2.4.3; Figure 2-2).

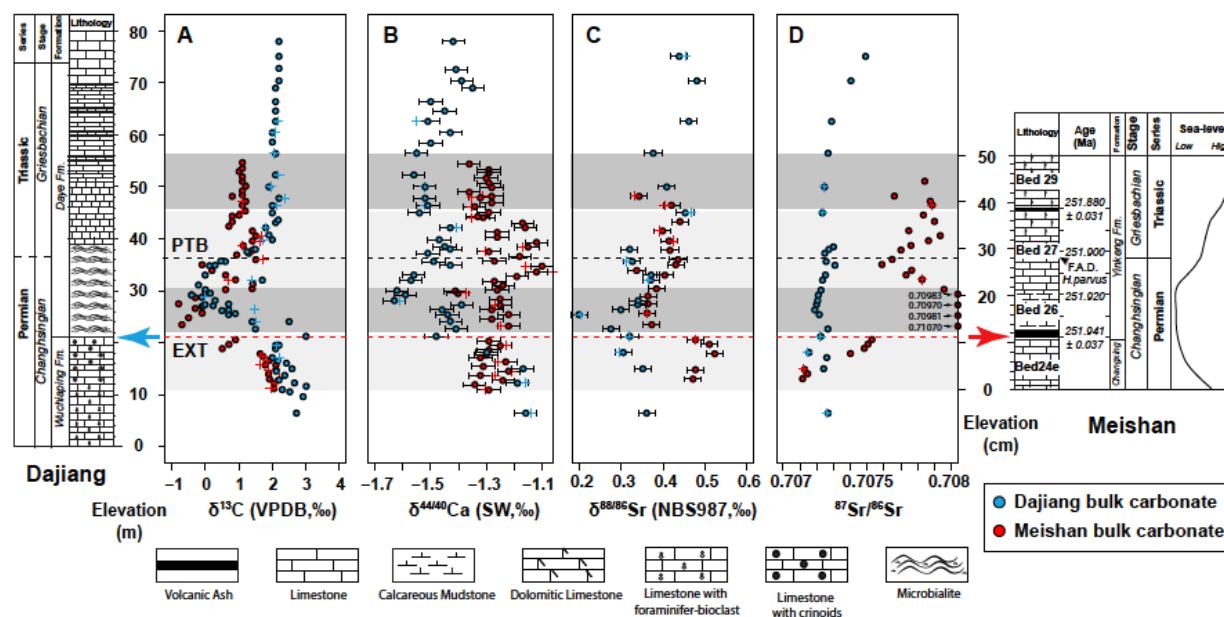


Figure 2-2 Stratigraphic correlation of (A) $\delta^{13}\text{C}$, (B) $\delta^{44/40}\text{Ca}$, (C) $\delta^{88/86}\text{Sr}$, and (D) $^{87}\text{Sr}/^{86}\text{Sr}$ records across the latest Permian to the earliest Triassic from the Meishan and Dajiang sections, south China (the data series are superimposed – note different y-axis scales for the two different sections). Filled circles denote original measurements, and crosses denote duplicates (see Section 2.3.3). At Meishan, the FAD of *Hindeodus parvus* defines the Permian-Triassic Boundary. The calculated age of the PTB is based on Burgess et al. (2014), and the age extrapolation assumes a constant sedimentation rate of 0.37 cm/kyr (Burgess et al., 2014). The correlation between Meishan and Dajiang is based on the extinction datum (Bed 25 at Meishan and the base of the microbialite at Dajiang) and $\delta^{13}\text{C}$ chemostratigraphy (see Section 2.4.3). The sea level curve is modified from Wignall and Hallam (1993).

2.3 Methodology

2.3.1 Sample Preparation

A total of 116 samples from the Meishan ($n = 49$) and Dajiang ($n = 67$) sections were drilled into powders with a low-speed, stationary micro-drill equipped with a 0.7 mm stainless

steel bit. Drilling sites were carefully selected to sample the bulk matrix of carbonate and avoid visible bioclasts and cements. For each sample, approximately 200 mg of powder was dissolved in ~10 mL of 5% HNO₃ in an acid-cleaned centrifuge tube. After bubbling subsided, the tubes were capped and gently shaken on a rocker table overnight to ensure complete reaction. The mixtures were centrifuged, and the supernatants were passed through acid-cleaned 0.45 μm polypropylene syringe filters (Whatman Puradisc™), collected in Teflon beakers, dried at 90°C, and then re-dissolved in 15 mL of 5% HNO₃ for elemental and isotopic analyses.

Most samples produced little to no residue after reaction, except those from the siliciclastic-rich member (Bed 26) of Meishan. Given the relatively low carbonate content of these samples, it is relevant to question whether the carbonate preserves primary seawater signals. Another question is whether the reagents used to dissolve carbonate minerals can leach Ca and Sr from coexisting silicate minerals. To address these questions, four samples from Bed 26 of the Meishan section and five samples representing the stratigraphically-equivalent interval of the carbonate-rich Dajiang section (see Section 2.4.5) were selected for a sequential leaching experiment, modified from Bailey et al. (2000) and Liu et al. (2013). Previous studies have shown that dilute acetic acid (HAc) can dissolve carbonate without affecting non-carbonate phases (e.g., Bailey et al., 2000; Bayon et al., 2002). We employed HAc solutions with concentrations of 0.25%, 1%, and 5%. Subsamples of micro-drilled powders (~200 mg/sample) were weighed into acid-cleaned 50 mL centrifuge tubes and first reacted with ~25 mL of 1N ammonium acetate (NH₄Ac, buffered to pH=8.2) to isolate surface-adsorbed phases and other exchangeable cations (Gao, 1990; Bailey et al., 2000). The remaining residues were then sequentially reacted with ~15 mL of 0.25%, 1%, and 5% HAc. For each step, mixtures were agitated in an ultrasonic bath for 15 min and then centrifuged at 3500 rpm for 15 min. The supernatants were filtered through 0.45 μm polypropylene

syringe filters into acid cleaned Teflon vials, dried at 90°C, and re-dissolved in 5% HNO₃. Before proceeding to the next step, the residues were rinsed with Milli-Q water, which was discarded after centrifuging.

2.3.2 Elemental Concentrations

Elemental concentrations (Ca, K, Mg, Mn, Na, Sr) were measured with a Thermo Scientific iCAP 6500 ICP-OES. The samples were diluted to minimize matrix effects. The analytical standard NIST 1643f was repeatedly analyzed to assess the accuracy and reproducibility of the method. Results were within $\pm 5\%$ of reported concentrations. Measured Ca and Sr concentrations were also compared with those determined by isotope dilution as part of the double-spike measurements presented below. Differences were within $\pm 5\%$. Calcium concentrations were used to estimate wt.% carbonate assuming stoichiometric CaCO₃.

2.3.3 Ca and Sr isotope ratios

Ca and Sr isotope ratios were measured in the Radiogenic Isotope Geochemistry Clean Laboratory at Northwestern University using a Thermo-Fisher Triton MC-TIMS equipped with $10^{11} \Omega$ amplifier resistors. Analytical sessions spanned a period of three years. Samples were analyzed out of stratigraphic order, and duplicates of the 5% HNO₃ dissolutions were measured for 20% (n = 25) of the samples, selected randomly. Three approaches were taken to measure duplicates, including reanalysis of the same solution of dissolved powder, re-dissolution and reanalysis of the same powder, and analysis of altogether different powders obtained by re-micro-drilling the original hand samples. In some instances, duplicates were analyzed in the same analytical session, while in others, measurements were separated by time periods of weeks to years.

Ca isotope ratios (⁴⁴Ca/⁴⁰Ca) were measured using an optimized ⁴³Ca-⁴²Ca double-spike technique introduced by Holmden and Bélanger (2010) and further developed by Lehn et al.

(2013). All procedures employed ultrapure reagents, and total procedural blanks determined with a ^{43}Ca isotope dilution method were $\sim 50\text{-}80$ ng ($n = 12$), which is negligible compared to the amount of sample Ca processed. Aliquots of dissolved samples containing 50 μg of Ca were weighed into Teflon vials, spiked, capped, and gently heated at $\sim 60^\circ\text{C}$ overnight to ensure complete sample-spike equilibration. The solutions were dried at 90°C , re-dissolved in 0.5 mL of 1.55N HCl, and eluted through Teflon columns packed with Bio-Rad AG MP-50 cation exchange resin to separate Ca from K and other matrix elements. The purified Ca fractions were dried, reacted with 35% H_2O_2 to oxidize potential organic compounds, dried, re-dissolved in concentrated HNO_3 to convert Ca to nitrate form, dried, and finally, re-dissolved in 5 μL of 3N HNO_3 . Approximately 12.5 μg of Ca was loaded onto outgassed, single Ta filament assemblies together with 0.5 μL of 10% H_3PO_4 . Solutions were loaded between parafilm dams, spaced ~ 0.80 mm apart to prevent spreading across the surface of the filament, and dried at 3.5 amps. In the TIMS, a 20V ^{40}Ca ion-beam was achieved before collecting 120 sets of $^{40}\text{Ca}/^{42}\text{Ca}$, $^{43}\text{Ca}/^{42}\text{Ca}$, and $^{43}\text{Ca}/^{44}\text{Ca}$ ratios using a 3-hop duty cycle having variable integration times. Amplifier biases were cancelled using amplifier rotation. The ^{41}K beam ($<0.0001\text{V}$) was monitored to confirm that ^{40}K did not isobarically interfere with ^{40}Ca ($^{40}\text{K}/^{41}\text{K} = 0.00174$). The total analysis time was 2.5 – 3 hr per sample. An iterative procedure was used to correct instrumental mass fractionation and subtract the spike composition from the measured composition of the spike-sample mixture (Eugster et al., 1969). Runs were carefully monitored to ensure a steady or increasing ^{40}Ca beam, an increasing raw $^{42}\text{Ca}/^{40}\text{Ca}$ fractionation pattern, and the absence of filament reservoir effects, which can appear as “reverse-fractionation” in uncorrected ratios or residual trends in fractionation-corrected ratios (Fantle and Bullen, 2009; Lehn and Jacobson, 2015). All results are reported in δ -notation relative to the OSIL Atlantic Seawater standard, where $\delta^{44/40}\text{Ca}(\text{‰}) =$

$$[(^{44}\text{Ca}/^{40}\text{Ca})_{\text{smp}}/(^{44}\text{Ca}/^{40}\text{Ca})_{\text{SW}}-1]\times 1000.$$

Collector cup drift due to changes in efficiency factors affects measurement of Ca isotope ratios (Holmden and Bélanger, 2010; Lehn et al., 2013; Lehn and Jacobson, 2015; He et al., 2017). Faraday cup degradation is frequently attributed solely to beam voltage (Mondal and Chakrabarti, 2018), but the net amount of time Ca ions are delivered to the collectors plays an equally important role (Lehn et al, 2013). While employing weaker beams can minimize Faraday collector damage, longer integration times and/or more scans are required to improve counting statistics such that the effects of weaker beams are offset. For example, measuring a 20V ^{40}Ca beam for 4 s and 120 scans (this study; Lehn et al., 2013) implants the same or lesser number of Ca ions into the receiving collector as measuring a 6-10V ^{40}Ca beam for 16 s and 100 scans (Mondal and Chakrabarti, 2018). Drift was quantified and accounted for by analyzing at least 6 seawater (SW) standards and 2 NIST 915b standards every 30 samples. During the period of study, repeated analyses yielded $\delta^{44/40}\text{Ca}_{\text{SW}} = 0.000\pm 0.003\text{‰}$ ($2\sigma_{\text{SEM}}$, $n=56$) and $\delta^{44/40}\text{Ca}_{915\text{b}} = -1.134\pm 0.003\text{‰}$ ($2\sigma_{\text{SEM}}$, $n=18$). The current long-term values for the laboratory are $\delta^{44/40}\text{Ca}_{\text{SW}} = 0.000\pm 0.002\text{‰}$ ($2\sigma_{\text{SEM}}$, $n=424$) and $\delta^{44/40}\text{Ca}_{915\text{b}} = -1.133\pm 0.003\text{‰}$ ($2\sigma_{\text{SEM}}$, $n=188$). These results correspond to a long-term, external reproducibility ($2\sigma_{\text{SD}}$) of $\pm 0.04\text{‰}$, which is the uncertainty assigned to samples.

Radiogenic and stable Sr isotope ratios ($^{87}\text{Sr}/^{86}\text{Sr}$ and $^{88}\text{Sr}/^{86}\text{Sr}$) were measured following the procedures presented in Andrews et al. (2016) and Andrews and Jacobson (2017). Total procedural blanks determined with an ^{84}Sr isotope dilution method were ~ 100 pg ($n = 11$), which is negligible compared to the amounts of sample Sr processed for both analyses. To measure $^{87}\text{Sr}/^{86}\text{Sr}$ ratios, aliquots of dissolved samples containing ~ 300 ng of Sr were weighed into Teflon vials, dried, re-dissolved in 8M HNO_3 , and eluted through inverted pipet tips packed with Eichrom Sr-Spec resin. The purified Sr fractions were dried and re-dissolved in 3 μL of 3N HNO_3 .

Approximately 150 ng of Sr was loaded between parafilm “dams” on outgassed, single Re filament assemblies together with 1 μL of a TaCl_5 solution. In the mass-spectrometer, an 8V ^{88}Sr ion-beam was achieved before collecting data in multi-dynamic mode for 110 duty cycles having a 4 s integration time. Measurements were made with amplifier rotation. The ^{85}Rb beam was monitored to ensure that ^{87}Rb did not isobarically interfere with ^{87}Sr ($^{87}\text{Rb}/^{85}\text{Rb} = 0.3856$). The total analysis time was 1-1.5 hr per sample. Instrumental mass fractionation was corrected by normalizing $^{86}\text{Sr}/^{88}\text{Sr}$ ratios to 0.1194 using an exponential law. During the period of study, repeated measurements of NBS 987 yielded a mean $^{87}\text{Sr}/^{86}\text{Sr}$ ratio of 0.710250 ± 0.000002 ($2\sigma_{\text{SEM}}$, $n=22$). The current, long-term mean $^{87}\text{Sr}/^{86}\text{Sr}$ ratio for this method is 0.710251 ± 0.000002 ($2\sigma_{\text{SEM}}$, $n=171$). These results correspond to a long-term external reproducibility ($2\sigma_{\text{SD}}$) of ± 0.000010 , which is the uncertainty assigned to samples.

To measure $^{88}\text{Sr}/^{86}\text{Sr}$ ratios, aliquots of dissolved samples containing 450 ng of Sr were weighed into Teflon vials and mixed with an ^{87}Sr - ^{84}Sr double-spike. The vials were capped and heated at 90°C overnight. The solutions were dried, re-dissolved in 8N HNO_3 , and purified using the same elution procedure described above. After drying, the purified Sr fractions were re-dissolved in 4.5 μL of 3N HNO_3 , and 1.5 μL aliquots containing ~ 150 ng of Sr were loaded between parafilm “dams” on outgassed, single Re filament assemblies together with 1 μL of a TaCl_5 solution. In the mass spectrometer, a 6V ^{88}Sr ion-beam was achieved before collecting $^{88}\text{Sr}/^{84}\text{Sr}$, $^{87}\text{Sr}/^{84}\text{Sr}$, and $^{86}\text{Sr}/^{84}\text{Sr}$ ratios in static mode for 160 duty cycles having a 16 s integration time. At least 140 cycles were used for the data reduction, which includes input of corresponding $^{87}\text{Sr}/^{86}\text{Sr}$ ratios. Measurements were made with amplifier rotation. The ^{85}Rb beam was monitored to confirm that ^{87}Rb did not isobarically interfere with ^{87}Sr . The total analysis time was 1 – 1.5 hr per sample. Data were reduced using the Eugster et al. (1969) equations. Similar to the analysis of

$^{44}\text{Ca}/^{40}\text{Ca}$ ratios, runs were carefully monitored to ensure a steady or increasing ^{88}Sr beam, an increasing raw $^{86}\text{Sr}/^{84}\text{Sr}$ fractionation pattern, and the absence of filament reservoir effects in both raw and fractionation-corrected ratios. All $^{88}\text{Sr}/^{86}\text{Sr}$ ratios are reported in δ -notation relative to NBS 987, where $\delta^{88/86}\text{Sr}$ (in ‰) = $[(^{88}\text{Sr}/^{86}\text{Sr})_{\text{smpl}}/(^{88}\text{Sr}/^{86}\text{Sr})_{\text{NBS987}} - 1] \times 1000$.

Collector cup drift also affects measurement of Sr isotope ratios (Andrews et al., 2016). In the case of $^{87}\text{Sr}/^{86}\text{Sr}$ ratios, acquiring data in multi-dynamic mode eliminates cup efficiency factors. For $^{88}\text{Sr}/^{86}\text{Sr}$ ratios, drift was quantified and accounted for in a manner similar to $^{44}\text{Ca}/^{40}\text{Ca}$ ratios. At least 6 NBS 987 standards and 2 IAPSO seawater standards were analyzed every 40 or fewer samples. During the period of study, repeated analyses yielded $\delta^{88/86}\text{Sr}_{\text{NBS987}} = 0.000 \pm 0.001\%$ ($2\sigma_{\text{SEM}}$, $n=40$) and $\delta^{88/86}\text{Sr}_{\text{IAPSO}} = 0.397 \pm 0.002\%$ ($\pm 2\sigma_{\text{SEM}}$, $n=17$). The current, long-term external reproducibility for NBS 987 is $\pm 0.018\%$ ($\pm 2\sigma_{\text{SD}}$, $n=206$), and the current, long-term external reproducibility for IAPSO seawater is $\pm 0.019\%$ ($\pm 2\sigma_{\text{SD}}$, $n=120$). Because the data reduction procedure employs measured $^{87}\text{Sr}/^{86}\text{Sr}$ ratios having an external reproducibility of $\pm 0.01\%$, errors must be propagated to arrive at the overall uncertainty for the reported $\delta^{88/86}\text{Sr}$ values (Andrews and Jacobson, 2017). The overall uncertainty therefore equals $\pm 0.020\%$ ($2\sigma_{\text{SD}}$), which is the uncertainty assigned to samples.

2.3.4 C and O isotope ratios

Carbon and oxygen isotope ratios were analyzed on carbonate samples using a Gas Bench II mated to a Delta V Plus Isotope Ratio Mass Spectrometer, located in the Stable Isotope Geochemistry Laboratory at Northwestern University. Powdered samples were purged with helium for 7 minutes and then reacted overnight at 30°C with 103% anhydrous phosphoric acid (H_3PO_4). Isotope ratios were calibrated against NBS-18, NBS-19, and one internal CaCO_3 standard and are reported in δ -notation ($\delta^{13}\text{C}$ and $\delta^{18}\text{O}$) relative to the Vienna Peedee Belemnite (VPDB)

scale. The current long-term reproducibilities ($2\sigma_{SD}$) for the $\delta^{13}C$ and $\delta^{18}O$ measurements are $\pm 0.12\%$ and $\pm 0.30\%$, respectively.

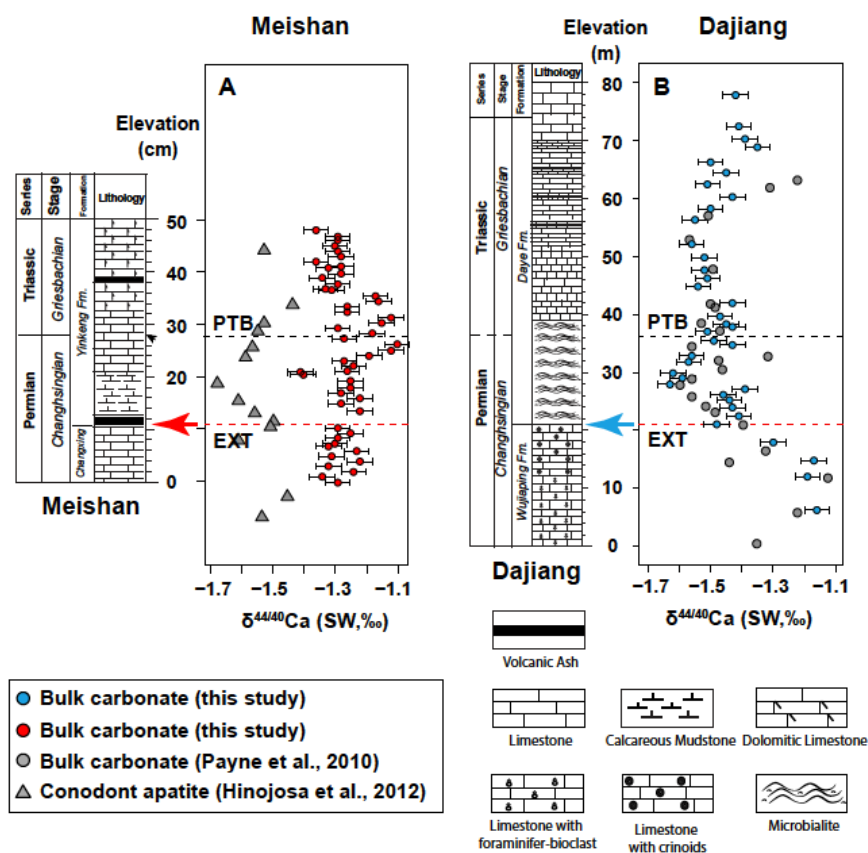


Figure 2-3 Comparison of $\delta^{44/40}Ca$ records across the Permian–Triassic transition from this study (colored) and published (grey) data for the (A) Meishan and (B) Dajiang sections. Published $\delta^{44/40}Ca$ data for Meishan represent hydroxyapatite conodonts (grey triangles; Hinojosa et al., 2012). Published $\delta^{44/40}Ca$ data for Dajiang are for bulk carbonate (grey circles; Payne et al., 2010). Published data reported on the bulk silicate earth scale (BSE) were converted to the seawater scale (SW) using the equation $\delta^{44/40}Ca_{BSE} = \delta^{44/40}Ca_{SW} + 0.86\%$ (Nielson et al., 2012, Melin et al., 2014).

2.4 Results

Table AI-1 provides results for the 5% HNO_3 leachates. Figure 2-2 shows detailed profiles of lithology, $\delta^{13}C$, $\delta^{44/40}Ca$, $^{87}Sr/^{86}Sr$, and $\delta^{88/86}Sr$ for the Meishan and Dajiang sections. Data for Meishan are plotted in red, while data for Dajiang are plotted in blue. Filled circles denote original

measurements, and crosses denote duplicates. All duplicates agreed with original analyses within the respective uncertainties, with the exception of three Ca isotope measurements. Duplicates for MS24e-4 yielded a difference of 0.05‰, while those for MS27-5 and MS27-6 yielded differences of 0.06‰. Given the diversity of duplicates analyzed (see Section 2.3.3), these results demonstrate the reproducibility of the Ca and Sr isotopic methods and further confirm that uncertainties determined from the repeated analysis of standards can be confidently applied to samples (Table AI-1).

2.4.1 Meishan section

The Meishan $\delta^{44/40}\text{Ca}$ record ($n=49$) exhibits $\sim 0.05\%$ to 0.10% variability at the centimeter-scale. Starting in Bed 24e, $\delta^{44/40}\text{Ca}$ values oscillate around a baseline of -1.25% and remain unchanged upsection through the EXT level and into the middle part of Bed 26. Several of these small oscillations were confirmed with repeat measurements. Values then rapidly decrease by 0.16% to -1.41% in the upper part of Bed 26 before gradually increasing by $\sim 0.30\%$ to a maximum of -1.10% , which straddles the PTB. Near the top of Bed 27, $\delta^{44/40}\text{Ca}$ values decrease to around -1.30% , which is slightly lower than the starting baseline of -1.25% in Bed 24e. The Meishan bulk carbonate $\delta^{44/40}\text{Ca}$ record reported here differs from the Meishan conodont record previously presented in Hinojosa et al. (2012) (Figure 2-3). $^{87}\text{Sr}/^{86}\text{Sr}$ ratios ($n=29$) increase from ~ 0.7071 in Bed 24e to ~ 0.7078 in Bed 29, a pattern consistent with previously published Meishan records (e.g., Dudás et al., 2017). However, a relatively large and abrupt increase (up to ~ 0.710 , see Table AI-1) occurs after the EXT level in Bed 26, with ratios returning to the upper end of pre-extinction levels in Bed 27. Simultaneously, $\delta^{88/86}\text{Sr}$ values ($n=20$) begin at 0.50% in Bed 24e, decrease by $\sim 0.15\%$ across the EXT level to 0.36% , and then increase to 0.45% toward the PTB.

2.4.2 Dajiang section

At Dajiang, $\delta^{44/40}\text{Ca}$ values (n=37) begin at -1.15‰, decrease by ~0.50‰ to a minimum of -1.63‰ across the EXT level, and then increase by 0.20‰ to -1.43‰ around the PTB. The Dajiang bulk carbonate $\delta^{44/40}\text{Ca}$ record generated in this study agrees with the one published in Payne et al. (2010), and it also compares well with the Meishan conodont record reported in Hinojosa et al. (2012) (Figure 2-3). $^{87}\text{Sr}/^{86}\text{Sr}$ ratios (n=25) minimally increase from ~0.7072 prior to the EXT level to ~0.7075 in the lower Triassic, consistent with other published records (e.g., Sedlacek et al., 2014; Dudás et al., 2017). $\delta^{88/86}\text{Sr}$ values (n=19) start at 0.35‰ and decrease by 0.15‰ across the EXT level to 0.20‰ before returning to 0.34‰ around the PTB. $\delta^{88/86}\text{Sr}$ values then increase to 0.45‰.

2.4.3 Correlation and comparison of sections

To interpret geochemical changes across the end-Permian mass extinction, it is important to correlate and compare the Meishan and Dajiang sections. At Meishan, different lines of evidence (e.g., Shen et al., 2011, Song et al., 2013) define the EXT level at the base of Bed 25, while the FAD of conodont *Hindeodus parvus* (Yin et al., 2001) indicates that the PTB occurs in the middle of Bed 27. In the Dajiang section, the boundary between the uppermost Permian skeletal limestone and the overlying microbialite defines the EXT level (e.g., Lehrmann et al., 2003; Payne et al., 2006; Song et al., 2009), but the exact placement of the PTB remains controversial. Lehrmann et al. (2007) placed the PTB in the middle of the microbialite by identifying the FAD of *Hindeodus parvus*, whereas other studies have argued that the abrupt lithologic change and potential dissolution surface observed at the base of the microbialite correspond to a hiatus of $\sim 61 \pm 48$ kyr, equivalent in time to Meishan Beds 25-27 (e.g., Jiang et al., 2014; Tian et al., 2015; Brosse et al., 2016). However, this is not consistent with the level of the most negative value of the $\square^{13}\text{C}$ excursion at Dajiang, which occurs in the middle of the microbialite unit (Figure 2-2).

Given potential regional speciation or extinction, facies changes, and other preservation and sampling issues, biostratigraphic correlation across extinction intervals can be challenging, especially in a high-resolution scale beyond fossil zonal resolution. In this case, chemostratigraphy provides a complementary tool. Both sections record the globally recognized negative $\delta^{13}\text{C}$ excursion (e.g., Korte and Kuzor, 2010; Shen et al., 2013), which occurs prior to the EXT level and ends near the PTB. In the interval that we measured at Meishan, $\delta^{13}\text{C}$ values start at $\sim 2.0\text{‰}$ in Bed 24e and abruptly decrease across the EXT level to a minimum of -0.8‰ in Bed 26. $\delta^{13}\text{C}$ values then recover to 1.4‰ in the lower part of Bed 27 before decreasing again to -0.1‰ in upper Bed 27. Finally, $\delta^{13}\text{C}$ values vary from 0.7‰ to 1.5‰ across the PTB before stabilizing around $\sim 1.0\text{‰}$. Compared to Meishan, the Dajiang $\delta^{13}\text{C}$ record displays a smooth curve, decreasing from 3.0‰ to -0.4‰ before returning to a slightly higher value of 2.2‰ , marking a $\sim 3.0\text{‰}$ negative excursion that is within the range reported by Payne et al. (2010) and Lehrmann et al. (2015). In an effort to avoid outcrop sampling artifacts and other biases, we employ the EXT level as a first datum and the upper $\delta^{13}\text{C}$ baseline after the excursion as a second datum. Thus, the PTB at the base of Bed 27c in the Meishan section correlates to 36 m in the upper middle of the microbialite in the Dajiang section, which generally matches the definition of the PTB based on conodonts by Payne et al. (2007) and Lehrmann et al. (2015).

Radioisotopic dating of intercalated volcanic ash layers, aided by the modern U-Pb CA-ID-TIMS method with improved accuracy, constrains the absolute timing of the isotopic and geochemical shifts across the PTB in China (Burgess et al., 2014; Lehrmann et al., 2015; Baresel et al., 2017; Shen et al., 2019). These measurements yield ages of 251.941 ± 0.037 Ma and 251.880 ± 0.031 Ma for Meishan Bed 25 and Bed 28, respectively (Burgess et al., 2014), indicating that the Ca and Sr isotope changes measured in the present study occur within $\sim 61 \pm 48$ kyr or less.

As shown in this study, shifts in $\delta^{44/40}\text{Ca}$ and $\delta^{88/86}\text{Sr}$ values occur in a relatively narrow range between upper Bed 24e and Bed 27 at Meishan over a <60 kyr interval between the EXT level and the PTB, as well as in the correlative interval at Dajiang. $\delta^{44/40}\text{Ca}$ and $\delta^{88/86}\text{Sr}$ values decrease by $\sim 0.50\%$ and $\sim 0.15\%$ over the first half of this interval and then increase by similar magnitudes leading up to the PTB. However, $^{87}\text{Sr}/^{86}\text{Sr}$ ratios in the Dajiang section do not show the relatively broad positive shift observed in Meishan Bed 26. As discussed below in Section 2.4.4 and elsewhere throughout the study, the different $^{87}\text{Sr}/^{86}\text{Sr}$ records more likely reflect diagenetic alteration of the Meishan section than a hiatus in the Dajiang section.

2.4.4 Proxies for lithology and diagenesis

Figure 2-4 shows CaCO_3 weight percentages, as well as Mg/Ca, Sr/Ca, and Mn/Sr ratios, versus stratigraphic height. Figures A1-1 and A1-2 examine correlations between various isotopic and elemental ratios, while Figure A1-3 evaluates $\delta^{44/40}\text{Ca}$ and $\delta^{88/86}\text{Sr}$ values relative to Sr concentrations. In the Meishan section, decreases in the abundance of CaCO_3 (Figure 2-4-A) from $\sim 80\%$ to $\sim 10\%$ correlate with a lithological change from skeletal carbonate in Bed 24e to calcareous mudstone in Bed 26. CaCO_3 abundances then increase upward to $\sim 50\%$. The Dajiang section generally exhibits higher average CaCO_3 abundances ($\sim 70\%$). The CaCO_3 abundances (Figure 2-4-A) at Dajiang decrease from $\sim 80\%$ to $\sim 60\%$ in the lower microbialite bed, corresponding to the time-equivalent decrease observed at Meishan, before reaching maximum values ($\sim 100\%$) in the upper part of the microbialite, equivalent to Bed 27 at Meishan. Mg/Ca ratios (Figure 2-4-B) provide a measure of the degree of dolomitization. Starting in Bed 26 at Meishan, Mg/Ca ratios increase gradually to a maximum of ~ 0.6 mol/mol in Bed 29. These data suggest a higher degree of dolomitization upsection. In contrast, Mg/Ca ratios at Dajiang are relatively low in the Wuchiaping Fm. but vary in the overlying microbialite. Both sections exhibit

similar patterns of Sr/Ca ratios (Figure 2-4-C), although Dajiang displays a marginally higher average value (0.8 vs. 1.3 nmol/ μ mol). In the Meishan section, Mn/Sr ratios (Figure 2-4-D) increase upward from ~0.5 to ~5 mol/mol with a mean of 2.75 mol/mol, while Mn/Sr ratios in the Dajiang section are less than 0.7 mol/mol.

$\delta^{44/40}\text{Ca}$ and $\delta^{88/86}\text{Sr}$ values do not linearly correlate with any of these elemental ratios (Figure A1-1), nor do they correlate with each other (Figure A1-2). Nonetheless, a few instances exist where parameters for one or both sections display statistically meaningful linear correlations. For example, $\delta^{88/86}\text{Sr}$ and $\delta^{13}\text{C}$ values for both sections weakly correlate (Figure A1-2), whereas no correlations exist between $\delta^{44/40}\text{Ca}$ and $\delta^{13}\text{C}$ values. $\delta^{18}\text{O}$ and $\delta^{13}\text{C}$ values at Meishan strongly correlate, while no correlations exist at Dajiang. Similarly, $^{87}\text{Sr}/^{86}\text{Sr}$ ratios at Meishan correlate with CaCO_3 abundances, as well as Sr/Ca and Mn/Sr ratios, while $^{87}\text{Sr}/^{86}\text{Sr}$ ratios measured for the Dajiang section do not. Given these latter four observations, the probability of diagenetic alteration at Meishan is high (see Section 2.5.1.2).

2.4.5 Sequential leaching experiment

The relatively high $^{87}\text{Sr}/^{86}\text{Sr}$ ratios and low carbonate contents observed in Meishan Bed 26 suggest that syn- and/or post-depositional diagenetic processes may have affected the geochemical signature of these carbonates, or that the 5% HNO_3 leaching procedure acquired Sr from coexisting silicate minerals. Therefore, we applied a sequential leaching procedure to Bed 26 samples, as well as stratigraphically equivalent samples from Dajiang. Table AI-2 provides the results, and the data are plotted in Figure 2-5. Relative to the original 5% HNO_3 leachates, which we assume dissolved all of the carbonate present, the four sequential leaching steps in total acquired >92% of the Ca and >95% of the Sr for the Meishan Bed 26 samples and >95% of the Ca and >92% of the Sr for the corresponding Dajiang samples.

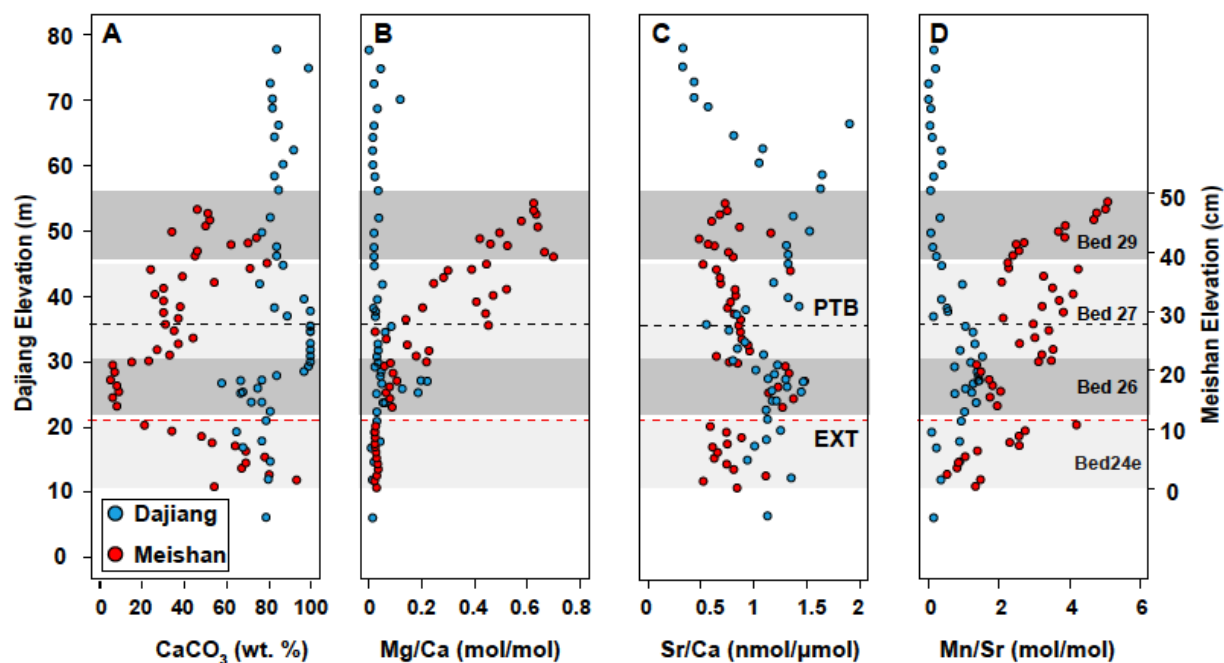


Figure 2-4 Stratigraphic height vs (A) CaCO_3 weight percentage, (B) Mg/Ca ratios (mol/mol), (C) Sr/Ca ratios (nmol/ μmol), and (D) Mn/Sr ratios (mol/mol) in bulk carbonate samples from the Meishan and Dajiang sections.

Figure 2-5 also compares the measured isotope ratios for each leachate with the isotope ratios determined for the original 5% HNO_3 leachates (filled circles), and Table AI-2 provides the weighted average isotope ratios for all leachates combined, determined using the concentrations and isotope ratios of each step. The weighted average $^{87}\text{Sr}/^{86}\text{Sr}$ ratios determined for the sequential leachates agree with the $^{87}\text{Sr}/^{86}\text{Sr}$ ratios measured for the original 5% HNO_3 leachates. Nonetheless, radiogenic Sr isotope ratios for Meishan Bed 26 showed relatively large differences (in the second decimal place) as a function of leaching step. For example, in the case of sample MS26-1, the 0.25% HAc yielded an $^{87}\text{Sr}/^{86}\text{Sr}$ ratio of 0.71105, while the 5% HAc step yielded an $^{87}\text{Sr}/^{86}\text{Sr}$ ratio of 0.70856. The sequential leaching procedure did not reveal major discrepancies for $\delta^{44/40}\text{Ca}$ and $\delta^{88/86}\text{Sr}$ values in Bed 26, or for $\delta^{44/40}\text{Ca}$ and $\delta^{88/86}\text{Sr}$ values, as well as $^{87}\text{Sr}/^{86}\text{Sr}$ ratios, of stratigraphically equivalent samples at Dajiang.

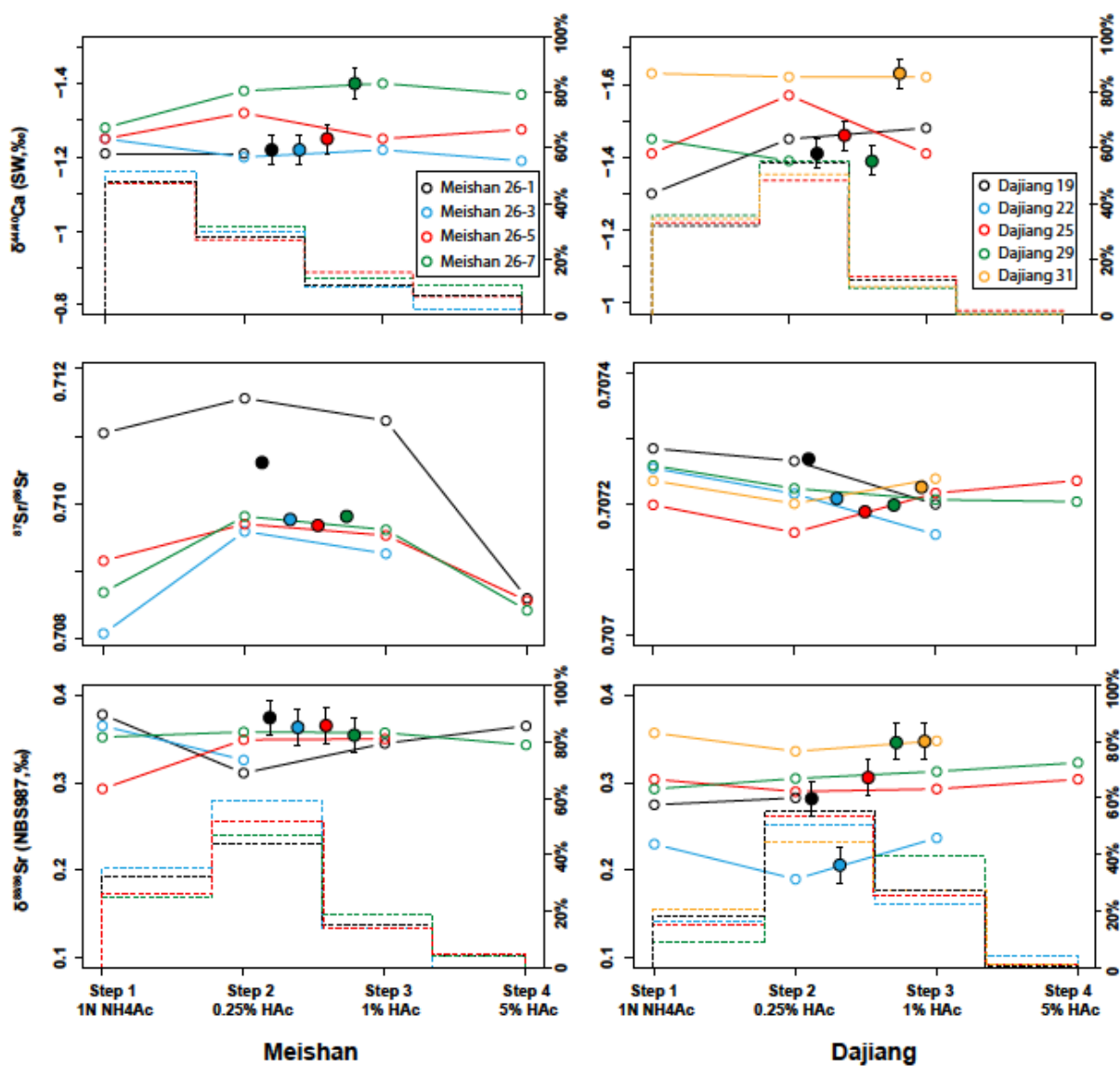


Figure 2-5 Open circles show $\delta^{44/40}\text{Ca}$, $^{87}\text{Sr}/^{86}\text{Sr}$, and $\delta^{88/86}\text{Sr}$ as a function of sequential leaching step for Bed 26 samples from Meishan (left) and stratigraphically-equivalent samples from Dajiang (right). Filled circles show data for the original 5% HNO_3 leachates. Dashed histograms show the proportions (%) of Ca and Sr obtained for each leaching step relative to the original 5% HNO_3 leachates (see Section 2.4.5 for details).

2.5 Discussion

The complex Ca and Sr isotope patterns for the two studied sections invite many potential interpretations. To arrive at an overall conclusion for the dataset, we focus on answering three

main questions: (1) Does Dajiang present primary $\delta^{44/40}\text{Ca}$, $\delta^{88/86}\text{Sr}$, and $^{87}\text{Sr}/^{86}\text{Sr}$ records? (2) Why does Meishan display higher isotope ratios, as well as coherent and incoherent stratigraphic trends relative to Dajiang? and (3) What mechanism(s) caused the negative $\delta^{44/40}\text{Ca}$ and $\delta^{88/86}\text{Sr}$ excursions in the <60 kyr interval between the EXT and the PTB? We attempt to reconcile diverse hypotheses with the aid of complementary elemental and isotope measurements, previously published Ca isotope data for other P-Tr sections, and model predictions. To this end, we organize our discussion according to three processes/variables expected to elicit isotopic variations within and between the two sections, namely diagenesis, spatial variability in bulk fractionation factors, and perturbations to global seawater input and output fluxes.

2.5.1. Diagenesis

Diagenesis can partially or completely reset the chemical and isotopic composition of bulk carbonate sediment and rocks (e.g., Bathurst, 1972; Brand and Veizer, 1980). In this section, we consider both syn-depositional (early marine) and post-depositional (late stage) processes and their implications for the fidelity and meaning of the measured isotopic signals.

2.5.1.1 Syn-depositional (early marine) diagenesis

Syn-depositional or early marine diagenesis occurs during carbonate sediment deposition, but before lithification (Bathurst, 1972; Flügel, 2013). In brief, syn-depositional diagenesis proceeds via two pathways (i.e., recrystallization and neomorphism) that alter crystal fabrics, mineralogical compositions, and in some instances, the geochemistry of bulk sediments. Following previous workers (e.g., Folk, 1965; Flügel, 2013; Lau et al., 2017; Higgins et al., 2018), recrystallization includes dissolution and re-precipitation mechanisms whereby new calcite crystals form from existing calcite crystals, while neomorphism refers to the *in-situ* transformation of primary aragonite to calcite. Dolomite, which occurs in and above Bed 27 of the Meishan

section, can form during syn-depositional diagenesis (e.g., Baker and Kastner, 1981; Gregg et al., 1992; Gammon et al., 2012; Blättler et al., 2015; Li and Jones, 2017; Ahm et al., 2019), as well as during late stage diagenesis (e.g., Graf et al., 1956; Adams and Rhodes, 1960; Hanshaw et al., 1971; Warren, 2000).

In all cases, carbonate minerals are open to elemental and isotopic exchange with surrounding seawater and pore fluids, although the magnitude of the effect for any given tracer depends on numerous factors, such as the concentration and isotopic gradients between water and carbonate sediment and whether the system is open (fluid-buffered), closed (rock-buffered), or somewhere in between (Brand and Veizer, 1980, 1981; Banner and Hanson, 1990; Derry, 2010; Fantle et al., 2010; Fantle and Higgins, 2014; Swart, 2015; Higgins et al., 2018; Ahm et al., 2019). The resulting geochemical changes to bulk sediment follow the principles of end-member mixing, and the predicted mixing trends are non-linear (Banner and Hanson, 1990; Ahm et al., 2018). However, for simplicity, models assume that end-members (e.g., aragonite or seawater) have fixed compositions devoid of any spatial or temporal heterogeneity and that mixtures (i.e., bulk sediment) are similarly free from changes in the geochemistry of seawater or kinetic effects during formation, both of which can produce trends that are difficult to distinguish from diagenetic alteration (Kimmig and Holmden, 2017; see for example, Figure 7 in Ahm et al., 2018; Ahm et al., 2019).

Syn-depositional diagenesis clearly causes Sr loss, and Sr/Ca ratios have long been used as a diagenetic indicator (Brand and Veizer, 1980; Baker et al., 1982; Banner, 1995). The phenomenon is especially pronounced for neomorphism, given that aragonite has much higher Sr concentrations than calcite (Kinsman, 1969; Paquette and Reeder, 1995; Finch and Allison, 2007). Carbonate $\delta^{13}\text{C}$ values are susceptible to alteration, although the concentration and isotopic mass-

balance between the precursor minerals and the diagenetic fluid plays a critical role in determining the magnitude and direction of change (Dickson and Coleman, 1980; Allan and Matthews, 1982; Lohmann, 1988; Romanek et al., 1992; Swart, 2008; Swart 2015; Ahm et al., 2019). Early diagenetic alteration can reset $\delta^{18}\text{O}$ values while preserving primary $\delta^{13}\text{C}$ values (Allen and Matthews, 1982; Ahm et al., 2018).

The advent of Ca isotope geochemistry has provided valuable new insight into recrystallization and neomorphism. Calcium isotope studies conducted in modern marine settings offer clear evidence for early diagenetic alteration (Fantle et al., 2015; Higgins et al., 2018; Blättler et al., 2015). For example, because the calcite fractionation factor is a function of precipitation rate (Fantle and Depaolo, 2007; Jacobson and Holmden, 2008; Tang et al., 2008b; AlKhatib and Eisenhauer, 2017a), the fractionation factor is \pm zero in slowly recrystallizing marine sediments, such that newly formed (diagenetic) calcite has higher $\delta^{44/40}\text{Ca}$ values than unaltered forms due to the incorporation of seawater Ca (Fantle and DePaolo, 2007; Bradbury and Turchyn, 2018). The effect appears particularly pervasive in carbonate-rich deep-sea sediments and platform environments (Fantle and DePaolo, 2007; Fantle et al., 2015; Higgins et al., 2018; Ahm et al., 2019), but may be suppressed in settings with relatively higher amounts of clay and organic matter (Turchyn and DePaolo, 2011). Moreover, fluid buffered systems yield greater resetting than rock buffered systems (Kimmig and Holmden, 2017; Higgins et al., 2018; Ahm et al., 2018, 2019). Similar to Sr/Ca ratios, relatively large shifts are expected for neomorphism, given that aragonite tends to have much lower $\delta^{44/40}\text{Ca}$ values than calcite (Gussone et al., 2005; Blättler et al., 2012; Gussone and Dietzel, 2016; Pruss et al., 2018; Ahm et al., 2019).

Stable Sr isotopes may show patterns similar to Ca isotopes given that the calcite-water and aragonite-water fractionation factors for the systems show complementary rate-controlled

behavior (Böhm et al., 2012; Stevenson et al., 2014; AlKhatib et al., 2017a, b; Müller et al., 2018). We note that Voigt et al. (2015) observed high $\delta^{88/86}\text{Sr}$ values in pore waters extracted from carbonate-rich deep-sea sediments but no changes in carbonate $\delta^{88/86}\text{Sr}$ values. These results may suggest either minimal recrystallization occurred or carbonate $\delta^{88/86}\text{Sr}$ values are less susceptible to alteration because carbonate has higher Sr concentrations than water. In either case, the current expectation is that the lowest $\delta^{44/40}\text{Ca}$ and $\delta^{88/86}\text{Sr}$ values of any given dataset are the most pristine, while higher values may represent progressively more alteration.

With the aid of the above interpretative framework, we consider two key questions:

2.5.1.1.1 Does syn-depositional diagenesis explain why Meishan has higher $\delta^{44/40}\text{Ca}$ and $\delta^{88/86}\text{Sr}$ values than Dajiang?

Recent research focusing on the Ediacaran Period (635-541 Ma) has argued that varying levels of early marine alteration, including wholesale resetting of sedimentary columns, explains regional differences in $\delta^{44/40}\text{Ca}$ values at the outcrop scale (Ahm et al., 2019). We pose this hypothesis for the present study and first examine whether the $\delta^{44/40}\text{Ca}$ and $\delta^{88/86}\text{Sr}$ offsets between Meishan and Dajiang reflect overall greater alteration at Meishan. If correct, then $\delta^{44/40}\text{Ca}$ and $\delta^{88/86}\text{Sr}$ values should co-vary with Sr/Ca, $\delta^{13}\text{C}$, and other diagenetic indicators, but no trends exist (Figures 2-6, A1-1, A1-2, A1-3). These results are not surprising because the two sections display nearly identical Sr/Ca and $\delta^{13}\text{C}$ records, despite differences in their $\delta^{44/40}\text{Ca}$ and $\delta^{88/86}\text{Sr}$ values.

The absence of trends could reflect the limited size of our dataset, as analyses of multiple sections are required to confidently fit the non-linear diagenetic mixing curves (e.g., Ahm et al., 2019). To address this point, we compiled $\delta^{44/40}\text{Ca}$, Sr/Ca, and $\delta^{13}\text{C}$ data for other sections spanning the end-Permian (Figure 2-6). Magnesium isotopes can provide additional insight (Fantle and Higgins, 2014; Higgins et al., 2018; Ahm et al., 2019), but no data are available for the P-Tr at

present. Similarly, no studies have reported $\delta^{88/86}\text{Sr}$ values across the P-Tr, with the exception of three brachiopod samples analyzed in Vollstaedt et al. (2014). On a diagram of $\delta^{44/40}\text{Ca}$ versus Sr/Ca (Figure 2-6-A), one heavily dolomitized section (Saiq, Oman) trends toward high $\delta^{44/40}\text{Ca}$ values at low and relatively constant Sr/Ca ratios. Ediacaran dolostones show a very similar trend (see Figure 9 in Ahm et al., 2019). More work may ultimately demonstrate this pattern as a diagnostic indicator of syn-depositional dolomitization.

The remaining P-Tr sections, including Meishan and Dajiang, mostly comprise limestone, especially in the main interval of interest between the EXT level and the PTB. Here, the interpretation is less clear. A few samples from one section (Taşkent, Turkey) suggest decreasing Sr/Ca ratios at nearly constant $\delta^{44/40}\text{Ca}$ values, while the other sections do not define an obvious correlation. Ediacaran limestones, on the other hand (not plotted in Figure 2-6), show a much larger range of $\delta^{44/40}\text{Ca}$ values and Sr/Ca ratios (see Figure 8 in Ahm et al., 2019). Beyond the null hypothesis that the P-Tr limestone records are primary because the samples experienced minimal recrystallization and neomorphism, multiple interpretations exist. One idea is that the samples extensively evolved from an aragonite precursor having a low $\delta^{44/40}\text{Ca}$ value and a high Sr/Ca ratio. Aragonite fan pseudomorphs, for example, occur in lower Triassic rocks but have not been described for the time period under investigation here (Kershaw et al., 1999; Woods et al., 1999; Lehrmann et al., 2015; Deng et al., 2017). An equally plausible alternative explanation is that the samples experienced extensive recrystallization and neomorphism, but under highly rock-buffered conditions that preserved primary signals (e.g., Higgins et al., 2018). Indeed, recrystallization fabrics are described for the rocks composing both sections (Yang et al., 2011; Kershaw et al., 2012; Lehrmann et al., 2015; Lau et al., 2017; Li and Jones, 2017), but the $\delta^{44/40}\text{Ca}$ values are not elevated by comparison to aragonite and calcite formed in the modern ocean (e.g., Gussone and

Dietzel, 2016). Some of the scatter in Figure 2-2-B could reflect variations in the initial proportions of aragonite and calcite in the sections, which in turn would cause differing degrees of neomorphism (Farkaš et al., 2016; Jost et al., 2017; Lau et al., 2017; Silva-Tamayo et al., 2018). The relationship between $\delta^{44/40}\text{Ca}$ and [Sr] can help discriminate the effect (Lau et al., 2017). However, such a diagram (Figures 2-7, A1-3) for the P-Tr sections also shows no correlation. While Meishan has higher $\delta^{44/40}\text{Ca}$ and lower [Sr] compared to Dajiang, several samples from the Tesero section in Italy have the same [Sr] as Meishan, but even lower $\delta^{44/40}\text{Ca}$ compared to Dajiang.

A diagram of $\delta^{44/40}\text{Ca}$ versus $\delta^{13}\text{C}$ offers potential to pinpoint the theorized aragonite end-member and quantify the degree of alteration (Figure 2-6-B). However, the P-Tr limestones again show no trend, in marked contrast to the Ediacaran limestones (see Figure 8 in Ahm et al., 2019). We attribute the difference to the C isotope composition of dissolved inorganic carbon (DIC). To interpret carbonate $\delta^{13}\text{C}$ values as the byproduct of early marine alteration, it is necessary to assume that the DIC pool of diagenetic fluids had a constant isotopic composition. This assumption appears valid for the Ediacaran (Higgins and Schrag, 2003), but is more questionable for the end-Permian given that the Siberian Traps eruption likely injected large quantities of isotopically light C into the atmosphere-ocean system (Retallack and Jahren, 2008; Svensen et al., 2009; Sobolev et al., 2011; Shen et al., 2012; Erwin, 2015).

Additional observations also raise doubt about an early diagenetic origin for the entirety of the Meishan $\delta^{44/40}\text{Ca}$ and $\delta^{88/86}\text{Sr}$ records. For instance, elevation of $\delta^{44/40}\text{Ca}$ values during recrystallization is expected to be particularly pervasive in carbonate-rich platform environments like Dajiang, yet Dajiang has overall lower $\delta^{44/40}\text{Ca}$ values compared to Meishan. At Meishan, $\delta^{44/40}\text{Ca}$ values increase from the top of Bed 26 into Bed 27, where the highest $\delta^{44/40}\text{Ca}$ values

occur. Bed 27 comprises dolomitic carbonate, but Dajiang exhibits a similar increase over the same interval. Moreover, $\delta^{44/40}\text{Ca}$ values in both sections decrease upsection, even though Mg/Ca ratios at Meishan indicate increasing dolomitization. Significant contrast between the dolomitic limestone in Bed 27 at Meishan and the dolostone in the Saiq section (Figure 2-6) may imply fundamentally different formation mechanisms or much greater resetting in the latter. Finally, carbonate minerals preferentially incorporate lighter Sr isotopes (e.g., Fietzke and Eisenhauer, 2006; Halicz et al., 2008; Krabbenhöft et al., 2009, 2010; Böhm et al., 2012; Stevenson et al., 2014), yet most of the $\delta^{88/86}\text{Sr}$ values at Meishan and Dajiang are either equivalent to or higher than the modern value for seawater (0.39‰). Before the EXT level, values at Meishan are near 0.50‰, while those at Dajiang are closer to 0.30‰. These data are consistent with the hypothesis that the end-Permian ocean had a higher $\delta^{88/86}\text{Sr}$ value than the present day (Vollstaedt et al., 2014).

2.5.1.1.2 Is the ‘primary’ signal diagenetic?

Another hypothesis is that evolving early diagenetic conditions can produce stratigraphic patterns in geochemical proxies that mimic those traditionally considered as primary signals. Several factors could have influenced the preservation of carbonate sediment in the end-Permian ocean, including ocean stratification, upwelling, eutrophication, anoxia, and euxinia to name a few (e.g., Knoll et al., 1996; Wignall and Twitchett, 1996; Hotinski et al., 2001; Rampino and Caldeira, 2005; Riccardi et al., 2007; Meyer et al., 2008; Schobben et al., 2015). Addressing all of these potential drivers is beyond the scope allowed by our dataset. Here, we simply consider the basic question whether the negative $\delta^{44/40}\text{Ca}$ and $\delta^{88/86}\text{Sr}$ excursions reflect a shift from fluid- to rock-buffered conditions.

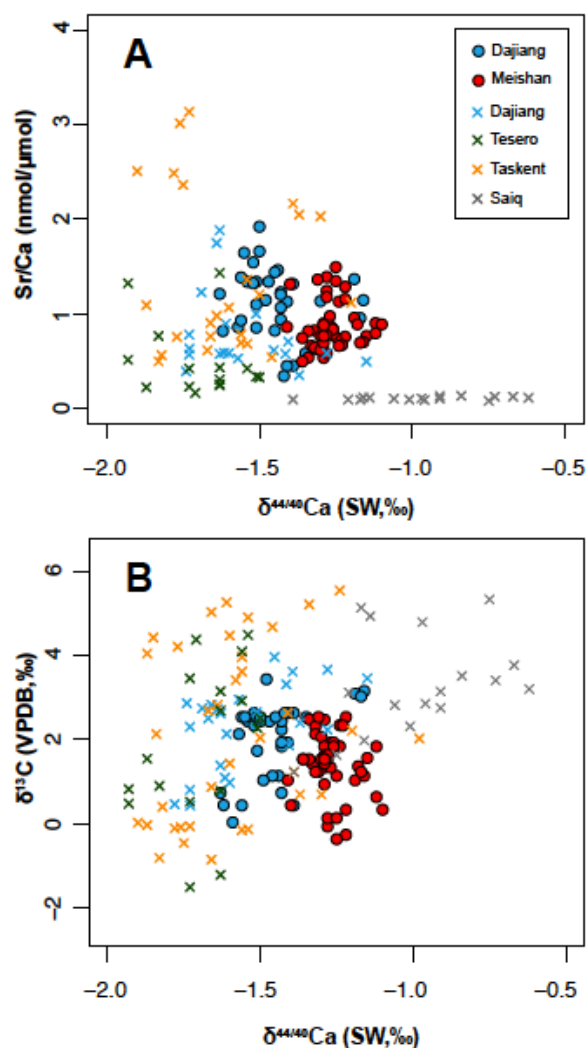


Figure 2-6 Cross-plots of (A) Sr/Ca vs $\delta^{44/40}\text{Ca}$ and (B) $\delta^{13}\text{C}$ vs $\delta^{44/40}\text{Ca}$. Filled circles indicate data from this study. Colored crosses indicate data from other studies. Dajiang data are from Payne et al. (2010). Tesero, Taškent, and Saiq data are from Silva-Tamayo et al. (2018). Note that dolostones dominate the Saiq section. Detailed lithological descriptions can be found in Silva-Tamayo et al. (2018). No linear correlations are observed at the significance level of 0.01 (A: $n=179$, linear regression: $R^2 = 0.12$, $p\text{-value} = 0.005$, SMA regression: $R^2 = 0.12$, $p\text{-value} = 0.005$; B: $n=179$, linear regression: $R^2 = 0.06$, $p\text{-value} = 0.002$, SMA regression: $R^2 = 0.06$, $p\text{-value} = 0.002$). Note that diagenetic mixing curves are non-linear; see Section 2.5.1.1.

At Dajiang, for example, the early diagenesis paradigm implies greater alteration below the EXT level than above, or alternatively, that the negative Ca and stable Sr isotope excursions

between the EXT level and the PTB represent preservation of the most pristine signals. Enhanced preservation requires either increased sedimentation rates favoring rock-buffered recrystallization or progressively less neomorphism. However, global sedimentation during the end-Permian was at a minimum for the Phanerozoic (Peters and Husson, 2017; Kump, 2018), and we expect ocean acidification to reduce carbonate accumulation in particular, thereby favoring fluid-buffered recrystallization. Equally challenging questions emerge when attempting to attribute the subsequent positive isotope shifts to enhanced fluid-buffered conditions.

In general, the $\delta^{44/40}\text{Ca}$ and $\delta^{13}\text{C}$ trends span a major lithologic boundary, from limestone to microbialite, and both records correlate with other sections worldwide (Kort and Kozur, 2010; Silva-Tamayo et al., 2018). Syn-depositional diagenesis has been variably invoked to explain both stratigraphic coherency and incoherency in geochemical records from different time periods throughout Earth history (e.g., Swart, 2008; Cui et al., 2017; Ahm et al., 2019). In the case of the end-Permian, more research is needed to identify an early diagenetic mechanism that can yield globally synchronous geochemical records within 60 kyr or less.

2.5.1.2 Post-depositional (late stage) diagenesis

Post-depositional or late stage diagenesis, including dissolution, cementation, and dolomitization, occurs after lithification in the marine realm, subaerial environments, and deeper crustal locations where pressure, temperature, and water circulation play a significant role. The degree of alteration depends on many of the same factors as syn-depositional diagenesis, such as water-rock ratios, concentration and isotopic gradients between water and rock, and recrystallization rates. In general, studies have shown that post-depositional alteration decreases Sr and Na concentrations and increases Mn and Fe concentrations, as well as textural maturity (Bathurst, 1972; Brand and Veizer, 1980; Longman, 1980; Moore, 1989). Post-depositional

diagenesis can decrease carbonate $\delta^{18}\text{O}$ values due to interaction with fluids having low $\delta^{18}\text{O}$ values and changes in fractionation during recrystallization at elevated temperatures (Brand and Veizer, 1980; Allan and Matthews, 1982). At Meishan, the lowest $\delta^{18}\text{O}$ values occur in Beds 26 and 27, which also show elevated Mn/Sr ratios, consistent with post-depositional alteration (Brand and Veizer, 1980; Derry, 2010). Jones and Li (2017) argued that meteoric diagenesis altered the chemical and isotopic composition of Beds 26 to 28 and contributed to increased dolomitization upsection. Subaerial alteration could have occurred during sea level fall (Figure 2-2). The strong correlation between $\delta^{13}\text{C}$ and $\delta^{18}\text{O}$ values in the Meishan section further supports post-depositional diagenetic overprinting (Figure A1-2-A). No correlation exists between $\delta^{13}\text{C}$ and $\delta^{18}\text{O}$ values at Dajiang, yet the Meishan and Dajiang $\delta^{13}\text{C}$ records favorably compare. Moreover, the negative $\delta^{13}\text{C}$ excursions that occur in both sections are globally recognized, not only in carbonate rocks (e.g., Korte and Kozur, 2010; Shen et al., 2013), but also in bulk organic matter (e.g., Krull et al., 2000; Shen et al., 2011) and specific organic compounds (e.g., Grice et al., 2005, 2007; Xie et al., 2007).

Formation waters and brines in siliciclastic-rich sections commonly show much higher $^{87}\text{Sr}/^{86}\text{Sr}$ ratios compared to Phanerozoic seawater (e.g., Stueber et al., 1984, 1987; McNutt et al., 1990; Banner, 1995). Interactions with Rb-rich feldspar and clay minerals contained within carbonate sediments and rocks can elevate groundwater $^{87}\text{Sr}/^{86}\text{Sr}$ ratios (Chaudhuri and Brookins, 1979; Ohr et al., 1991; Chaudhuri and Clauer, 1993; Stewart et al., 2015), and meteoric water that infiltrates carbonate outcrops may also exhibit relatively high $^{87}\text{Sr}/^{86}\text{Sr}$ ratios due to silicate weathering at the Earth's surface (e.g., Kump, 1989; Davis et al., 2003). Both processes can yield abnormally high $^{87}\text{Sr}/^{86}\text{Sr}$ ratios in recrystallized carbonates (e.g., Banner and Hasson, 1990; Banner, 1995). Elevated and variable $^{87}\text{Sr}/^{86}\text{Sr}$ ratios measured in the Meishan section, which

correlate with relatively high Mn/Sr ratios, are consistent with such effects (Figure 2-4). The variability observed in the sequential leachates (Figure 2-5) provides more evidence that the bulk Meishan samples do not offer a primary radiogenic Sr isotope signal. While we did not apply the sequential leaching procedure to other Meishan samples, the relatively high $^{87}\text{Sr}/^{86}\text{Sr}$ ratios point to equally poor fidelity (Liu et al., 2013; Liu et al., 2018). In contrast, the lack of radiogenic Sr isotope variability observed for the Dajiang leachates indicates no post-depositional overprinting.

Bulk rocks and meteoric waters typically exhibit a limited range of $\delta^{44/40}\text{Ca}$ and $\delta^{88/86}\text{Sr}$ values (Fantle and Tipper, 2014; Pearce et al., 2015), but carbonate rocks have much higher Ca and Sr concentrations than water. Therefore, large amounts of water are required to significantly reset carbonate $\delta^{44/40}\text{Ca}$ and $\delta^{88/86}\text{Sr}$ values during post-depositional diagenesis, assuming negligible isotopic fractionation occurs during recrystallization and secondary carbonate formation. Neither the Meishan sequential leachates nor those for Dajiang exhibited significant $\delta^{44/40}\text{Ca}$ and $\delta^{88/86}\text{Sr}$ variability. Thus, if the Meishan $^{87}\text{Sr}/^{86}\text{Sr}$ ratios reflect late-stage alteration, then the corresponding impact on stable Ca and Sr isotope ratios must have been too small to explain the apparent delta value offset between the records generated from the two sections, but was possibly large enough to cause small-scale differences in their relative trends.

2.5.2 Spatial variation of bulk carbonate fractionation factors

A diagenetic interpretation for the dataset implies that primary calcite and aragonite always precipitate with the lowest possible $\delta^{44/40}\text{Ca}$ and $\delta^{88/86}\text{Sr}$ values, the isotopic compositions are the same everywhere the minerals form, and trends toward higher values reflect increasing degrees of alteration. An altogether different interpretation emerges from a hypothesis that we find difficult to disprove, namely that bulk carbonate fractionation factors spatially vary for several reasons inherent to how the ‘carbonate factory’ works. Primary carbonate producers have widely varying

Ca and stable Sr isotope ratios (Böhm et al., 2012; Raddatz et al., 2013; Gussone and Dietzel, 2016; Fruchter et al., 2016; Müller et al., 2018) and inhabit different ecological niches (Scholle et al., 1983; Morse and Mackenzie, 1990; Pomar and Hallock, 2008). Simply given these observations, we find little reason to expect that the Meishan and Dajiang sections should express identical bulk fractionation factors. The two sections clearly comprise different carbonate rocks that formed in distinct depositional environments. They also bear unique fossil assemblages (see Section 2.2) that must have contributed to local sediment accumulation.

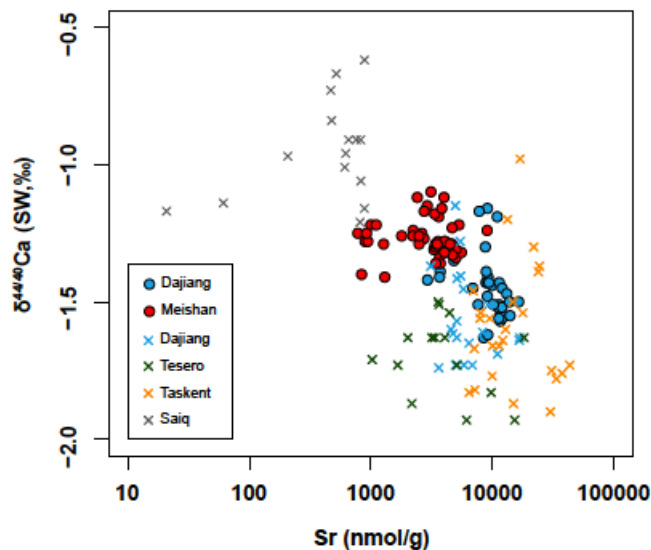


Figure 2-7 Cross-plot of $\delta^{44/40}\text{Ca}$ vs Sr concentrations (logarithmic scale). Linear and SMA regression for linear-log regression models (after logarithmic transformation of [Sr]) yield weak/no statistical correlations (All sections: $n = 179$, linear regression: $R^2 = 0.34$, p -value < 0.001 ; SMA regression: $R^2 = 0.32$, p -value < 0.001 ; Spearman's $\rho = -0.56$; Excluding Saiq: $n = 160$, linear regression: $R^2 = 0.16$, p -value = 0.005; SMA regression: $R^2 = 0.16$, p -value = 0.005; Spearman's $\rho = -0.39$). Symbols and descriptions same as Figure 2-6.

Mineralogy provides a first-order control on the isotopic composition of primary carbonate producers. Aragonitic organisms generally have lower $\delta^{44/40}\text{Ca}$ values than calcitic organisms, although wide ranges exist because species-specific differences in biocalcification pathways affect isotopic fractionation (e.g., Gussone et al., 2005; Gussone and Dietzel, 2016). Moreover, for any

given organism, shifts in Ca and Sr isotope fractionation stem from biological responses to local seawater conditions, such as temperature, salinity, ionic strength, and dissolved carbonate geochemistry, with some parameters exerting a greater influence than others (Böhm et al., 2006; Böhm et al., 2012; Heinemann et al., 2008; Griffith et al., 2008; Gussone et al., 2009; Allmen et al., 2010; Gussone and Filipsson, 2010; Kısakürek et al., 2011; Raddatz et al., 2013; Hippler et al., 2013; Inoue et al., 2015; Gothmann et al., 2016; Gussone and Dietzel, 2016; Fruchter et al., 2016; Müller et al., 2018; Mejía et al., 2018; Gussone and Greifelt, 2019). Therefore, it is not surprising that local variations in bulk fractionation factors arise from physically mixing carbonate detritus derived from different sources (Farkaš et al., 2016; Lau et al., 2017; Jost et al., 2017). The basic premise of our argument also applies to elemental distribution coefficients, which control Sr concentrations and Sr/Ca ratios, for example. Under ideal circumstances, simple mixing between aragonite and calcite end-members should yield a linear relationship between $\delta^{44/40}\text{Ca}$ and [Sr] (e.g., Farkaš et al., 2016), but the combination of species-specific vital effects and physical mixing could explain why such correlations are elusive when comparing bulk carbonate records at a global scale (e.g., Figure 2-7).

With the aid of the high-precision stable isotope and geochronologic methods employed in this study and previous works (e.g., Bowring et al., 1998; Shen et al., 2011; Burgess et al., 2014), we can examine small isotopic signals (many confirmed with repeat measurements; see Section 2.4.1) relative to larger ones to identify how different mechanisms of change manifest in the end-Permian rock record at various temporal resolutions. The conceptual model presented here suggests that the Meishan and Dajiang $\delta^{44/40}\text{Ca}$ and $\delta^{88/86}\text{Sr}$ records can synchronously shift relative to different average background values. Indeed, Ca isotope ratios in both records increase by $\sim 0.15\text{‰}$ to 0.20‰ toward the PTB and decrease by $\sim 0.20\text{‰}$ thereafter. These trends span different

lithologies, which provides evidence that the species-specific calcification mechanisms composing the bulk fractionation factors shared some commonalities and similarly responded to the same global drivers. At the same time, the two records clearly diverge in discrete intervals. Before the EXT level, both records show complementary $\delta^{44/40}\text{Ca}$ values, but after this point, Dajiang exhibits an $\sim 0.50\text{‰}$ decrease while the trend spanning Bed 24e through most of Bed 26 at Meishan is muted. A similar dichotomy exists for $\delta^{88/86}\text{Sr}$. These instances of incoherency are consistent with fluid-buffered early diagenesis, late stage diagenesis, or some combination thereof at Meishan.

The concept of active versus passive tracers (e.g., Fantle, 2010) further supports our interpretations. The bulk carbonate samples examined in this study represent an active tracer, while the hydroxyapatite microfossils studied in Hinojosa et al. (2012) represent a passive tracer. Figure 2-3 compares the bulk carbonate Ca isotope records for Meishan and Dajiang with the hydroxyapatite Ca isotope record for Meishan. Synchronous shifts in the carbonate and hydroxyapatite records (e.g., negative excursions between the EXT level and PTB) preclude local mineralogical changes and diagenetic alteration as explanations for the trends and point more toward a change in the isotopic composition of seawater (Payne et al., 2010; Hinojosa et al., 2012; Silva-Tamayo et al., 2018), whereas asynchronous shifts in the carbonate records (e.g., Beds 24e and Bed 26 at Meishan) provide evidence for syn- or post-depositional modification.

For the present dataset, we observe smaller isotopic shifts defined by multiple data points, which appear superimposed on the longer-term stratigraphic trends. The Ca isotope data straddling the PTB provide a good example. Changes in fractionation due to any number of environmental, biological, or sedimentological fluctuations offer one explanation. Greater scatter at Meishan may reflect variable degrees of dolomitization, although stable Sr isotope ratios show less scatter in the same interval. This may imply that $\delta^{88/86}\text{Sr}$ values are less vulnerable to dolomitization, but more

research is needed to understand the behavior of stable Sr isotopes during all aspects of diagenesis.

Lastly, fine-scale noise is evident throughout the records. Bed 24e at Meishan, for instance, shows Ca isotope oscillations on the order of 0.10‰. These oscillations could reflect small fluctuations in early diagenetic conditions between fluid- and rock-buffered, or similarly small shifts in fractionation. The stochasticity of primary carbonate formation provides another explanation. We expect primary calcite and aragonite to inherently display a distribution of isotopic and elemental abundances, even when the minerals form under relatively constant background conditions.

More broadly, our conceptual model allows for differing interpretations of Ca and stable Sr isotope records throughout geologic time given evolutionary constraints on carbonate production pathways and products. Ocean acidification, for example, is predicted to decrease precipitation rates (Doney et al., 2009; Kump et al., 2009; Hönisch et al., 2012; Zeebe, 2012), which should decrease the magnitude of the Ca and Sr isotope fractionation factors (Tang et al., 2008; DePaolo, 2011; Nielsen et al., 2012; Watkins et al., 2017) and cause positive isotope excursions. Such an explanation has been invoked to explain an ~0.10‰ to 0.15‰ increase in $\delta^{44/40}\text{Ca}$ values during the ~40 to 55 kyr onset of OAE 2 in the late Cretaceous (Du Vivier et al., 2015), but presently seems less applicable to the end-Permian, which exhibits an ~0.30‰ decrease over roughly the same timeframe. The difference might reflect the fundamentally different biology of the end-Permian ocean (e.g., Bambach, 2006; Knoll et al., 2007; Payne and Clapham, 2013), among many other factors. Similar arguments arise when comparing the end-Permian to the Ediacaran, although it is interesting to consider that outcrops reflecting local variations in bulk fractionation factors and elemental distribution coefficients can also be modeled as a continuum of data points plotting along a diagenetic mixing curve.

2.5.3 Variations in input and output fluxes: Role of sea level fall

The evidence considered to this point suggests that the Ca and Sr isotope records from Dajiang are reasonably pristine and free from diagenetic overprinting, but we have not identified a mechanism that satisfactorily explains the negative $\delta^{44/40}\text{Ca}$ and $\delta^{88/86}\text{Sr}$ excursions that occur in the <60 kyr interval between the EXT level and the PTB. Here, we consider whether the excursions represent a rapid change in seawater geochemistry due to variations in global input and output fluxes. Over timescales shorter than the residence time of Ca in seawater (~1 Myr; Schmitt et al., 2003; Farkaš et al., 2007; Holmden et al., 2012; Fantle and Tipper, 2014), the elevation of weathering inputs over carbonate output can produce transient, negative isotope excursions (Fantle and Depaolo, 2005; Fantle, 2010; Blättler et al., 2011). Similar behavior is expected for $\delta^{88/86}\text{Sr}$, given present understanding about the marine stable Sr isotope budget (Krabbenhöft et al., 2010; Vollstaedt et al., 2014; Pearce et al., 2015).

However, important questions exist about the magnitude of isotopic excursions that flux imbalances can produce, or more fundamentally, whether significant imbalances in the marine Ca cycle can persist in the first place. Employing a typical mass-balance model, where the carbonate output flux is prescribed as a function of seawater calcium concentrations, Payne et al. (2010) proposed that the negative $\delta^{44/40}\text{Ca}$ excursion at Dajiang represents a relatively large decrease in carbonate output due to ocean acidification, combined with a more modest increase in the chemical weathering input. More recently, Komar and Zeebe (2016) pointed out that the carbonate burial flux depends on the calcite saturation state, which is proportional to the product of both Ca^{2+} and CO_3^{2-} concentrations. Because seawater CO_3^{2-} concentrations are much lower than those for Ca^{2+} , the former exerts a much stronger control on the output flux than the latter. Therefore, in coupled Ca-C models, the burial flux rapidly responds to elevated riverine inputs, which reduces the flux

imbalance and dampens the magnitude of the resulting isotopic excursion. Ocean acidification can lead to no carbonate burial, but coupled Ca-C models still predict smaller imbalances compared to Ca-only models (Komar and Zeebe, 2016).

The Dajiang $^{87}\text{Sr}/^{86}\text{Sr}$ record further constrains how chemical weathering either did or did not respond across the event. The flat trend precludes changes in the magnitude and isotopic composition of the silicate weathering contribution, in good agreement with recent research arguing that silicate weathering rates during the end-Permian were exceptionally low due to prevailing transport-limited conditions (Kump, 2018). The record also implies no increase in the hydrothermal flux, nor a substantial shift in the radiogenic Sr isotope composition of the carbonate weathering flux.

Few chemical weathering studies have considered that the late Permian is associated with one of the lowest sea levels during the entire Phanerozoic Eon (e.g., Holser and Magaritz et al., 1989; Hallam, 1992; Haq and Schutter, 2008). A tectonically-induced global lowstand (Hallam, 1992; Miller et al., 2005; Haq and Schutter, 2008) made the end-Permian particularly susceptible to rapid oscillations in sea level (Holser and Magaritz et al., 1987; Holser et al., 1989; Erwin, 1990). Glacioeustatic fluctuations may have played a role (Erwin, 1990; Campbell et al., 1992; Baresel et al., 2017) despite evidence for prevailing greenhouse conditions (Cui and Kump, 2015). Detailed stratigraphic studies of globally distributed sections indicate that the latest Permian (mid-late Changhsingian) coincided with a maximum sea level fall on the order of 280 m (Holser and Magaritz et al., 1987; Holser et al., 1989; Campbell et al., 1992; Yin et al., 2014). A compelling correspondence between the $\delta^{44/40}\text{Ca}$ and $\delta^{88/86}\text{Sr}$ records and the record of sea level variation for the end-Permian (Figure 2-2) leads us to hypothesize that the regression facilitated the subaerial exposure and weathering of shelf carbonates bearing low $\delta^{44/40}\text{Ca}$ and $\delta^{88/86}\text{Sr}$ values but the same

$^{87}\text{Sr}/^{86}\text{Sr}$ ratio as contemporaneous seawater.

Previous attempts to model the negative $\delta^{44/40}\text{Ca}$ excursion expressed at Dajiang and other sections assumed a fixed isotopic composition for the riverine input (Payne et al., 2010; Komar and Zeebe, 2016; Silva-Tamayo et al., 2018). This assumption is reasonable given that no chemical weathering studies have identified mechanisms that can substantially alter the Ca and stable Sr isotope composition of global riverine runoff, especially over short timescales. However, the subaerial exposure of shelf carbonates during large and rapid sea level fall provides one key exception.

Carbonate weathering occurs quickly, and elevated $p\text{CO}_2$ from the Siberian Traps eruption may have accelerated dissolution rates. Today and during times of aragonitic seas (Sandberg, 1983), shelf carbonates predominantly comprise aragonite (Stoll and Schrag, 1998), which has relatively low $\delta^{44/40}\text{Ca}$ and $\delta^{88/86}\text{Sr}$ values (Gussone et al., 2005; Blättler et al., 2012; Gussone and Dietzel, 2016; Gussone et al., 2016; AlKhabit et al., 2017a, b; Pruss et al., 2018) but the same $^{87}\text{Sr}/^{86}\text{Sr}$ ratio as contemporaneous seawater. Shelf carbonate weathering therefore satisfies the observation that $\delta^{44/40}\text{Ca}$ and $\delta^{88/86}\text{Sr}$ values decreased across the event while $^{87}\text{Sr}/^{86}\text{Sr}$ ratios remained unchanged. A higher Sr flux due to more aragonite weathering (Stoll and Schrag, 1998) also explains why Sr/Ca ratios at Dajiang (and Meishan) increased over the same interval.

Komar and Zeebe (2016) calculated that an $\sim 0.15\%$ increase in Ca isotope fractionation between seawater and carbonate is required to explain the Dajiang $\delta^{44/40}\text{Ca}$ record. However, the authors assumed that reduced saturation increases the magnitude of the fractionation factor, whereas considerable evidence points to the opposite relationship (see Silva-Tamayo et al., 2018). Our hypothesis eliminates the need for increased fractionation because a higher Ca flux from the dissolution of aragonite bearing low $^{44}\text{Ca}/^{40}\text{Ca}$ ratios could have shifted the $\delta^{44/40}\text{Ca}$ value of the

global weathering flux downward by 0.15%. Previous studies examining Ca isotope cycling near Florida Bay and Punta Maroma, Mexico have deduced that sea level fall and subsequent weathering of coastal marine carbonate successions could decrease the isotopic composition of the global weathering flux (Holmden et al., 2012). However, the exact implications for the present study are challenging to quantify for a few different reasons. One is that elevated saturation due to higher alkalinity inputs from carbonate weathering could have increased the magnitude of the fractionation factor (Teng et al., 2008; Nielsen et al., 2012). Another pertains to local inputs from rivers (Shao et al., 2018) and submarine groundwater discharge (Holmden et al., 2012). Finally, submarine carbonate dissolution due to ocean acidification (Payne et al., 2010) may have contributed complementary effects and cannot be completely discounted, even if the marine Ca cycle remained closer to steady-state than previously anticipated.

Diminution of the shelf carbonate input during subsequent sea level rise provides the most straightforward explanation for the increase in $\delta^{44/40}\text{Ca}$ and $\delta^{88/86}\text{Sr}$ values toward the PTB, especially given lithological evidence for rising sea level in the earliest Griesbachian (Wignall and Hallam, 1992, 1993; Yin et al., 2014). Nonetheless, other hypotheses exist. For example, the aftermath of enhanced carbonate weathering represents a state of disequilibrium between riverine inputs and carbonate output that causes alkalinity to accumulate in seawater (Higgins and Schrag, 2003; Kump et al., 2009; Cui et al., 2013; Penman et al., 2016). So-called “alkalinity overshoots” are eventually overcome through extensive carbonate deposition (Caldeira and Rampino, 1993; Opdyke and Wilkinson, 1993). Global carbon cycle models commonly yield “alkalinity overshoots” (e.g., Cui et al., 2013), and many field studies focused on the earliest Triassic have documented evidence for increased microbial carbonate precipitation and inorganic carbonate accumulation in the form of oolites and carbonate cements (e.g., Reinhardt, 1988; Schubert and

Bottjer, 1992; Lehrmann et al., 2003). The elevation of carbonate output over weathering inputs can produce transient, positive $\delta^{44/40}\text{Ca}$ excursions (Fantle and Depaolo, 2005; Fantle, 2010), although improvements to coupled Ca-C models are required to estimate the exact magnitude of the isotopic effect.

2.6 Conclusion

We used high-precision TIMS methods to generate $\delta^{44/40}\text{Ca}$, $\delta^{88/86}\text{Sr}$, and $^{87}\text{Sr}/^{86}\text{Sr}$ records for two carbonate successions in south China that span the latest Permian to earliest Triassic, with the ultimate aim of better understanding how Ca and Sr isotopes behave during periods of profound biological and environmental change. The Dajiang section shows negative $\delta^{44/40}\text{Ca}$ and $\delta^{88/86}\text{Sr}$ excursions, as well as low and invariant $^{87}\text{Sr}/^{86}\text{Sr}$ ratios, in the <60 kyr interval between the onset of the mass extinction and the Permian-Triassic boundary. The Meishan section shows higher $\delta^{44/40}\text{Ca}$ and $\delta^{88/86}\text{Sr}$ values, which variably define coherent and incoherent secular trends relative to Dajiang. In addition, $^{87}\text{Sr}/^{86}\text{Sr}$ ratios at Meishan are much higher and do not define an obvious pattern. To explain the dataset, we considered several primary and secondary processes that control the Ca and Sr isotope composition of carbonate sediment and operate over varying spatial and temporal scales. We conclude that the Dajiang records are reasonably primary and preserve information about the geochemistry of end-Permian seawater. The Meishan $\delta^{44/40}\text{Ca}$ and $\delta^{88/86}\text{Sr}$ records offer complementary insights when compared to other records, but must be interpreted cautiously given evidence for early and late stage diagenetic overprinting. The Meishan $^{87}\text{Sr}/^{86}\text{Sr}$ record is clearly consistent with late stage alteration.

The end-Permian is associated with one of the largest regressions during the Phanerozoic, but this detail has been largely overlooked in previous Ca isotope studies. Enhanced weathering of aragonitic shelf carbonates during sea level fall provides a straightforward mechanism for

rapidly decreasing seawater $\delta^{44/40}\text{Ca}$ and $\delta^{88/86}\text{Sr}$ values while maintaining constant $^{87}\text{Sr}/^{86}\text{Sr}$ ratios. The $\delta^{44/40}\text{Ca}$ and $\delta^{88/86}\text{Sr}$ proxies may be able to trace large and rapid glacioeustatic fluctuations in sea level during other times in Earth history. In the case of the end-Permian, enhanced weathering of shelf carbonates has implications for estimating the magnitude of the CO_2 input from the Siberian Traps eruption using C isotope mass-balance mixing models.

CHAPTER 3

STABLE CA AND SR ISOTOPES SUPPORT VOLCANICALLY-TRIGGERED BIOCALCIFICATION CRISIS DURING OCEANIC ANOXIC EVENT 1A

This chapter was accepted for publication in Geology: Wang, J., Jacobson, A.D., Sageman, B.B., Hurtgen, M.T., 2021. Stable Ca and Sr isotopes support volcanically-triggered biocalcification crisis during Oceanic Anoxic Event 1a

3.1 Introduction

Large Igneous Province (LIP) eruptions correlate with mass extinction and biotic turnover events throughout Earth history (Rampino et al., 2019). OAE 1a during the early Aptian (~120 Ma) represents a prime example. OAE 1a correlates with emplacement of the Ontong Java Plateau (Bottini et al., 2012), and the fossil record reveals abrupt decreases in the production rate and species abundance of calcareous nannoplankton, collectively termed the ‘nannoconid crisis’ (Erba et al., 2010). A ~2‰ negative carbon isotope ($\delta^{13}\text{C}$) excursion immediately followed by a prolonged ~3‰ positive shift (Jenkyns and Wilson, 1999) further indicates extreme environmental disruption.

Biocalcification crises have potential to produce positive calcium isotope ($\delta^{44/40}\text{Ca}$) excursions in the rock record. This hypothesis derives from observations that the carbonate Ca isotope fractionation factor is sensitive to precipitation rate, with slower rates yielding higher $\delta^{44/40}\text{Ca}$ values and vice versa for faster rates (Tang et al., 2008; Alkhatib and Eisenhauer, 2017; Mejía et al., 2018). Nonetheless, uncertainty surrounds the exact Ca isotope signature of LIP volcanism. $\delta^{44/40}\text{Ca}$ records generated for OAE 2 (~94 Ma, correlative with the Caribbean LIP) and the end-Cretaceous (~66 Ma, correlative with the Deccan Traps LIP) show positive excursions (Du Vivier et al., 2015; Linzmeier et al., 2020), while those spanning the Permian-Triassic

Boundary (~252 Ma, correlative with the Siberian Traps LIP) yield negative shifts (Payne et al., 2010; Wang et al., 2019). Complexity arises because different mechanisms of change yield similar isotopic patterns. Fluid-buffered recrystallization (Higgins et al., 2018), aragonite neomorphism (Ahm et al., 2018), and carbonate polymorph mixing (Lau et al., 2017) can simulate rate-dependent shifts in fractionation. Excursions may also reflect variations in seawater $\delta^{44/40}\text{Ca}$ due to transient flux imbalances between carbonate output and total chemical weathering inputs (Payne et al., 2010), as well as shifts in the $\delta^{44/40}\text{Ca}$ of riverine runoff (Wang et al., 2019).

Stable strontium isotope ($\delta^{88/86}\text{Sr}$) measurements can help resolve the origin of $\delta^{44/40}\text{Ca}$ signals. Similar to Ca isotopes, carbonate minerals preferentially incorporate lighter Sr isotopes with fractionation factors that inversely correlate with precipitation rate and approach zero at chemical equilibrium (Böhm et al., 2012; Stevenson et al., 2014; AlKhatib and Eisenhauer, 2017). However, unlike $\delta^{44/40}\text{Ca}$, $\delta^{88/86}\text{Sr}$ is less susceptible to diagenetic overprinting (Voigt et al., 2015) because recrystallizing minerals reject Sr from their lattices (Baker et al., 1982) with minimal reuptake from pore fluids (Richter and DePaolo, 1988; Richter and Liang, 1993; Voigt et al., 2015). Moreover, flux imbalances drive $\delta^{88/86}\text{Sr}$ excursions in the same directions as those for $\delta^{44/40}\text{Ca}$, but $^{87}\text{Sr}/^{86}\text{Sr}$ ratios determined as part the $\delta^{88/86}\text{Sr}$ method can further distinguish the relative dominance of riverine versus hydrothermal fluxes (e.g., Vollstaedt et al., 2014; Wang et al., 2019). To test these hypotheses, we measured the stable Ca and Sr isotope compositions of bulk carbonate samples across OAE 1a collected from Hole 866A of the Ocean Drilling Program Leg 143.

3.2 Geological setting

Hole 866A was drilled on the flanks of Resolution Guyot (21°N, 174°E) in the mid-Pacific. The core comprises ~1600 m of shallow-water carbonate strata spanning the Barremian (~127 Ma) to the Albian (~99 Ma; Jenkyns and Wilson, 1999). During the early Cretaceous, the guyot was

located in the southern tropical Pacific and accumulated a shallow-water platform facies (Figure 3-1A, Jenkyns and Wilson, 1999). Cyclic packstone–wackestones and oolitic/peloidal grainstones dominate the lithology, and the rocks primarily contain calcite (Jenkyns and Strasser, 1995). See Appendix II for more information.

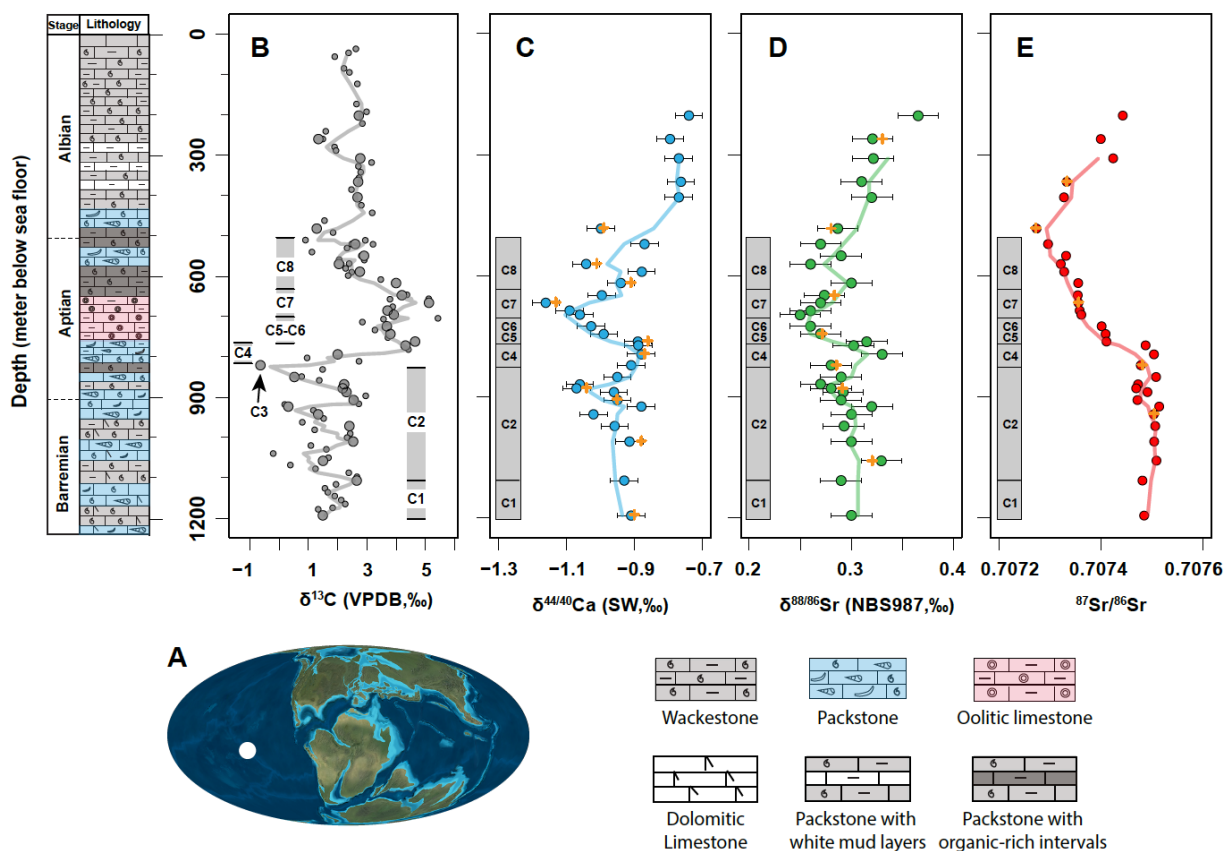


Figure 3-1 (A) Paleogeographic location of Resolution Guyot during the Early Cretaceous modified after Blättler et al. (2011), (B) $\delta^{13}\text{C}$, (C) $\delta^{44/40}\text{Ca}$, (D) $\delta^{88/86}\text{Sr}$, and (E) $^{87}\text{Sr}/^{86}\text{Sr}$ records. Fitted lines show 3-point moving averages. In B, large circles represent data from this study while small circles show data from Mills et al. (2017). In C, D, and E, orange crosses denote duplicate measurements, and error bars represent analytical uncertainties assigned to the measurements. Gray bars (C1-C8) show the $\delta^{13}\text{C}$ segmentation. See the Appendix II for more details. VPDB—Vienna Peedee belemnite; SW—OSIL seawater standard; NIST987—NIST SRM-987 strontium carbonate standard.

3.3 Methodology

Samples (n=33) were analyzed at Northwestern University. Elemental concentrations

determined by ICP-OES have an uncertainty of $\pm 5\%$ or less. $\delta^{13}\text{C}$ and $\delta^{18}\text{O}$ were analyzed using an IRMS equipped with a gas bench. Data are reported relative to VPDB with uncertainties ($2\sigma_{\text{SD}}$) of $\pm 0.12\text{‰}$ ($\delta^{13}\text{C}$) and $\pm 0.30\text{‰}$ ($\delta^{18}\text{O}$). $\delta^{44/40}\text{Ca}$, $\delta^{88/86}\text{Sr}$, and $^{87}\text{Sr}/^{86}\text{Sr}$ were measured using high-precision TIMS techniques. $\delta^{44/40}\text{Ca}$ and $\delta^{88/86}\text{Sr}$ are reported relative to OSIL seawater (SW) and NBS-987, respectively. Uncertainties ($2\sigma_{\text{SD}}$) are $\pm 0.05\text{‰}$ ($\delta^{44/40}\text{Ca}$), $\pm 0.02\text{‰}$ ($\delta^{88/86}\text{Sr}$), and ± 0.000010 ($^{87}\text{Sr}/^{86}\text{Sr}$). See Appendix II for more information, including data (Table AII-1) and supporting diagrams (Figures AII-1 – AII-3).

3.4 Results

The $\delta^{13}\text{C}$ profile exhibits a distinctive negative excursion followed by a prolonged positive shift, consistent with previously published records for OAE 1a (Figure 3-1; Jenkyns and Wilson, 1999). Measured $\delta^{44/40}\text{Ca}$ range from -0.74‰ to -1.16‰ , with an average of -0.94‰ . Values are higher before OAE 1a than immediately after, similar to results reported elsewhere (Blättler et al., 2011). However, all data presented in Blättler et al. (2011) are lower (Figure AII-4; see section 4.1 in Du Vivier et al., 2015), and the high-precision TIMS methodology employed here resolves several oscillations, including a negative shift prior to OAE 1a (C2), a positive shift that begins before and peaks within the event (C4-5), a negative shift after the event (C6-7), and a longer-term recovery to near-starting values (C8). Measured $\delta^{88/86}\text{Sr}$ range from 0.25‰ to 0.37‰ , with an average of 0.29‰ . The $\delta^{44/40}\text{Ca}$ and $\delta^{88/86}\text{Sr}$ records mimic each other but markedly differ from the $^{87}\text{Sr}/^{86}\text{Sr}$ record, which begins at ~ 0.70751 and gradually decreases to a minimum of 0.70727 , identical to the global record (Paull et al., 1995).

3.5 Discussion

3.5.1 Early Diagenesis

Lack of correlation between $\delta^{13}\text{C}$ and $\delta^{18}\text{O}$ supports absence of diagenesis after lithification

(Figure AII-2; Jenkyns and Wilson, 1999), but Hole 866A sediments likely experienced some degree of recrystallization before lithification (Paull et al., 1995). Fluid-buffered syn-depositional diagenesis can elevate carbonate $\delta^{44/40}\text{Ca}$ values, especially in platform environments (e.g., Higgins et al., 2018). Significant isotopic resetting is possible because primary carbonate producers preferentially incorporate lighter Ca isotopes, while little to no fractionation occurs when recrystallizing sediments subsequently equilibrate with seawater (Fantle and DePaolo, 2007). Given that recrystallizing sediments also experience net Sr loss (e.g., Baker et al., 1982; Richter and DePaolo, 1988; Richter and Liang, 1993), negative correlations between $\delta^{44/40}\text{Ca}$ and [Sr] represent one potential consequence of early diagenetic alteration (Lau et al., 2017; Ahm et al., 2018).

The 866A samples display such a pattern (Figure 3-2A), but the exact interpretation is ambiguous. Although the slope of the line is identical to that expected for precipitation rate-dependent shifts in Ca isotope fractionation and Sr partitioning between calcite and water (Figure 3-2A; Tang et al., 2008), other research has theorized that fluid-buffered recrystallization can produce the same trend (Ahm et al., 2018). In the absence of secondary alteration, the intercept should recover the $\delta^{44/40}\text{Ca}$ of the fluid from which the minerals formed (Tang et al., 2008). Carbonates spanning the Ludfordian (Silurian) also yield the ‘kinetic slope,’ and these data were used to argue that contemporaneous seawater had a $\delta^{44/40}\text{Ca}$ of -0.92‰ (Farkaš et al., 2016). Our data similarly suggest that early-Cretaceous seawater had a $\delta^{44/40}\text{Ca}$ of $-0.64\pm 0.06\text{‰}$. However, this interpretation does not account for the hypothesis that the sediments recrystallized under rock-buffered conditions, whereby calcite simply lost Sr with minimal Ca isotope resetting (Higgins et al., 2018). Rather than the isotopic composition of seawater, the intercept could be interpreted as the $\delta^{44/40}\text{Ca}$ of pore fluid (presumably a mixture between seawater Ca and Ca from carbonate

dissolution), but equilibration with this end-member implies that samples with the highest $\delta^{44/40}\text{Ca}$ underwent nearly complete Ca isotope exchange. No other proxies support such extensive diagenetic overprinting.

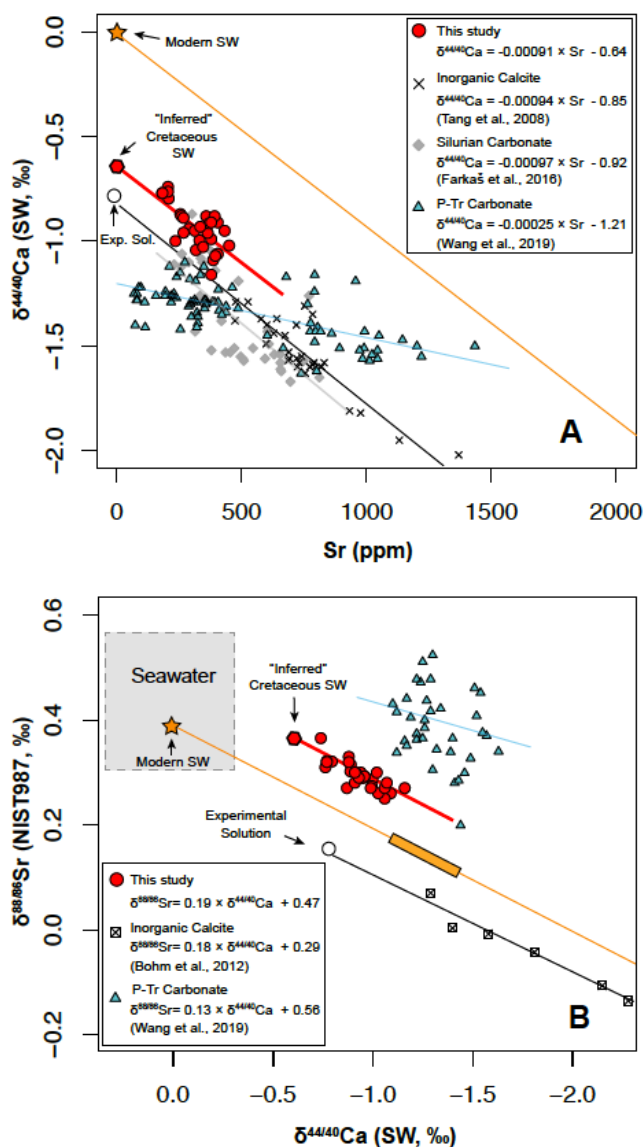


Figure 3-2 Cross-plots of (A) $\delta^{44/40}\text{Ca}$ vs. $[\text{Sr}]$ and (B) $\delta^{44/40}\text{Ca}$ vs. $\delta^{88/86}\text{Sr}$. Grey box shows approximate range of seawater $\delta^{44/40}\text{Ca}$ and $\delta^{88/86}\text{Sr}$ based on measurements and modeling (Vollstaedt et al., 2014; Blättler and Higgins, 2017). Orange lines denote kinetic relationship between modern seawater and marine carbonates predicted from Tang et al. (2008) (in A) and Böhm et al. (2012) (in B). Orange bar in B shows approximate range of modern calcite fractionation factors. See text for explanation of the inferred Cretaceous seawater end member.

Linear correlations for measured data are found at the significance level of 0.01. See the Appendix II for more details. P-Tr—Permian-Triassic; SW—OSIL seawater standard; NIST987—NIST SRM-987 strontium carbonate standard.

3.5.2 Chemical Weathering

High $p\text{CO}_2$ and warm temperatures characterized the early Aptian (e.g., Naafs et al., 2016). Previously published $\delta^{44/40}\text{Ca}$, $\delta^7\text{Li}$, and $^{187}\text{Os}/^{188}\text{Os}$ records suggest that greenhouse conditions accelerated the hydrological cycle and increased weathering rates (Figure 3-3; Blättler et al., 2011; Bottini et al., 2012; Lechler et al., 2015). At Cismon, for example, enhanced terrestrial weathering explains correspondence between a positive $^{187}\text{Os}/^{188}\text{Os}$ spike and the well-known negative $\delta^{13}\text{C}$ spike preceding OAE 1a (Tejada et al., 2009; Bottini et al., 2012). Negative $\delta^{44/40}\text{Ca}$ and $\delta^{88/86}\text{Sr}$ excursions within the same interval (Figure 3-3) appear consistent with a transient weathering pulse, yet the increased riverine fluxes required to produce these trends should correspond to a positive $^{87}\text{Sr}/^{86}\text{Sr}$ shift, for which no evidence exists (Figure 3-1). In general, flux imbalances cannot shift $\delta^{44/40}\text{Ca}$ and $\delta^{88/86}\text{Sr}$ on the same timescale as $^{187}\text{Os}/^{188}\text{Os}$ because the former elements have long residence times and their mixing end-members have limited isotopic contrast (e.g., Holmden et al., 2012).

3.5.3 Kinetic Effects

On a diagram of $\delta^{44/40}\text{Ca}$ vs. $\delta^{88/86}\text{Sr}$ (Figure 3-2B), the Hole 866A samples define a line with a slope of 0.194 ± 0.027 , which is the slope expected when the Ca and Sr isotope fractionation factors vary with the rate of calcite precipitation (Böhm et al., 2012). Unlike correlations between $\delta^{44/40}\text{Ca}$ and $[\text{Sr}]$ (Figure 3-2A), diagenesis is less likely to simulate rate-dependent shifts between $\delta^{44/40}\text{Ca}$ and $\delta^{88/86}\text{Sr}$. Strontium isotope equilibration with pore fluids occurs during recrystallization, but the effect only shifts carbonate $^{87}\text{Sr}/^{86}\text{Sr}$ by 10 - 50 ppm because carbonates lose much more Sr than they gain (Baker et al., 1982; Richter and DePaolo, 1988). The exchange

rate rapidly decreases with sediment age (Richter and Liang, 1993), such that in the modern-day, the ongoing release of Sr from Resolution Guyot limestone lowers pore fluid $^{87}\text{Sr}/^{86}\text{Sr}$ relative to seawater, as opposed to uptake of pore fluid Sr elevating carbonate $^{87}\text{Sr}/^{86}\text{Sr}$ (Figure AII-5; Paull, 1995). The calcite-water equilibrium fractionation factor characterizing the stable Sr isotope system equals $\pm 0\text{‰}$ (Böhm et al., 2012), similar to the Ca isotope system (Fantle and DePaolo, 2007; Jacobson and Holmden, 2008). Therefore, the complementary effect of isotope exchange on carbonate $\delta^{88/86}\text{Sr}$ values is predictably negligible because the fractionated mixing end-members have less contrast (Figure AII-6; see Appendix II). Uptake of lighter Sr isotopes during rapid formation of secondary calcite can elevate pore fluid $\delta^{88/86}\text{Sr}$, but bulk carbonates are not affected because the amount of Sr incorporated is minor (Voigt et al. 2015). We conclude that the $\delta^{44/40}\text{Ca}$ and $\delta^{88/86}\text{Sr}$ records reflect primary, precipitation rate-dependent effects, which further suggests that the estimated $\delta^{44/40}\text{Ca}$ of -0.64‰ for the early-Cretaceous ocean is an artifact of Sr loss at effectively constant $\delta^{44/40}\text{Ca}$.

3.5.4 Comparison to Permian-Triassic Boundary and the Modern Ocean

With the exception of the Permian-Triassic Boundary (Wang et al., 2019), no other paired $\delta^{44/40}\text{Ca}$ - $\delta^{88/86}\text{Sr}$ datasets exist for times of LIP volcanism. Considering these data together with those for OAE 1a and the modern ocean help place all results in better context. Figure 3-2B illustrates that carbonates from different time periods define kinetic mass-fractionation lines with similar slopes but different intercepts, mostly because seawater $\delta^{88/86}\text{Sr}$ appears to have gradually decreased toward the present. The weaker correlation of the PTB dataset has significance, as more scatter supports the conclusion that seawater $\delta^{44/40}\text{Ca}$ and $\delta^{88/86}\text{Sr}$ rapidly oscillated during the 60 kyr timespan that the samples represent (Wang et al., 2019). This interpretation is further supported by the $\delta^{44/40}\text{Ca}$ vs. $[\text{Sr}]$ trendline (Figure 3-2A), which fits neither a simple kinetic model where

balance. Measurements applied to other archives that elicit different fractionation patterns, such as barite and hydroxyapatite, could help resolve these questions.

3.6 Conclusions and implications

Our study has demonstrated for the first time that $\delta^{88/86}\text{Sr}$ measurements can constrain the fidelity and meaning of $\delta^{44/40}\text{Ca}$ signals archived in the carbonate rock record. For a ~27 Myr period during the early Cretaceous, shallow water carbonates that formed in the mid-Pacific acquired $\delta^{44/40}\text{Ca}$ and $\delta^{88/86}\text{Sr}$ values consistent with precipitation rate-dependent shifts in fractionation. We attribute the shifts to the dynamic interplay between LIP forcings and biocalcification feedbacks (e.g., Boudreau et al., 2018). Volcanic CO_2 emissions are expected to acidify seawater, decrease $[\text{CO}_3^{2-}]$, and lower calcification rates, thereby causing positive isotope excursions. The peak of reconstructed $p\text{CO}_2$ across OAE1a (Figure 3-3; Naafs et al., 2016) coincides with high $\delta^{44/40}\text{Ca}$ and $\delta^{88/86}\text{Sr}$, but warming, toxic metal loading, and other environmental stressors could have lowered calcification rates and produced the same effect. Decreased calcification eventually increases alkalinity, thereby leading to higher calcification rates and negative isotope excursions. LIP eruptions are also expected to enhance chemical weathering. While elevated riverine fluxes of Ca and Sr cannot drive geologically rapid $\delta^{44/40}\text{Ca}$ and $\delta^{88/86}\text{Sr}$ variations, the complementary delivery of alkalinity and nutrients could stimulate precipitation rates and cause negative isotope shifts, such as observed prior to OAE 1a. It is noteworthy that the $\delta^{44/40}\text{Ca}$ record presented here appears similar to that spanning the end-Cretaceous, including a negative-to-positive shift that precedes the main extinction horizon (Linzmeier et al., 2020). Finally, long-term recovery in the aftermath of biocalcification crises should remove excess alkalinity and produce positive isotope trends, such as observed after OAE 1a and during the earliest Danian (Linzmeier et al., 2020).

CHAPTER 4

Ca AND Sr ISOTOPIC CONSTRAINTS ON THE ORIGIN OF THE MARINOAN CAP CARBONATE

4.1 Introduction

The Marinoan glaciation occurred at the end of the Cryogenian Period (ca. 630 Ma) and represents one of the most extreme climate events in Earth's history. The aftermath of the Marinoan glaciation was characterized by a carbon cycle perturbation as recorded in the carbon isotope composition of marine carbonate (e.g., Hoffman and Schrag, 2002; Halverson et al., 2005), marine transgression (e.g., Creveling and Mitrovica, 2014), and widespread deposition of carbonate rocks (e.g., Hoffman and Li, 2009). This widespread carbonate succession directly overlies the glacial deposits and is often termed the “cap carbonate sequence”. It is composed of a globally distributed transgressive “cap dolostone” (e.g., Kennedy et al., 1996; Hoffman et al., 2007) and subsequent limestone in many places (e.g., Hoffman et al., 2011). A number of mechanisms for cap carbonate formation have been proposed, including: oceanic overturn (e.g., Kirschvink, 1992; Grotzinger and Knoll, 1995), sediment starvation (e.g., Kennedy and Christie-Blick, 2011; Wallace et al., 2019), gas hydrate destabilization (e.g., Kennedy et al., 2001), early diagenesis (e.g., Ahm et al., 2019), and water mass mixing (e.g., Higgins and Schrag, 2003; Shields, 2005).

The calcium isotope composition of Neoproterozoic cap carbonates has been widely used to investigate the processes responsible for post glacial carbonate deposition (e.g., Kasemann et al., 2005; Silva-Tamayo et al., 2010; Kasemann et al., 2014; Ahm et al. 2019; Wei et al., 2019). Secular variation in carbonate $\delta^{44/40}\text{Ca}$ can reflect seawater Ca cycle perturbations. Silva-Tamayo

et al. (2010) recognized a negative $\delta^{44/40}\text{Ca}$ shift within several globally distributed cap dolostone sequences, followed by rapid upsection recovery, and argued for a transient flux imbalance between global chemical weathering and carbonate burial rates. In spite of observed local heterogeneity in $\delta^{44/40}\text{Ca}$, Kasemann et al. (2014) similarly interpret $\delta^{44/40}\text{Ca}$ variations spanning cap carbonates as a seawater signal reflecting changes in chemical weathering rates. However, complexity arises in the interpretation when the possibility of secondary overprinting is considered. Early diagenetic processes occurring under fluid-buffered conditions are expected to elevate the $\delta^{44/40}\text{Ca}$ of bulk sediments (Higgins et al., 2018): during recrystallization, Ca isotope fractionation shrinks when carbonate precipitation approaches equilibrium (Fantle and Depaolo, 2007; Jacobson and Holmden, 2008); and during the aragonite to calcite transformation or neomorphism, the magnitude of Ca isotope fractionation in aragonite is larger than that of calcite (Gussone et al., 2016). Thus, the same observed variability in cap carbonate $\delta^{44/40}\text{Ca}$ could represent changes in diagenetic regime (fluid- versus rock-buffered) or carbonate mineralogy (calcite versus aragonite; Ahm et al., 2019). Nevertheless, carbonate $\delta^{44/40}\text{Ca}$ would directly record changes of seawater $\delta^{44/40}\text{Ca}$ under more extensive and complete diagenesis (Wei et al., 2019).

Sr, as a trace element, substitutes for Ca in the carbonate lattice (Pingitore et al., 1992). The stable isotope composition of trace Sr ($\delta^{88/86}\text{Sr}$) may help refine understanding of $\delta^{44/40}\text{Ca}$ signals because Sr isotopes behave similarly to Ca isotopes in most carbonate forming reactions (Krabbenhöft et al., 2009; Böhm et al., 2012; Stevenson et al., 2014; AlKhatib and Eisenhauer, 2017; Wang et al., 2021). Compared to $\delta^{44/40}\text{Ca}$, $\delta^{88/86}\text{Sr}$ is less susceptible to diagenetic overprinting (Voigt et al., 2015) because recrystallized minerals predominantly lose Sr during their crystal structure reordering (Richter and DePaolo, 1988; Richter and Liang, 1993). Therefore, $\delta^{88/86}\text{Sr}$ measurements could place important constraints on the processes of carbonate formation

and alteration (Wang et al., 2021). The Sr and Ca cycles share mass fluxes and intersect with the C cycle via chemical weathering and carbonate burial (Vollstaedt et al., 2014; Wang et al., 2019). The integration of $\delta^{44/40}\text{Ca}$ and $\delta^{88/86}\text{Sr}$ could also help delineate carbon cycle perturbations characterized by profound $\delta^{13}\text{C}$ variations (e.g., Kaufman and Knoll, 1995; Kaufman et al., 1997; Hoffman et al., 1998; James et al., 2001; Halverson et al., 2005; Hoffman et al., 2007). In the present study, we measured these and other geochemical proxies to investigate the processes responsible for cap carbonate formation in the aftermath of the Marinoan glaciation.

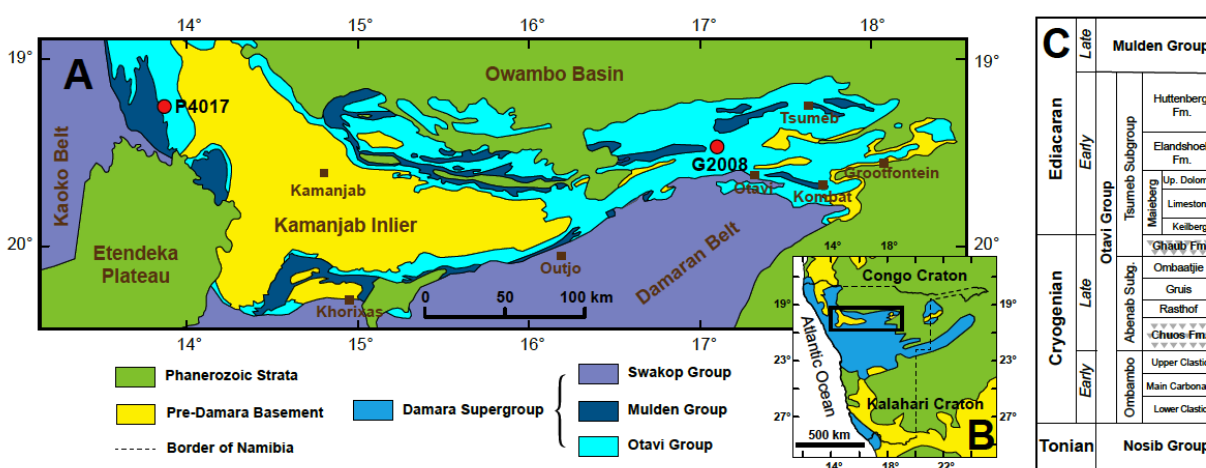


Figure 4-1 Geologic map of Namibia (A and B), locations of studied sections (shown in red circles), and stratigraphic column of Otavi Group (C).

4.2 Settings and materials

We investigated the cap carbonate sequences from the Ombaatjie (P4017) and Arbeitsgenot (G2008) sections in Namibia (Figure 4-1). The Maieberg Formation overlies the diamictitic Ghuab Formation and is comprised of a basal member of micritic dolostone with columnar stromatolitic structures and wave ripples (Keilberg cap dolostone), a middle member of limestone rhythmite, and an upper member of dolomite grainstone (Hoffman and Halverson, 2008; Hoffman et al., 2011). The two study sections are thought to have been deposited in a marine carbonate platform

situated in subtropical latitudes (Li et al., 2008), with the Arbeitsgenot section located further offshore than the Ombaatjie section (Hurtgen et al., 2006; Hoffman et al., 2011). Correlation of the two sections is adopted from previous studies using $\delta^{13}\text{C}$ chemostratigraphy (Hurtgen et al., 2006; Hoffman et al., 2007).

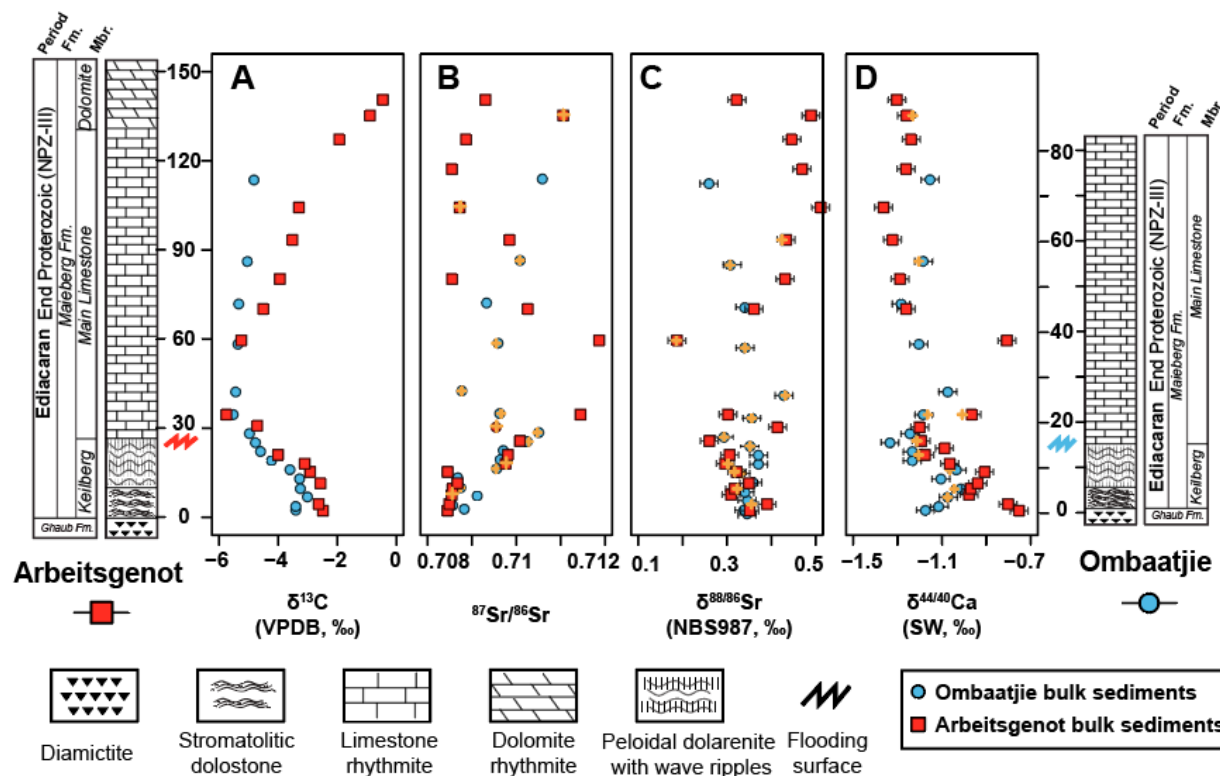


Figure 4-2 Stratigraphic correlation of (A) $\delta^{13}\text{C}$, (B) $^{87}\text{Sr}/^{86}\text{Sr}$, (C) $\delta^{88/86}\text{Sr}$, and (D) $\delta^{44/40}\text{Ca}$ records of the Maieberg Formation from the Arbeitsgenot and Ombaatjie sections, Namibia (the data series are superimposed). Filled circles denote original measurements, and orange crosses denote duplicates.

4.3 Results from the Maieberg Formation

The $\delta^{44/40}\text{Ca}$, $^{87}\text{Sr}/^{86}\text{Sr}$, and $\delta^{88/86}\text{Sr}$ values were measured at Northwestern University using high precision TIMS methodology (see Appendix III for detailed analytical methods). The $\delta^{44/40}\text{Ca}$ records of the Arbeitsgenot (n=21) and Ombaatjie (n=16) sections show an overall decreasing

pattern (Figure 4-2). Both sections show a negative shift within the Keilberg cap dolostone, a pattern consistent with other studies (e.g., Kasemann et al., 2014; Ahm et al., 2019; Wei et al., 2019). Similarly, $\delta^{88/86}\text{Sr}$ values decrease slightly within the cap dolostone and increase within the lower part of the overlying limestone. $^{87}\text{Sr}/^{86}\text{Sr}$ ratios also increase within the Keilberg cap dolostone. Dissimilarities exist between the two sections. For example, the lower part of the main limestone in the Arbeitsgenot section has a 0.25‰ larger increase in $\delta^{44/40}\text{Ca}$ and a peak in $^{87}\text{Sr}/^{86}\text{Sr}$ values, whereas $^{87}\text{Sr}/^{86}\text{Sr}$ returns to the starting value before increasing upward in the Ombaatjie section. At around the same level, $\delta^{88/86}\text{Sr}$ in the Arbeitsgenot section plummets to $\sim 0.15\text{‰}$ and then quickly increases to $\sim 0.50\text{‰}$, a value that is higher than the starting value, but generally matches the end-Ediacaran background value found in South China (Sawaki et al., 2011). $\delta^{88/86}\text{Sr}$ exhibits a slight upsection decrease in the Ombaatjie succession. The fidelity of the measured data was evaluated using various tools. The isotopic ratios of the original 5% HNO_3 leachates did not yield substantive discrepancies with those of sequential leachates (except the non-carbonate initial leachates), nor with the weighted average isotope ratios determined for all leachates combined. Furthermore, they are not likely to be affected by the radiogenic ^{40}Ca and ^{87}Sr additions (Figure AIII-1, see Appendix III for detailed evaluation).

4.4 Evaluating the calcium and strontium isotopic signals

Secondary processes may partially account for the observed complexities. Burial diagenesis has been shown to decrease Sr concentration, increase Mn and Fe concentrations, and lead to covariance of $\delta^{13}\text{C}$ and $\delta^{18}\text{O}$ (Bathurst, 1972; Brand and Veizer, 1980; Longman, 1980; Moore, 1989). Although $\delta^{13}\text{C}$ and $\delta^{18}\text{O}$ values exhibit a general correlation, the elemental abundances show mixed signals (Figure AIII-2). Within the Keilberg Member, increasing Fe concentrations and Mn/Sr ratios suggest a higher degree of diagenesis, yet higher Sr/Ca ratios

indicate better preservation. The increasing Sr/Ca and the decreasing Mn/Sr ratios also contradict the elevated Fe concentrations in the Main Limestone Member. In fact, the $\delta^{13}\text{C}$ and $\delta^{18}\text{O}$ pattern of the Maieberg Formation is reproduced in multiple Namibian sections and across the world, arguing against extensive overprinting of the Marinoan cap carbonates (e.g., Halverson et al., 2005; Hoffman et al., 2007). We note that samples located near the cap dolostone and overlying carbonate interface, which has been recognized as a flooding surface (Hoffman et al., 2007), bear higher K and Al concentrations indicating larger detrital input, which may elevate the $^{87}\text{Sr}/^{86}\text{Sr}$ ratio (Liu et al., 2014). However, the lack of variation observed in sequential leachates does not support this argument (Figure AIII-1). Moreover, Kasemann et al. (2005, 2010, 2014) suggested that the Maieberg Formation preserves primary $\delta^{11}\text{B}$, $\delta^{26}\text{Mg}$ and $\delta^{44/40}\text{Ca}$ signals by investigating multiple sections on the paleocontinental margin of the Congo craton.

The $\delta^{44/40}\text{Ca}$ value of carbonate sediments can be elevated during early diagenesis in platform environments where the sediment system is open to seawater invasion (namely fluid buffered condition, Higgins et al., 2018). Thus, the declining $\delta^{13}\text{C}$ and $\delta^{44/40}\text{Ca}$ values within the cap dolostone may reflect a change from fluid-buffered to sediment-buffered diagenetic conditions and improved preservation of geochemical signatures. This, however, is opposite to what is expected in a transgressive system like the post-Marinoan ocean (e.g., Halverson et al., 2004; Hoffmann et al., 2007; Hoffman, 2011). The pore fluids of the shelf are warmed by geothermal heat flux from the Earth's crust, or the warm atmosphere near the surface, and then replaced by inflowing cold seawater creating the so-called geothermal convection (Kohout, 1967). The expanding seawater body would increase the dipping isopycnals, enhance geothermal convection, and facilitate fluid-buffered diagenesis (e.g., Essaid, 1990; Phillip et al., 1991; Wilson, 2003, 2005). The conflicting information conveyed by the diagenesis model and rising sea-levels indicate

the change in diagenetic conditions is unlikely to have caused the excursions we observe.

In addition to recrystallization, transformation of carbonate polymorphs or neomorphism may alter sediment $\delta^{44/40}\text{Ca}$ values (Higgins et al., 2018) because Ca isotope fractionation differs between metastable aragonite and the more stable calcite (e.g., Gussone et al., 2016). The mixing of variable degrees of neomorphosed CaCO_3 in a fluid buffered system could lead to an inverse relationship between $\delta^{44/40}\text{Ca}$ and [Sr] (e.g., Husson et al., 2015; Lau et al., 2017). Based on these observations, Ahm et al (2019) utilized a reactive transport model to propose that the entire cap carbonate sequence is of early diagenetic origin and aragonite is the precursory carbonate mineral. This hypothesis is compelling as we observe samples with higher $\delta^{44/40}\text{Ca}$ exhibit lower [Sr]. However, the correlation is only observed in the Keilberg cap dolostone and not in the overlying limestone (Figure AIII-3). Moreover, in stable Sr isotope space, a similar relationship is expected because recrystallization repels Sr and exhibits little isotope fractionation when equilibrating with seawater (Böhm et al., 2012; Stevenson et al., 2014; AlKhatib and Eisenhauer, 2017). We find no correlation between $\delta^{88/86}\text{Sr}$ and [Sr] in the cap dolostone, but a weak positive correlation in the limestone where the presumably most primary samples with highest [Sr] exhibit the highest $\delta^{88/86}\text{Sr}$ values (Figure AIII-4). These observations cannot be entirely explained by early diagenetic processes.

4.5 A meltwater – seawater mixing origin of cap carbonate

As observed in previous Maieberg Formation studies, geochemical differences exist between the two sections examined in this study (e.g., Kasemann et al., 2005; Hoffman et al., 2007; Kasemann et al., 2014). Integrated $\delta^{88/86}\text{Sr}$ and $\delta^{44/40}\text{Ca}$ measurements can help resolve the origin of geochemical variations because the two proxies covary during carbonate formation, but covariation is degraded as a consequence of diagenesis (Wang et al., 2019; Wang et al., 2021). On

the cross-plot of $\delta^{88/86}\text{Sr}$ and $\delta^{44/40}\text{Ca}$ (Figure 4-3), both sections of the cap dolostone exhibit good correlation. The Arbeitsgenot section shows a positive correlation with a slope of 0.21 ± 0.05 , which is very close to the slope expected in calcite precipitation experiments with rate-dependent Ca and Sr isotope fractionation (Böhm et al., 2012). This kinetic slope is less likely simulated by early diagenesis because the effect of early diagenetic alteration on bulk carbonate $\delta^{88/86}\text{Sr}$ is negligible (Voigt et al., 2015; Wang et al., 2021). A similar kinetic slope is also observed in biogenic calcites whose growth rate responded to seawater chemistry perturbations during the Early Cretaceous OAE 1a (Wang et al., 2021).

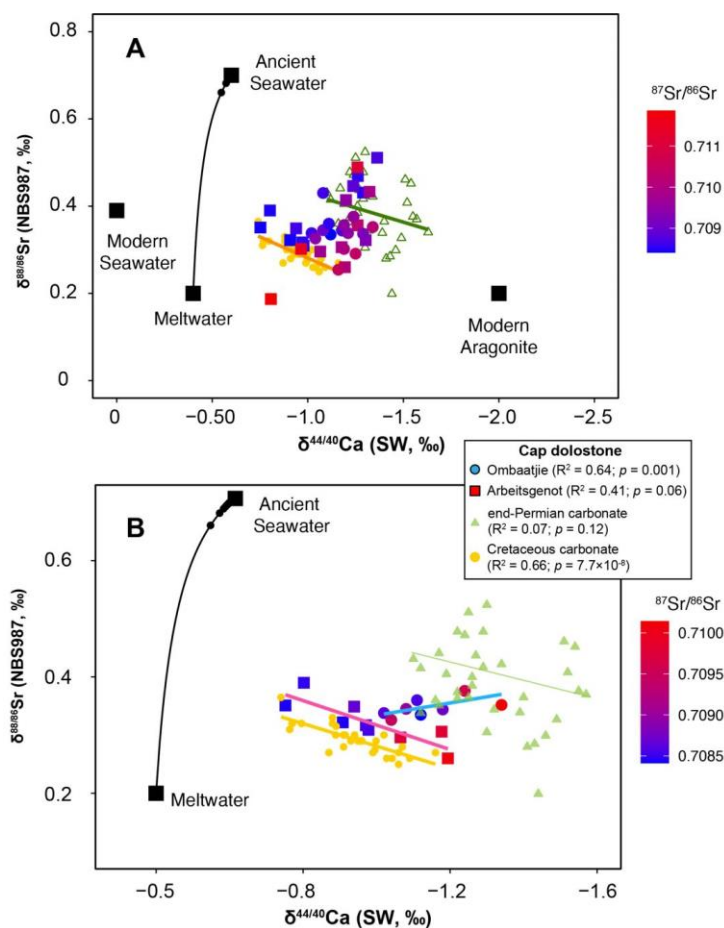


Figure 4-3 Cross-plots of $\delta^{44/40}\text{Ca}$ and $\delta^{88/86}\text{Sr}$ overlain with $^{87}\text{Sr}/^{86}\text{Sr}$ ratios. A) Samples of whole cap carbonate sequence; B) Samples of the Keilberg Member. Yellow circles represent data from the early Cretaceous oceanic anoxic event 1a (Wang et al., 2021); green triangles represent data

from the Permian-Triassic boundary (Wang et al., 2019). Solid line represents meltwater-seawater mixing line (see section 4.5 for details).

Numerous studies have suggested that the cap dolostone was deposited during the initial stage of the Marinoan deglaciation, whose prominent feature was high volume of meltwater runoff (e.g., Shields, 2005; Yang et al., 2017). When meltwater mixes with seawater, the chemical and isotopic compositions of mixtures can be derived by the following equations:

$$Ca_{\text{mix}} = Ca_r \chi + Ca_s (1 - \chi) \quad (4-1)$$

$$Sr_{\text{mix}} = Sr_r \chi + Sr_s (1 - \chi) \quad (4-2)$$

$$\delta^{44/40} Ca_{\text{mix}} = \delta^{44/40} Ca_r \left(\frac{Ca_r}{Ca_{\text{mix}}} \right) \chi + \delta^{44/40} Ca_s \left(\frac{Ca_s}{Ca_{\text{mix}}} \right) (1 - \chi) \quad (4-3)$$

$$\delta^{88/86} Sr_{\text{mix}} = \delta^{88/86} Sr_r \left(\frac{Sr_r}{Sr_{\text{mix}}} \right) \chi + \delta^{88/86} Sr_s \left(\frac{Sr_s}{Sr_{\text{mix}}} \right) (1 - \chi) \quad (4-4)$$

where χ is the proportion of meltwater runoff in the mixture, and Ca_r , Sr_r , $\delta^{44/40} Ca_r$, $\delta^{88/86} Sr_r$, Ca_s , Sr_s , $\delta^{44/40} Ca_s$, $\delta^{88/86} Sr_s$, Ca_{mix} , Sr_{mix} , $\delta^{44/40} Ca_{\text{mix}}$, and $\delta^{88/86} Sr_{\text{mix}}$ are calcium, strontium concentrations and $\delta^{44/40} Ca$, $\delta^{88/86} Sr$ values of riverine, seawater, and their mixture, respectively. In Figure 4-3, the meltwater-seawater mixing line was determined by estimates of glacial meltwater and end-Neoproterozoic seawater geochemistry (e.g., Peucker-Ehrenbrink and Fiske, 2019; Ahm et al., 2019; see Appendix III for details). When carbonate precipitates, the Ca and Sr isotopes fractionate from the mixing line (to the bottom right in Figure 4-3). To preserve the kinetic slope, the rate of carbonate precipitation must be faster than the rate of fluid evolving. Within this context, we suggest that the observed $\delta^{44/40} Ca$ and $\delta^{88/86} Sr$ shifts in the Arbeitsgenot cap dolostone represent faster precipitation rates from a reservoir with relatively uniform Ca and Sr isotope compositions. The highly fractionated dolostone samples corresponding to higher $^{87}Sr/^{86}Sr$ ratios

indicate that their higher precipitation rates may have resulted from continental meltwater runoff. This finding is consistent with the hypothesis that meltwater, carrying weathering-derived alkalinity, facilitated the rapid deposition of cap dolostone at the onset of deglaciation (e.g., Higgins and Schrag, 2003; Fabre and Berger, 2012; Kasemann et al., 2014; Yang et al., 2017; Hoffman et al., 2017). Despite the fact that the $\delta^{44/40}\text{Ca}$ and $\delta^{88/86}\text{Sr}$ values of freshwater melt are hard to constrain, they may have been lowered by intense weathering (e.g., Kasemann et al., 2014; Liu et al., 2014; Wei et al., 2019). The abrupt $^{87}\text{Sr}/^{86}\text{Sr}$ changes in the cap carbonate sequence also suggest a local signal rather than one reflecting the global ocean given the long residence time of Sr (Kaufman et al., 1993; Halverson et al., 2007, 2010). The $\delta^{88/86}\text{Sr}$ and $\delta^{44/40}\text{Ca}$ values in the proximal Ombaatjie cap dolostone show weak inverse correlation whereas the distal Arbeitsgenot samples do not, which indicates strong spatial heterogeneity across the Otavi platform. Yet, the similar $^{87}\text{Sr}/^{86}\text{Sr}$ pattern agrees with the inference that high continental weathering influx occurred at this time and the different $\delta^{88/86}\text{Sr}$ - $\delta^{44/40}\text{Ca}$ relationship could be reconciled by proximity to shore, where the effects of meltwater-seawater mixing would be more pronounced.

These results suggest that the Keilberg cap dolostone records primary signals reflecting rapid deposition in a freshwater-dominated environment, which agrees with the lithological observations and numerical simulations (e.g., Hoffman et al., 2011; Hoffman et al., 2017; Yang et al., 2017). For both sections, the overlying limestones exhibit more scatter, with no correlation between $\delta^{88/86}\text{Sr}$ and $\delta^{44/40}\text{Ca}$, which is similar to a dataset obtained from the Permian-Triassic boundary interval (Wang et al., 2019). This suggests that $\delta^{88/86}\text{Sr}$ and $\delta^{44/40}\text{Ca}$ of the reservoir may have oscillated during the time when these limestones were deposited.

In accordance with theoretical models (Allen and Hoffman, 2005; Shields, 2005; Yang et al., 2017), massive meltwater influx prevailed in the aftermath of the Marinoan snowball earth,

possibly formed a widespread plume (given the proposed large spatial heterogeneity in ocean geochemistry), and this likely facilitated the deposition of cap dolostone. During deposition of overlying strata, the stratified ocean may have been overturned (e.g., Hoffman et al., 2011; Yang et al., 2017; Irie et al., 2019), but the influence of meltwater on ocean geochemistry may have persisted, depending on the depositional environment. Overall, our theoretical model does not preclude the possibility of early diagenetic processes altering the geochemical signatures. However, it demonstrates that it is not necessary to incorporate them to explain the observed geochemical variability.

We compiled all published $\delta^{44/40}\text{Ca}$ records of cap dolostone from the Otavi platform and foreslope in Namibia (Figure 4-4) following the principle of $\delta^{13}\text{C}$ chemostratigraphy described by Hoffman et al. (2007, see Appendix III for details). The heterogeneous nature of cap dolostone geochemistry is observed among different depositional settings. The distinct pattern between platform and foreslope environment can be explained by varying degrees of freshwater mixing in different environments, where the epi-platform was dominated by freshwater and the foreslope exhibits a mixed signal between freshwater and saline seawater. Thus, the widely recognizable $\delta^{44/40}\text{Ca}$ excursion within the cap dolostone (e.g., Silva-Tamayo et al., 2010; Liu et al., 2013, 2014; Kasemann et al., 2014; Ahm et al., 2019; Wei et al., 2019) may reflect a global process variably influenced by local differences in rates of carbonate precipitation and magnitude of meltwater input. Parallel shifts in $\delta^{13}\text{C}$ and $\delta^{44/40}\text{Ca}$ values implies that the negative $\delta^{13}\text{C}$ excursion may have also been associated with rapid precipitation of carbonate, which provides supporting evidence for the kinetic isotope effect proposed by Higgins and Schrag (2003). Additionally, $\delta^{88/86}\text{Sr}$ values of the Maieberg carbonate (average 0.35‰) are significantly higher than the Phanerozoic carbonate average (0.16‰), suggesting a higher $\delta^{88/86}\text{Sr}$ value for end-Neoproterozoic seawater (Sawaki et

al., 2010). This may imply that the end Neoproterozoic ocean was characterized by higher carbonate burial rates (e.g., Strauss and Tosca, 2020) led by high atmospheric $p\text{CO}_2$ (e.g., Bao et al., 2008) and elevated silicate weathering at this time (e.g., Halverson et al., 2007; Huang et al., 2016). Such a high precipitation rate of carbonate would eventually sequester atmospheric CO_2 accumulated during the glaciation and help to stabilize Neoproterozoic climate (Berner and Calderia, 1997; Pierrehumbert et al., 2011; Strauss and Tosca, 2020).

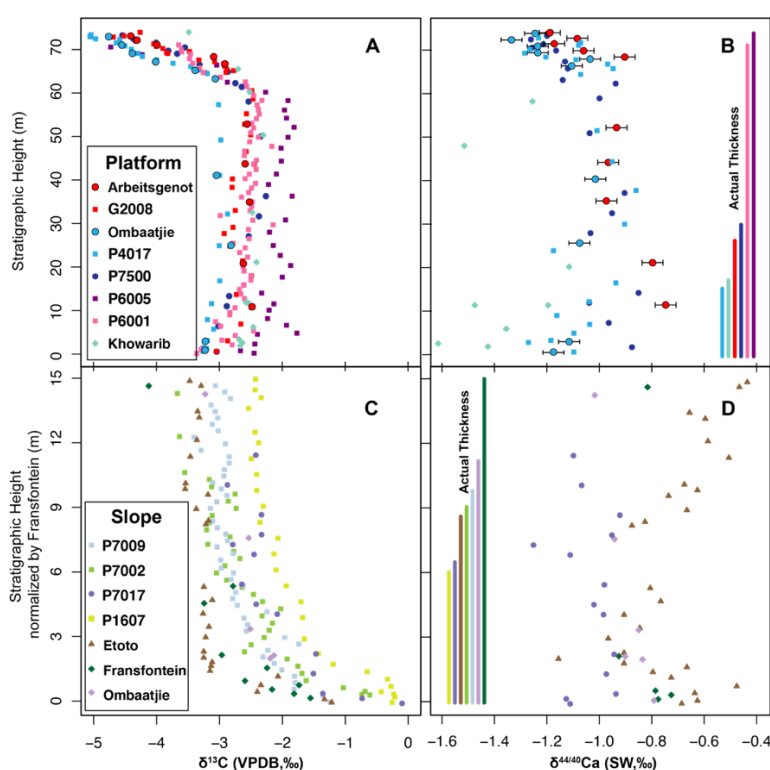


Figure 4-4 Compilation of $\delta^{13}\text{C}$ and $\delta^{44/40}\text{Ca}$ records from sections across the Otavi platform (A and B) and its foreslope (C and D). Stratigraphic correlations are utilized $\delta^{13}\text{C}$ following Hoffman et al. (2017).

4.7 Conclusions

Our study provides a new perspective on the origin of Maronian cap carbonate. The $\delta^{44/40}\text{Ca}$ and $\delta^{88/86}\text{Sr}$ correlation with a kinetic slope in the Arbeitsgenot section provides a piece of compelling evidence for the primary origin of the Namibian cap dolostones. To preserve such a

kinetic slope, the cap dolostone must have been deposited in a rate faster than the rate of meltwater-seawater mixing, which is less than 10^5 years based on numerical stimulations (Yang et al., 2017). Our findings agree with the recent geochronological data of Marinoan cap dolostones in South China (Condon et al., 2005; Zhou et al., 2019). Thus, the $\delta^{44/40}\text{Ca}$ and $\delta^{88/86}\text{Sr}$ negative shifts within the Keilberg cap carbonate can be readily explained by the kinetic effect from fast precipitation. $\delta^{44/40}\text{Ca}$ and $\delta^{88/86}\text{Sr}$ variations in the overlying limestone can be attributed to changes in the geochemistry of precipitating fluids due to meltwater-seawater mixing. More generally, our findings describe a global deglaciation process amplified by local depositional environments, where intensified riverine runoff with enhanced continental weathering and alkalinity input to shelf environment and mixing between meltwater and seawater. Our data also implies that the Marinoan negative $\delta^{13}\text{C}$ excursion may reflect a component of kinetic isotope effect and water mass mixing. Overall, this meltwater-seawater mixing process provides a simple answer to the observed $\delta^{44/40}\text{Ca}$ and $\delta^{88/86}\text{Sr}$ variations as well as the long-recognized geochemical heterogeneity in Neoproterozoic cap carbonates (e.g., Hoffman et al., 2011; Kasemann et al., 2005; Kasemann et al., 2014; Liu et al., 2014; Liu et al., 2018; Ahm et al., 2019).

CHAPTER 5

CONCLUSIONS

Carbon dioxide (CO₂) is one of the most important forcing factors influencing the Earth System. The current anthropogenically forced rise in atmospheric CO₂ is predicted to cause climate warming, and, consequently, increases in wildfire, drought, extreme weather, and global sea-level. Ocean acidification is also a predicted consequence of elevated atmospheric CO₂ (Doney et al., 2019). As a result of the observed atmospheric CO₂ increase, average surface ocean pH has fallen by ~0.1 units since preindustrial times (NOAA, 2020). Given that pH is a logarithmic scale, this represents a doubling of the acidity levels in seawater. Correspondingly, the saturation states for carbonate minerals have decreased dramatically, which has caused a series of biological catastrophes (see reviews in Doney et al., 2019). To better understand how the Earth System responds to rising atmospheric CO₂, this dissertation investigated three geological events associated with abrupt CO₂ changes: the end-Permian mass extinction (associated with the eruption of Siberian Traps large igneous province and the largest mass extinction in Earth history: Chapter 2), the Early Cretaceous Oceanic Anoxic Event 1a (correlative with eruption of the Ontong Java large igneous province and a crisis among calcareous plankton: Chapter 3), and the Neoproterozoic Marinoan deglaciation (related to long-term build-up of volcanic CO₂ during a Snowball Earth event: Chapter 4).

Stable Ca and Sr isotopes have provided a powerful tool for understanding the Earth system processes that control the global carbon cycle. The research in Chapter 2 presented the $\delta^{44/40}\text{Ca}$, $^{87}\text{Sr}/^{86}\text{Sr}$, and $\delta^{88/86}\text{Sr}$ records across the Permian-Triassic boundary, a time period characterized by severe biological and environment perturbations. Our study demonstrated that the enhanced

weathering of shelf carbonate during sea level fall and its induced lowering of stable Ca and Sr isotopic compositions in riverine flux can significantly decrease seawater $\delta^{44/40}\text{Ca}$ and $\delta^{88/86}\text{Sr}$ without affecting $^{87}\text{Sr}/^{86}\text{Sr}$ ratios. Moreover, this study reconciled a variety of geochemical measurements and conceptual models and set a valuable workflow for validating the fidelity of bulk sediment $\delta^{44/40}\text{Ca}$ and $\delta^{88/86}\text{Sr}$ signatures.

Stable Sr isotopes is particularly useful in distinguishing primary versus diagenetic processes and resolving the origin of $\delta^{44/40}\text{Ca}$ signals. This is because $\delta^{88/86}\text{Sr}$ of carbonate is less susceptible to diagenetic overprinting due to minimal uptake from surrounding fluids during recrystallization (Baker et al., 1982; Richter and DePaolo, 1998; Voigt et al., 2015). In Chapter 2, I applied these concepts to shallow-water carbonates that formed in the mid-Pacific of the early Cretaceous. Our measurements revealed a strong correlation between $\delta^{44/40}\text{Ca}$ and $\delta^{88/86}\text{Sr}$. The slope of the line is consistent with kinetic control of the Ca and Sr isotope fractionation factors (Böhm et al., 2012). This observation precludes major effects from diagenetic alteration and further reveals that these shallow-water carbonates archived primary geochemical signals. Positive $\delta^{44/40}\text{Ca}$ and $\delta^{88/86}\text{Sr}$ shifts that begin before OAE 1a and peak within the interval are consistent with reduced precipitation rates (Erba et al., 2011) and reconstructed pCO_2 maxima (Naafs et al., 2016). Our results suggest that the $\delta^{44/40}\text{Ca}$ and $\delta^{88/86}\text{Sr}$ variability across OAE1a can be attributed to rate-dependent Ca and Sr isotope fractionation variation, which derive from the dynamic interplay between LIP eruptions and biocalcification feedbacks. Additionally, this study provided strong evidence of kinetic isotope effects in naturally-occurring biogenic carbonates and updated the interpretive framework of $\delta^{44/40}\text{Ca}$ and $\delta^{88/86}\text{Sr}$ records for the Early Aptian.

In Chapter 4, the same $\delta^{44/40}\text{Ca}$ - $^{87}\text{Sr}/^{86}\text{Sr}$ - $\delta^{88/86}\text{Sr}$ multi-proxy tool was used to study cap carbonate formation during the Marinoan deglaciation. Two measured sections along a proximal-

distal transect showed negative excursions in $\delta^{44/40}\text{Ca}$ and $\delta^{88/86}\text{Sr}$ and positive shifts in $^{87}\text{Sr}/^{86}\text{Sr}$ ratios within the cap dolostone. The Arbeitsgenot section exhibiting the kinetic slope as observed in the samples of Cretaceous OAE 1a provided compelling support for the primary origin of the rock, and also suggested that the cap dolostone must have been precipitated at a rate that was faster than meltwater-seawater mixing. The $\delta^{44/40}\text{Ca}$ and $\delta^{88/86}\text{Sr}$ patterns in the overlying carbonate could be explained by the process of meltwater-seawater mixing. Overall, our data support that the cap dolostone was rapidly deposited in a meltwater dominated environment and the overlying strata was likely deposited in a seawater-meltwater mixing environment in agreement with field observations (e.g., Allen and Hoffman, 2005) and numerical modeling simulations (e.g., Yang et al., 2017). Additionally, our study also implied that the globally recognizable negative $\delta^{13}\text{C}$ excursion within the cap dolostone may have also been associated with rapid precipitation of carbonate with the kinetic isotope effect proposed by Higgins and Schrag (2003).

Regardless of event duration and sample archive, similar positive shifts that slightly precede shifts in $\delta^{13}\text{C}$ records are observed when comparing the $\delta^{44/40}\text{Ca}$ data among several candidate ocean acidification events in deep time (e.g., the Paleocene–Eocene Thermal Maximum, Kitch et al., 2021; the end-Cretaceous mass extinction, Linzmeier et al., 2020; the Cretaceous OAE 1a, Wang et al., 2021; the Cretaceous OAE 2, Du Vivier et al., 2015). This suggests that seawater carbonate chemistry across ocean acidification events must be controlled by fundamental interactions between marine organisms and their environment. Integration of $\delta^{44/40}\text{Ca}$, $^{87}\text{Sr}/^{86}\text{Sr}$, and $\delta^{88/86}\text{Sr}$ proxies provide a powerful tool to investigate the global carbon cycle and seawater carbonate chemistry changes during times of rapid CO_2 release.

APPENDIX I

Results of the end-Permian rock samples and the leaching experiments

Table AI-1 Elemental, C, O, Ca, and Sr isotope geochemistry of rock samples from the Dajiang and Meishan sections

Sample	Elevation	$\delta^{13}\text{C}$	$\delta^{13}\text{C}$ Duplicate	$\delta^{18}\text{O}$	$\delta^{18}\text{O}$ Duplicate	Ca	Mg
		(‰)	(‰)	(‰)	(‰)	($\mu\text{mol/g}$)	($\mu\text{mol/g}$)
Dajiang	(m)						
DJ1	6.4	2.7		-4.0		7894	112
DJ2	9.6	2.9		-4.1		-	-
DJ3	10.5	2.5		-4.3		-	-
DJ4	11.0	2.3		-6.4		-	-
DJ5	11.6	3.0		-5.4		-	-
DJ6	12.2	2.7		-4.5		7976	110
DJ7	12.8	2.2		-4.2		-	-
DJ8	13.7	2.4		-4.7		-	-
DJ9	14.5	2.1		-5.7		-	-
DJ10	15.0	2.6		-4.9		8113	157
DJ11	16.0	2.4		-3.4		-	-
DJ12	16.5	2.2		-6.0		-	-
DJ13	17.1	2.0	2.2	-6.9	-6.4	6849	64
DJ14	18.1	-		-		7685	327
DJ15	18.8	2.1		-5.9		-	-
DJ16	19.5	2.1	2.1	-6.1	-6.2	-	-
DJ17	19.5	2.2		-7.4		6519	143
DJ18	21.2	3.0		-1.1		7903	242

DJ19	22.6	1.5		-3.2		8117	249
DJ20	24.0	2.5	1.5	-1.7	-3.4	7696	415
DJ21	24.1	1.4	1.5	-3.9	-4.0	7187	442
DJ22	25.4	0.7		-3.4		6703	198
DJ23	25.6	0.9		-3.4		6833	1273
DJ24	26.2	0.5		-3.9		7554	951
DJ25	26.3	0.7	1.5	-3.0	-4.8	-	-
DJ26	26.9	-0.1		-3.9		5820	285
DJ27	27.1	-0.1		-5.3		-	-
DJ28	27.1	0.2		-5.4		-	-
DJ29	27.3	0.0		-4.2		6725	1491
DJ30	27.4	0.7		-3.1		7440	1464
DJ31	28.1	0.3		-5.1		6952	303
DJ32	28.7	-0.1	0.0	-4.4	-4.2	9746	454
DJ33	29.2	-0.4	-0.4	-4.0	-4.0	-	-
DJ34	29.5	0.2		-4.8		9955	233
DJ35	30.2	0.0		-4.6		11172	382
DJ36	31.1	-0.2		-4.6		10871	334
DJ37	32.0	1.7	1.4	-1.1	-1.0	13459	473
DJ38	33.0	0.0		-4.3		12798	445
DJ39	34.8	0.1		-4.0		12376	769
DJ40	34.9	0.3		-3.8		12372	761
DJ41	35.6	0.6		-4.6		12562	793
DJ42	35.7	0.5		-3.6		12287	1051
DJ43	37.2	1.3		-4.9		8894	219
DJ44	37.5	1.3		-5.1		-	-
DJ45	38.0	1.5		-4.2		12056	315

DJ46	38.5	-	-	-	-	8312	148
DJ47	39.8	2.0	1.7	-5.8	-5.7	9739	314
DJ48	40.7	1.9		-4.4		-	-
DJ49	42.1	1.8	1.8	-6.0	-4.6	7559	388
DJ50	43.1	2.1		-5.4		-	-
DJ51	43.6	2.2		-5.2		-	-
DJ52	45.0	2.0		-4.7		8707	176
DJ53	46.4	2.0	2.1	-4.7	-4.7	8430	167
DJ54	47.8	2.2	2.4	-4.4	-4.5	8376	162
DJ55	50.0	1.9	2.0	-4.5	-4.7	7721	153
DJ56	52.3	2.1	2.2	-4.6	-4.4	8102	308
DJ57	56.4	2.1	2.1	-4.8	-4.0	8465	302
DJ58	58.6	2.0		-4.4		8255	191
DJ59	60.4	2.0	2.1	-3.1	-2.9	8741	137
DJ60	62.6	2.1	2.2	-3.6	-3.3	9255	131
DJ61	64.6	2.1	2.5	-3.7	-3.4	8331	126
DJ62	66.4	2.1	2.3	-4.2	-4.2	8522	164
DJ63	69.0	2.1	2.3	-2.9	-2.7	8222	265
DJ64	70.4	2.2	2.4	-3.1	-2.8	8189	973
DJ65	72.8	2.2	2.5	-3.8	-3.4	8125	164
DJ66	75.1	2.2		-2.7		9903	444
DJ67	78.0	2.2	2.3	-3.9	-3.8	8428	3
<hr/>							
Meishan	(cm)						
MS24e-1	0.2	2.0	1.9	-4.4	-4.4	5389	157
MS24e-2	1.3	2.1	2.1	-4.1	-3.8	9270	200
MS24e-3	2.2	1.9	2.2	-3.2	-4.4	7998	242
MS24e-4	3.3	1.9		-3.2		6710	238

MS24e-5	4.2	2.1	1.9	-4.6	-3.3	6954	232
MS24e-6	5.2	2.1		-4.8		7792	225
MS24e-7	6.2	1.9	1.9	-4.8	-3.4	6894	186
MS24e-8	7.1	1.7	1.7	-5.8	-4.8	6407	155
MS24e-9	7.6	1.6		-3.2		5307	122
MS24e-10	8.7	0.5		-8.2		4853	115
MS24e-11	9.6	0.7		-7.5		3441	80
MS24e-12	10.6	0.9		-6.9		2097	55
MS26-1	13.8	-0.7		-9.2		771	68
MS26-2	15.3	-0.5		-8.5		640	51
MS26-3	16.3	-0.1		-8.0		948	62
MS26-4	17.3	-0.3		-7.9		752	59
MS26-5	18.3	-0.8		-8.3		519	55
MS26-6	19.6	-0.3		-8.3		678	62
MS26-7	20.8	0.0		-7.6		634	37
MS26-8	21.3	0.6		-7.1		1496	122
MS27-1	21.5	1.4		-4.5		2276	496
MS27-2	22.5	1.4		-4.0		3351	599
MS27-3	23.4	0.9	0.7	-5.4	-5.4	2665	606
MS27-4	24.4	0.6		-7.4		3751	547
MS27-5	25.4	0.2		-7.8		4405	291
MS27-6	26.6	-0.1		-8.6		3494	83
MS27-7	27.7	1.5	1.7	-4.1	-3.3	3110	1407
MS27-8	28.7	0.9		-5.4		3744	524
MS27-9	29.7	1.4	1.4	-4.3	-4.1	2989	1321
MS27-10	30.7	1.1	1.1	-4.6	-4.3	3767	766
MS27-11	31.7	1.4	1.6	-4.2	-3.4	3014	1227

MS27-12	32.8	1.5	1.7	-3.9	-3.3	2613	1230
MS27-13	33.8	1.4		-3.6		2958	1540
MS27-14	34.8	0.7		-5.3		5429	1336
MS27-15	35.8	0.8		-6.3		3926	1109
MS27-16	37	0.8		-5.5		2406	721
MS29-3-0.2	37.2	1.0		-5.1		7061	2747
M29-3-1.1	38.1	1.2	1.1	-4.0	-3.7	6781	3021
MS29-3-2.3	39.3	1.1		-3.8		4459	3112
MS29-3-3.1	40.1	1.2	1.1	-3.3	-3.7	4587	3050
MS29-3-4.2	41.2	0.8		-4.4		6228	3264
MS29-1/2-0.3	41.5	1.1		-3.6		6975	3208
MS29-1/2-1.2	42.4	1.1		-3.8		7443	3128
MS29-1/2-2.2	43.4	1.2		-4.1		3405	1685
MS29-1/2-3.2	44.4	1.1		-3.5		5053	3231
MS29-1/2-4.2	45.4	1.1		-3.6		5441	3141
MS29-1/2-5.3	46.5	1.0		-4.0		4874	3087
MS29-1/2-6	47.2	1.1		-3.8		4569	2848
MS29-1/2-7.2	48.4	1.1		-3.7		4570	2848

Table AI-1 (continued)

Mn	Sr	CaC O ₃	$\delta^{44/40}\text{Ca}$	$\delta^{44/40}\text{Ca}$ Duplicate	$^{87}\text{Sr}/^{86}\text{Sr}$	$^{87}\text{Sr}/^{86}\text{Sr}$ Duplicate	$\delta^{88/86}\text{S}$ r	$\delta^{88/86}\text{Sr}$ Duplicate
(nmol/g)	(nmol/g)	(%)	(‰)	(‰)			(‰)	(‰)
1238	9039	79	-1.16	-1.14	0.70727	0.70726	0.36	
-	-	-	-		-		-	
-	-	-	-		-		-	

-	-	-	-	-	-	-	-
-	-	-	-	-	-	-	-
3786	10911	80	-1.19	-1.16	-	-	-
-	-	-	-	-	-	-	-
-	-	-	-	-	-	-	-
-	-	-	-	-	-	-	-
6808	7738	81	-1.17		0.70724	0.35	
-	-	-	-	-	-	-	-
-	-	-	-	-	-	-	-
1565	7008	68	-		0.70726	-	
7645	8719	77	-1.30		0.70715	0.70715	0.30 0.30
-	-	-	-	-	-	-	-
-	-	-	-	-	-	-	-
728	8263	65	-		-	-	
8373	9039	79	-1.48		0.70722	0.70722	0.32 0.32
9320	9176	81	-1.41		0.70727	0.28	
12341	9153	77	-		-	-	
11904	8834	72	-1.43	-1.43	-	-	
7245	9815	67	-1.44		0.70721	0.20	0.20
9902	8103	68	-		-	-	
10448	10043	75	-		-	-	
-	-	-	-1.46		0.70719	0.30	
10921	8628	58	-		-	-	
-	-	-	-	-	-	-	-
-	-	-	-	-	-	-	-
12450	8856	67	-1.39		0.70720	0.34	
12305	8560	77	-		-	-	

11941	8423	84	-1.63	-1.61	0.70721		0.34	
13834	10066	97	-		-		-	
-	-	-	-1.59		0.70721		-	
9101	12349	99	-		-		-	
10921	9130	100	-1.62		0.70723		-	
18312	12029	100	-		-		-	
10303	11550	100	-1.57		0.70723		0.37	0.36
15618	11915	100	-1.56		0.70725		0.37	
12123	9655	100	-		-		-	
10367	8761	100	-1.43		0.70731		-	
8013	7632	100	-1.49		0.70726		0.33	0.31
7281	6962	100	-		-		-	
983	7601	89	-1.51		0.70725		-	
-	-	-	-		-		-	
6116	11322	100	-1.43		0.70727		0.32	
6189	11984	83	-1.45		0.70730		-	
4733	13056	97	-1.47		-		-	
-	-	-	-		-		-	
8664	9085	76	-1.43	-1.41	-		-	
-	-	-	-		-		-	
-	-	-	-		-		-	
4296	11664	87	-1.54		0.70723	0.70724	0.45	0.47
2476	11299	84	-1.51	-1.52	-		-	
1274	11093	84	-1.52		-		-	
692	11915	77	-1.52	-1.52	0.70725	0.70725	0.41	
3604	11230	81	-1.56		-		-	
692	13924	85	-1.55	-1.55	0.70727		0.38	

1966	13718	83	-1.50		-		-	
3604	9313	87	-1.43		-		-	
3568	10180	92	-1.51	-1.55	0.70729		0.46	
692	6871	83	-1.45		-		-	
655	16366	85	-1.50		-		-	
291	4793	82	-1.35		-		-	
-	3698	82	-1.39		0.70740		0.48	
-	3652	81	-1.41		-		-	
655	3401	99	-		0.70749		0.44	0.45
437	2899	84	-1.42		-		-	
<hr/>								
6152	4622	54	-1.29	-1.3	-		-	
7336	4987	93	-1.34		-		-	
4678	9028	80	-1.24		0.70712		0.47	
4441	5535	67	-1.32	-1.27	0.70715		-	
4441	5273	69	-1.22	-1.21	0.70713	0.70712	0.48	
5151	4987	78	-1.31		-		-	
6425	4634	69	-1.23	-1.26	-		-	
10284	4006	64	-1.32		-		-	
9356	4063	53	-1.30		0.70740		0.52	
11158	4360	48	-1.29		0.70749		-	
7117	2602	34	-1.25	-1.23	0.70751		0.51	
5315	1267	21	-1.29		0.70753		0.48	0.48
1929	993	8	-1.22	-1.25	0.71070	0.71070	0.37	
1547	890	6	-1.28		-		-	
2239	1096	9	-1.22		0.70981	0.70979	0.36	0.36
1693	936	8	-1.28		-		-	

1329	776	5	-1.25	-1.27	0.70970		0.37	
1347	913	7	-1.25		-		-	
1129	833	6	-1.40	-1.37	0.70983	0.70982	0.37	
4023	1290	15	-1.41		0.70796		-	
6189	1780	23	-1.26		0.70837		0.39	
7117	2214	33	-1.24		-		-	
9174	2602	27	-1.27		0.70783	0.70783	-	
9265	3595	37	-1.19		0.70773		0.41	
11977	3972	44	-1.12	-1.06	0.70777		0.34	
10594	3104	35	-1.10	-1.16	0.70759		0.43	
8064	2716	31	-1.27		0.70765		0.44	
7044	3333	37	-1.18		-		-	
9465	2477	30	-1.29	-1.3	0.70770		0.42	
9301	2887	38	-1.15	-1.17	0.70776		-	
8865	2397	30	-1.12		0.70787		0.42	0.43
9028	2203	26	-1.26		0.70794		-	
8701	2477	30	-1.26		0.70775		0.40	0.39
7882	3812	54	-1.16		-		-	
8883	2728	39	-1.17		0.70790		0.44	
13907	3276	24	-1.31	-1.35	-		-	
10594	4668	71	-1.33		0.70784		-	
8155	3629	79	-1.29		-		-	
8737	3652	45	-1.34	-1.35	0.70789	0.70789	0.42	0.40
9083	3549	46	-1.28		0.70788		-	
9957	4006	62	-1.32	-1.35	0.70766		0.34	0.33
10994	4063	70	-1.28	-1.31	-		-	
14271	3698	74	-1.36		-		-	

14744	4006	34	-1.28	-	-
17274	4451	50	-1.29	0.70785	-
15727	3355	52	-1.30	-	-
16091	3378	51	-1.29	-	-
17511	3492	46	-1.29	-	-
17292	3401	46	-1.36	-	-

Table A1-2 Ca and Sr isotope geochemistry of leachates from sequential leaching experiment

Sample	Leaching Step	Elevation (cm)	Ca %	$\delta^{44/40}\text{Ca}$ (‰)	$\delta^{44/40}\text{Ca}$ Weighted Average (‰)
MS26-1	1N NH ₄ Ac		47%	-1.21	
	0.25% HAc	13.8	27%	-1.21	-1.21
	1% Hac		10%	-	
	5% Hac		7%	-	
MS26-3	1N NH ₄ Ac		51%	-1.25	
	0.25% Hac	16.3	30%	-1.20	-1.23
	1% Hac		10%	-1.22	
	5% Hac		1%	-1.19	
MS26-5	1N NH ₄ Ac		47%	-1.25	
	0.25% Hac	18.3	26%	-1.32	-1.27
	1% Hac		14%	-1.25	

	5% Hac		7%	-1.28	
	1N NH ₄ Ac		47%	-1.28	
MS26-7	0.25% Hac	20.8	31%	-1.38	-1.34
	1% Hac		13%	-1.40	
	5% Hac		11%	-1.37	

Table A1-2 (Continued)

Sr	⁸⁷ Sr/ ⁸⁶ Sr	⁸⁷ Sr/ ⁸⁶ Sr Weighted Average	$\delta^{88/86}\text{Sr}$ (‰)	$\delta^{88/86}\text{Sr}$ Weighted Average (‰)
32%	0.71105		0.38	
44%	0.71156	0.71121	0.31	0.34
15%	0.71123		0.35	
4%	0.70860		0.37	
35%	0.70808		0.37	
59%	0.70959	0.70906	0.33	0.34
14%	0.70926		-	
0%	-		-	
26%	0.70916		0.29	
52%	0.70970	0.70947	0.35	0.33
14%	0.70953		0.35	
5%	0.70856		-	
25%	0.70869		0.35	
47%	0.70981	0.70942	0.36	0.36
19%	0.70962		0.36	
4%	0.70842		0.34	

Table A1-2 (Continued)

Sample	Leaching Step	Elevation (m)	Ca %	$\delta^{44/40}\text{Ca}$ (‰)	$\delta^{44/40}\text{Ca}$ Weighted Average (‰)
DJ19	1N NH ₄ Ac		32%	-1.30	
	0.25% HAc	22.6	55%	-1.45	-1.42
	1% HAc		13%	-1.48	
	5% HAc		0%	-	
DJ22	1N NH ₄ Ac		-	-	
	0.25% HAc	25.4	-	-	-
	1% HAc		-	-	
	5% HAc		-	-	
DJ25	1N NH ₄ Ac		33%	-1.41	
	0.25% HAc	26.3	48%	-1.57	-1.49
	1% HAc		14%	-1.41	
	5% HAc		1%	-	
DJ29	1N NH ₄ Ac		36%	-1.45	
	0.25% HAc	27.3	55%	-1.39	-1.41
	1% HAc		9%	-	
	5% HAc		1%	-	

	1N NH ₄ Ac		34%	-1.63	
DJ31	0.25% HAc	28.1	50%	-1.62	-1.62
	1% HAc		10%	-1.62	
	5% HAc		1%	-	

Table A1-2 (Continued)

Sr	⁸⁷ Sr/ ⁸⁶ Sr	⁸⁷ Sr/ ⁸⁶ Sr Weighted Average	$\delta^{88/86}\text{Sr}$ (‰)	$\delta^{88/86}\text{Sr}$ Weighted Average (‰)
18%	0.70729		0.27	
55%	0.70727	0.70725	0.28	0.28
27%	0.70720		-	
0%	-		-	
16%	0.70726		0.23	
50%	0.70722	0.70721	0.19	0.21
22%	0.70715		0.24	
4%	-		-	
15%	0.70720		0.30	
53%	0.70716	0.70718	0.29	0.29
25%	0.70722		0.29	
1%	0.70724		0.30	
9%	0.70726		0.29	
44%	0.70722	0.70721	0.31	0.31
39%	0.70721		0.31	
1%	0.70720		0.32	

20%	0.70724		0.36	
44%	0.70720		0.34	
		0.70721		0.34
27%	0.70724		0.35	
1%	-		-	

APPENDIX II

Lithology, methodology, data, and supporting information for samples of the Cretaceous OAE 1a

Lithology

Samples analyzed in this study are from Hole 866A drilled on the flanks of Resolution Guyot in the Mid-Pacific (21°N, 174°E). Cyclic packstone–wackestones and oolitic/peloidal grainstones dominate the lithology, with lesser amounts of dolomitic packstone (Sager et al., 1993; Jenkyns and Strasser, 1995). Skeletal fragments of rudists, gastropods, and corals occur as sand-sized or larger grains (Sliter, 1995; Swinburne et al., 1995). Petrologic and elemental analyses reveal calcite as the primary mineralogy (Jenkyns and Strasser, 1995), although parts of the core below the study interval (>1200 mbsf) show evidence for dolomitization (Flood and Chivas, 1995).

Thermal gradients have convected large volumes of seawater through the carbonates (Paull et al., 1995). This mechanism may have supplied Mg necessary for dolomitization lower in the section (Food and Chivas, 1995), but the results presented here for the overlying limestone do not reveal significant secondary incorporation of seawater Ca and Sr. Limestone at the base of Hole 865, drilled on Allison Guyot, shows evidence for radiogenic Sr isotope equilibration with basaltic basement rocks (Paull et al., 1995). However, the Hole 866 rocks analyzed here, as well as stratigraphically equivalent rocks at Hole 865, display $^{87}\text{Sr}/^{86}\text{Sr}$ ratios consistent with the global record, and no evidence exists for alteration by younger fluids (Paull et al., 1995). While researchers have raised concerns about meteoric water diagenesis at Hole 866A (Röhl and Strasser, 1995), other studies suggest minimal alteration, or at least negligible impact on bulk sediment $\delta^{13}\text{C}$ values and $^{87}\text{Sr}/^{86}\text{Sr}$ ratios (Jenkyns and Wilson, 1999).

Analytical Methods

We analyzed a subset of samples previously investigated by Mills et al. (2017). Rocks were powdered in a shatterbox equipped with an alumina ceramic grinding container. Approximately ~200 mg of powder was dissolved in 10 mL of ultrapure 5% HNO₃ in acid-cleaned centrifuge tubes for 12 hrs. The mixtures were centrifuged, and the supernatants were passed through 0.45 μm polypropylene syringe filters, collected in Teflon beakers, dried at 90 °C, and re-dissolved in 15 mL of 5% HNO₃ for elemental and isotopic analyses.

Subsamples of the solutions taken for elemental analysis were diluted to minimize matrix effects. Concentrations of Ca, K, Mg, Na, Mn, and Sr were measured using a Thermo Scientific iCAP 6500 ICP-OES. K was not detected in the samples. Repeated analyses of NIST-1643f yielded results within ±5% of reported concentrations. In addition, Ca and Sr concentrations measured by ICP-OES were within ±5% of those determined by isotope dilution, as part of the double-spike methodologies presented below. Calcium concentrations were used to estimate the abundance of calcium carbonate (wt%), assuming stoichiometric CaCO₃.

Carbon and oxygen isotope ratios were measured using a Gas Bench connected to a Delta V Plus Isotope Ratio Mass Spectrometer (IRMS). Powders were purged with He for 7 minutes and then reacted overnight at 30 °C with 103% anhydrous H₃PO₄. Results were calibrated against NBS-18, NBS-19, and one internal CaCO₃ standard. Data are reported in δ-notation (δ¹³C and δ¹⁸O) relative to Vienna Peedee Belemnite (VPDB). The uncertainties (2σ_{SD}) for δ¹³C and δ¹⁸O are ±0.12‰ and ±0.30‰, respectively.

Calcium and strontium isotope ratios were measured using a Thermo-Scientific Triton Thermal Ionization Mass Spectrometer (TIMS) equipped with $10^{11} \Omega$ amplifier resistors. Wang et al. (2019) recently reviewed the methods. In brief, a ^{43}Ca - ^{42}Ca double-spike technique was used to measure $^{44}\text{Ca}/^{40}\text{Ca}$ ratios (Lehn et al., 2013). Procedural blanks quantified with an ^{42}Ca isotope dilution method were negligible (~ 50 ng, $n = 6$) compared to the amount of sample Ca that was spiked and processed through column chemistry (50 μg). Radiogenic and stable Sr isotope ratios ($^{87}\text{Sr}/^{86}\text{Sr}$ and $^{88}\text{Sr}/^{86}\text{Sr}$) were measured following Andrews et al. (2016) and Andrews and Jacobson (2017). $^{87}\text{Sr}/^{86}\text{Sr}$ ratios were measured using multi-dynamic mode, and instrumental mass fractionation was corrected by normalizing $^{88}\text{Sr}/^{86}\text{Sr}$ ratios to a value of 8.3752 using an exponential law. An ^{87}Sr - ^{84}Sr double-spike technique was used to measure fractionated $^{88}\text{Sr}/^{86}\text{Sr}$ ratios. The $^{88}\text{Sr}/^{86}\text{Sr}$ data reduction includes input of corresponding $^{87}\text{Sr}/^{86}\text{Sr}$ ratios. Procedural blanks determined with an ^{84}Sr isotope dilution method were negligible (~ 70 pg, $n = 3$) compared to the amounts of Sr employed for both analyses (150 ng for $^{87}\text{Sr}/^{86}\text{Sr}$ and 200 ng for $^{88}\text{Sr}/^{86}\text{Sr}$). $^{44}\text{Ca}/^{40}\text{Ca}$ and $^{88}\text{Sr}/^{86}\text{Sr}$ ratios are reported in δ -notation, with $\delta^{44/40}\text{Ca}$ presented relative to the Ocean Scientific International Ltd. (OSIL) Atlantic seawater standard (SW) and $\delta^{88/86}\text{Sr}$ presented relative to NIST SRM-987 strontium carbonate standard (NIST-987).

For $\delta^{44/40}\text{Ca}$, at least 6 SW standards and 2 NIST-915b standards were analyzed every 30 samples. For $\delta^{88/86}\text{Sr}$, at least 6 NIST-987 standards and 2 IAPSO seawater standards were analyzed every 40 or fewer samples. During the period of study, repeated analyses yielded $\delta^{44/40}\text{Ca}_{\text{SW}} = 0.000 \pm 0.003\text{‰}$ ($2\sigma_{\text{SEM}}$, $n=16$) and $\delta^{44/40}\text{Ca}_{915b} = -1.134 \pm 0.002\text{‰}$ ($2\sigma_{\text{SEM}}$, $n=6$). These results point to a remarkably good short-term reproducibility ($2\sigma_{\text{SD}}$) ranging between 0.012‰ and 0.005‰. The current long-term values for the laboratory are $\delta^{44/40}\text{Ca}_{\text{SW}} = 0.000 \pm 0.002\text{‰}$ ($2\sigma_{\text{SEM}}$,

n=661) and $\delta^{44/40}\text{Ca}_{915b} = -1.135 \pm 0.003\text{‰}$ ($2\sigma_{\text{SEM}}$, n=263). These results are consistent with an external reproducibility ($2\sigma_{\text{SD}}$) of $\pm 0.05\text{‰}$, which is the uncertainty adopted for the study. As shown below, the reproducibility of sample unknowns is better than $\pm 0.05\text{‰}$. During the period of study, repeated measurements of NIST-987 yielded $^{87}\text{Sr}/^{86}\text{Sr} = 0.710250 \pm 0.000002$ ($2\sigma_{\text{SEM}}$, n=10), consistent with the long-term mean ratio for the laboratory of 0.710251 ± 0.000001 ($2\sigma_{\text{SEM}}$, n=211). The overall uncertainty ($2\sigma_{\text{SD}}$) assigned to $^{87}\text{Sr}/^{86}\text{Sr}$ ratios is ± 0.000010 . For $\delta^{88/86}\text{Sr}$, at least 6 NIST-987 standards and 2 IAPSO seawater standards were analyzed every 40 or fewer samples. During the period of study, repeated analyses yielded $\delta^{88/86}\text{Sr}_{\text{NIST987}} = 0.000 \pm 0.001\text{‰}$ ($2\sigma_{\text{SEM}}$, n=17) and $\delta^{88/86}\text{Sr}_{\text{IAPSO}} = 0.397 \pm 0.002\text{‰}$ ($\pm 2\sigma_{\text{SEM}}$, n=8). The current long-term values for the laboratory are $\delta^{88/86}\text{Sr}_{\text{NIST987}} = 0.000 \pm 0.001\text{‰}$ ($\pm 2\sigma_{\text{SEM}}$, n=235) and $\delta^{88/86}\text{Sr}_{\text{IAPSO}} = 0.396 \pm 0.002\text{‰}$ ($\pm 2\sigma_{\text{SEM}}$, n=133). After propagating measurement errors for $^{87}\text{Sr}/^{86}\text{Sr}$ and $^{88}\text{Sr}/^{86}\text{Sr}$ ratios, the overall uncertainty ($2\sigma_{\text{SD}}$) assigned to $\delta^{88/86}\text{Sr}$ is $\pm 0.020\text{‰}$ ($2\sigma_{\text{SD}}$).

Care was taken to ensure that uncertainties determined from the repeated analyses of standards apply to sample unknowns. Duplicates were determined by reanalyzing sample solutions (n = 4), as well as by re-dissolving and processing separate aliquots of powder (n = 6). As shown in Table AII-1, duplicates agree with original analyses within the uncertainties. Duplicate measurements are shown in Figure 3-1 as crosses.

$\delta^{13}\text{C}$ Segmentation and Stratigraphic Correlation

Magnetostratigraphy (Tarduno et al., 1995), benthic foraminiferal biostratigraphy (Arnaud-Vanneau and Sliter, 1995), and chemostratigraphy ($^{87}\text{Sr}/^{86}\text{Sr}$ and $\delta^{13}\text{C}$) have aided correlation of the section (Jenkyns, 1995; Jenkyns and Wilson, 1999). The Cretaceous stage boundaries are taken from Jenkyns and Wilson (1999). The nomenclature and segmentation of the

$\delta^{13}\text{C}$ intervals associated with OAE 1a follow Menegatti et al. (1998) and Bralower et al. (1999), based on study of the Cismon section in Italy. The C1 interval represents the pre-OAE 1a baseline of the $\delta^{13}\text{C}$ curve, with a mean value of $\sim 2.4\text{‰}$. The C2 interval starts with a progressive decrease of $\delta^{13}\text{C}$, but values oscillate around the baseline with a slightly lower mean of $\sim 1.8\text{‰}$. The C3 interval points to the minimum $\delta^{13}\text{C}$ within a relatively organic-rich interval overlying the wackestone of C2. The C4 interval correlates with an abrupt positive shift towards heavier values ($\sim 4.5\text{‰}$) immediately following C3. The C5 interval represents a segment with invariant $\delta^{13}\text{C}$ values ($\sim 3.6\text{‰}$). The C6 interval is characterized by another step-like abrupt increase to the maximum values of the entire section ($\sim 5.4\text{‰}$). The C7 interval bears the heaviest mean value of the entire section ($\sim 4.0\text{‰}$). The C8 interval represents the subsequent drop in $\delta^{13}\text{C}$ overlying C7, towards the upper Aptian.

In Figure 3-3 and AII-7, the $\delta^7\text{Li}$ values shown for Resolution Guyot are from Lechler et al. (2015). The nannoconid abundance data and $^{187}\text{Os}/^{188}\text{Os}$ ratios shown for the Cismon site are from Erba and Tremolada (2004) and Bottini et al. (2012), respectively. Atmospheric $p\text{CO}_2$ values reconstructed from analysis of the Cau section are from Naafs et al. (2016). The $\delta^{13}\text{C}$ segmentation criteria for these sections are mutually consistent. These $\delta^{13}\text{C}$ segments are unchanged from the original publications and were used in our study to correlate the three sections shown in the figures.

Supporting Elemental and Isotopic Results

Figure AII-1 plots CaCO_3 abundances, as well as Mg/Ca , Sr/Ca , and Mn/Sr ratios, versus stratigraphic height. On average, the samples have high CaCO_3 abundances ($\sim 95\text{ wt\%}$). Mg/Ca ratios are slightly elevated lower in the section and decrease upwards. Sr/Ca ratios average ~ 0.4

nmol/ μ mol before decreasing to 0.2 nmol/ μ mol upsection. Mn/Sr ratios are low and modestly decrease upsection from 0.3 to 0.2 mol/mol.

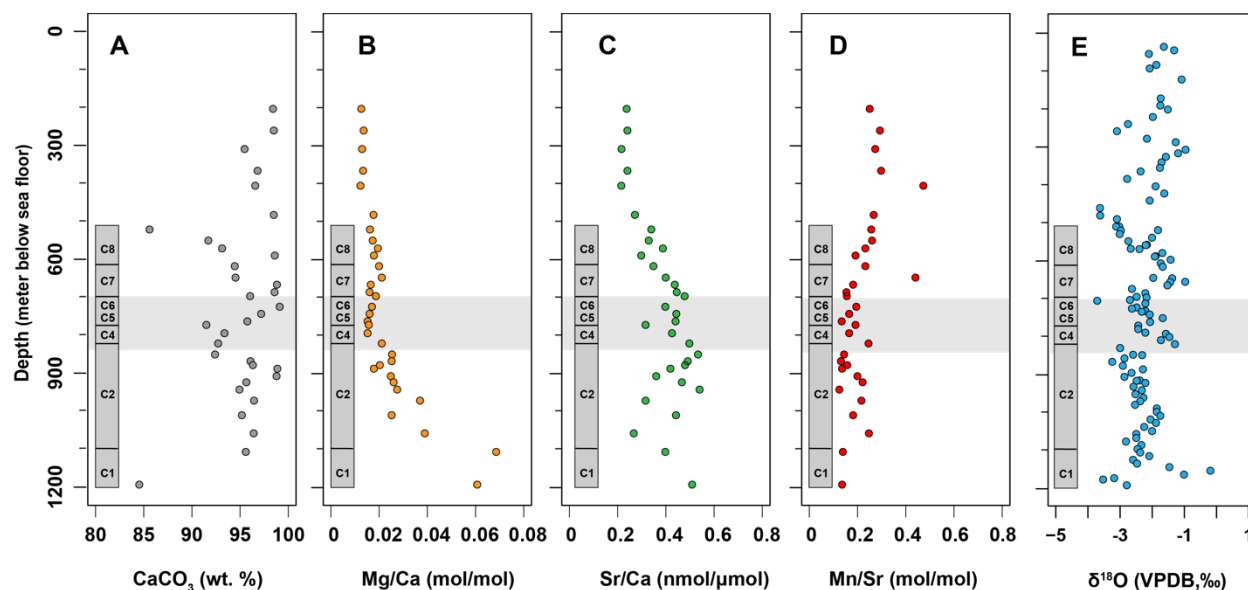


Figure AII-1 Stratigraphic height vs (A) CaCO_3 abundance, (B) Mg/Ca (mol/mol), (C) Sr/Ca (nmol/ μ mol), (D) Mn/Sr (mol/mol), and (E) $\delta^{18}\text{O}$ in bulk carbonate samples from ODP Hole 866A at Resolution Guyot.

Figures AII-2 – AII-3 cross plot various parameters. Both ordinary least squares (OLS) and standardized major axis (SMA) linear regression models were employed to evaluate the statistical significance of apparent correlations. Unlike the OLS model, the SMA model considers that both x and y variables have error. All regression statistics presented here are from the SMA model, but no differences between the two models were observed. No significant correlations exist, with the exception of the following: $\delta^{44/40}\text{Ca}$ vs. $\delta^{88/86}\text{Sr}$ ($R^2 = 0.66$, $p = 7.7 \times 10^{-8}$), $\delta^{44/40}\text{Ca}$ vs. Sr/Ca ($R^2 = 0.40$, $p = 1.3 \times 10^{-4}$), and $\delta^{88/86}\text{Sr}$ vs. Ca/Sr ($R^2 = 0.31$, $p = 1.0 \times 10^{-3}$).

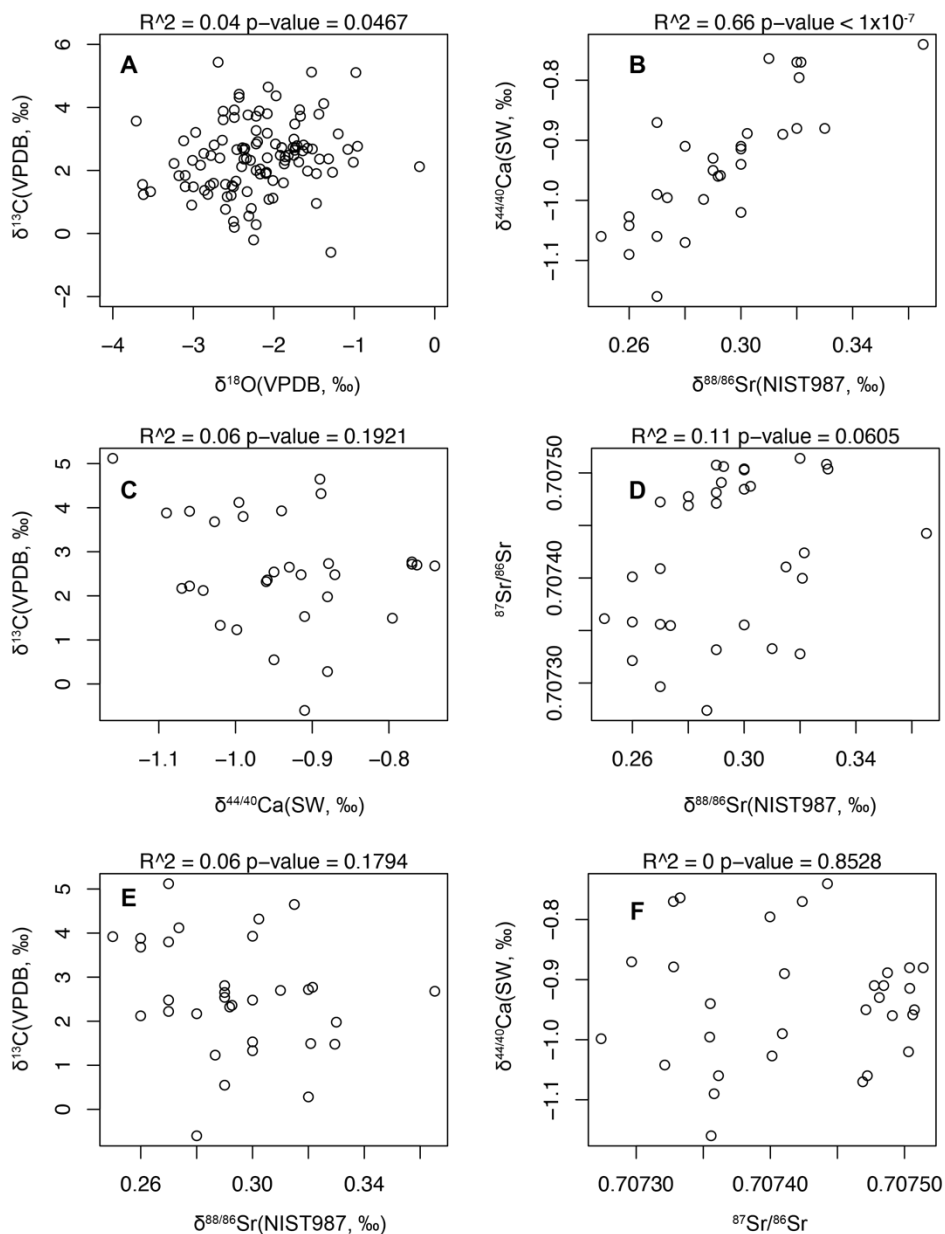


Figure AII-2 Cross-plots of various parameters measured for bulk carbonate samples from ODP Hole 866A at Resolution Guyot. R^2 and p-value are from the SMA regression model. (A) $\delta^{13}\text{C}$ vs $\delta^{18}\text{O}$, (B) $\delta^{44/40}\text{Ca}$ vs $\delta^{88/86}\text{Sr}$, (C) $\delta^{13}\text{C}$ vs $\delta^{44/40}\text{Ca}$, (D) $^{87}\text{Sr}/^{86}\text{Sr}$ vs $\delta^{88/86}\text{Sr}$, (E) $\delta^{13}\text{C}$ vs $\delta^{88/86}\text{Sr}$, and (F) $\delta^{44/40}\text{Ca}$ vs $^{87}\text{Sr}/^{86}\text{Sr}$.

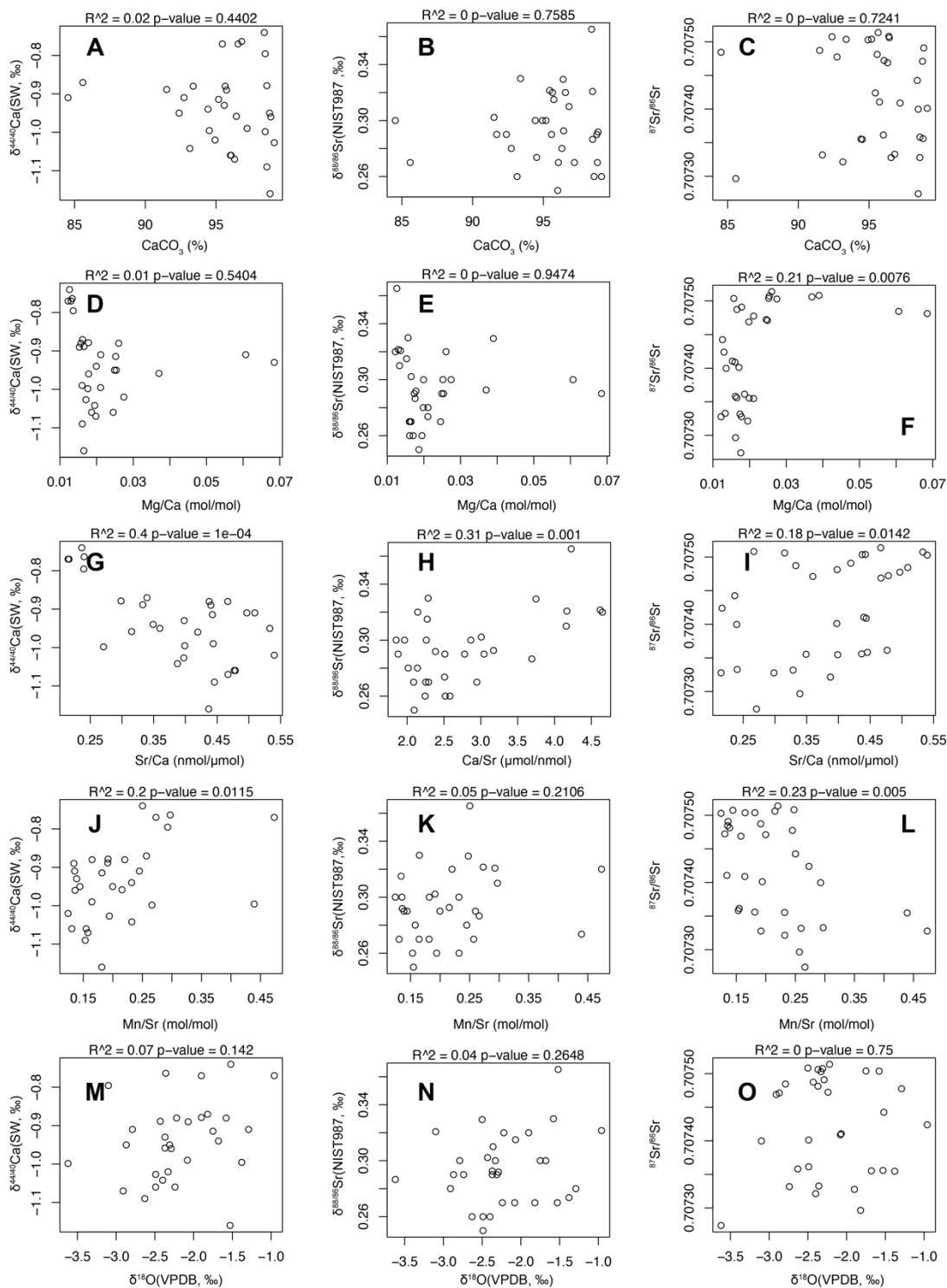


Figure AII-3 Cross-plots of isotope ratios and selected lithological proxies in bulk carbonate samples from the ODP Hole 866A at Resolution Guyot. R^2 and p -value are from the SMA regression model. (A) $\delta^{44/40}\text{Ca}$ vs CaCO_3 , (B) $\delta^{88/86}\text{Sr}$ vs CaCO_3 , (C) $^{87}\text{Sr}/^{86}\text{Sr}$ vs CaCO_3 , (D)

$\delta^{44/40}\text{Ca}$ vs Mg/Ca , (E) $\delta^{88/86}\text{Sr}$ vs Mg/Ca , (F) $^{87}\text{Sr}/^{86}\text{Sr}$ vs Mg/Ca , (G) $\delta^{44/40}\text{Ca}$ vs Sr/Ca , (H) $\delta^{88/86}\text{Sr}$ vs Ca/Sr , (I) $^{87}\text{Sr}/^{86}\text{Sr}$ vs Sr/Ca , (J) $\delta^{44/40}\text{Ca}$ vs Mn/Sr , (K) $\delta^{88/86}\text{Sr}$ vs Mn/Sr , (L) $^{87}\text{Sr}/^{86}\text{Sr}$ vs Mn/Sr , (M) $\delta^{44/40}\text{Ca}$ vs $\delta^{18}\text{O}$, (N) $\delta^{88/86}\text{Sr}$ vs $\delta^{18}\text{O}$, and (O) $^{87}\text{Sr}/^{86}\text{Sr}$ vs $\delta^{18}\text{O}$.

Sr Isotope Equilibration Sensitivity Analysis

Previous investigations have shown that Sr isotope equilibration between recrystallizing carbonate sediments and pore fluids only shifts $^{87}\text{Sr}/^{86}\text{Sr}$ ratios by 10 - 50 ppm (e.g., Richter and DePaolo, 1988; Richter and Liang, 1993). Negligible effects are predicted for $\delta^{88/86}\text{Sr}$ because the mixing end-members have less contrast in stable Sr isotope space. To illustrate this point, a simple two-component mixing model is employed to examine how shifts in carbonate $\delta^{88/86}\text{Sr}$ values ($\Delta^{88/86}\text{Sr}$) correspond to shifts in carbonate $^{87}\text{Sr}/^{86}\text{Sr}$ ratios ($\Delta^{87}\text{Sr}/^{86}\text{Sr}$). The equations are:

$$\delta^{88/86}\text{Sr}_{carb_altered} = \frac{(\delta^{88/86}\text{Sr}_{carb_initial} - \delta^{88/86}\text{Sr}_{fluid}) * ^{87}\text{Sr}/^{86}\text{Sr}_{carb_altered}}{(^{87}\text{Sr}/^{86}\text{Sr}_{carb_initial} - ^{87}\text{Sr}/^{86}\text{Sr}_{fluid})} \quad (\text{AII-1})$$

$$\delta^{88/86}\text{Sr}_{carb_altered} = \delta^{88/86}\text{Sr}_{carb_initial} + \Delta^{88/86}\text{Sr} \quad (\text{AII-2})$$

$$^{87}\text{Sr}/^{86}\text{Sr}_{carb_altered} = ^{87}\text{Sr}/^{86}\text{Sr}_{carb_initial} + \Delta^{87}\text{Sr}/^{86}\text{Sr} \quad (\text{AII-3})$$

where *carb_initial* refers to the initial carbonate before recrystallization, *carb_altered* denotes the altered carbonate after recrystallization, and *fluid* refers to pore water. Two example calculations are presented. In one case (Figure AII-6-A), $^{87}\text{Sr}/^{86}\text{Sr}_{carb_initial}$ values are set to the range of ratios measured for the present dataset and all other parameters are set to modern values. In the second case (Figure AII-6-B), $^{87}\text{Sr}/^{86}\text{Sr}_{carb_initial}$ is set to the average for the present dataset, $^{87}\text{Sr}/^{86}\text{Sr}_{fluid}$ is

allowed to range from 0.7082 to 0.7092, and the remaining two parameters are set to modern values. As figures AII-6-A and B show, $\Delta^{87}\text{Sr}/^{86}\text{Sr}$ values ranging up to 100 ppm yield $\Delta^{88/86}\text{Sr}$ values no higher than 0.03‰, which is only 0.01‰ higher than the long-term external reproducibility of the stable Sr isotope method and smaller than the total range of $\delta^{88/86}\text{Sr}$ variation measured for the samples (0.12‰).

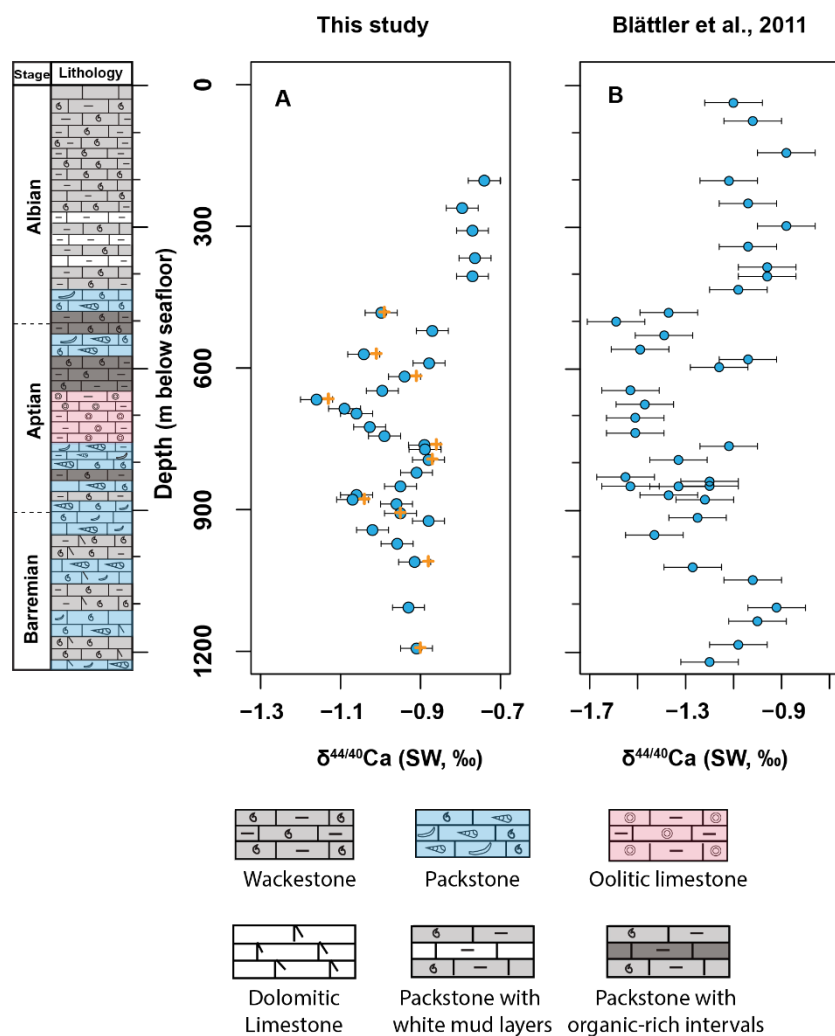


Figure AII-4. $\delta^{44/40}\text{Ca}$ values from Hole 866A of ODP Leg143 at Resolution Guyot, mid-Pacific Ocean. A) $\delta^{44/40}\text{Ca}$ values from this study with error bars of $\pm 0.05\text{‰}$. Crosses represent duplicate measurements. B) $\delta^{44/40}\text{Ca}$ values from Blättler et al. (2011) with error bars of $\pm 0.12\text{‰}$. Blättler et al. (2011) measured $\delta^{44/42}\text{Ca}$ relative to NIST-915a. The data and corresponding error bars of $\pm 0.06\text{‰}$ were converted using the equation: $\delta^{44/40}\text{Ca}_{\text{SW}} = \delta^{44/42}\text{Ca}_{915a} / 0.488 - 1.86$, where 0.488 assumes

mass fractionation follows a kinetic law and 1.86 is the value the Northwestern Laboratory measures for 915a relative to seawater (e.g., Du Vivier et al., 2015).

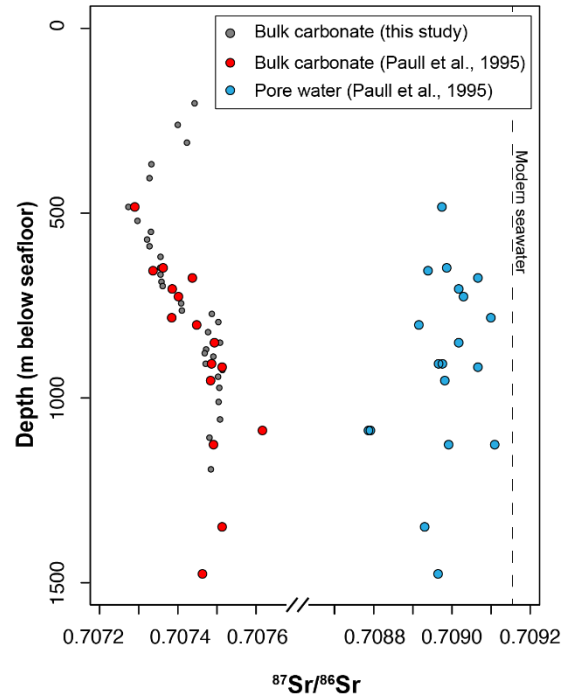


Figure AII-5 $^{87}\text{Sr}/^{86}\text{Sr}$ records of porewater (Paull et al., 1995) and bulk carbonate (This study; Paull et al., 1995).

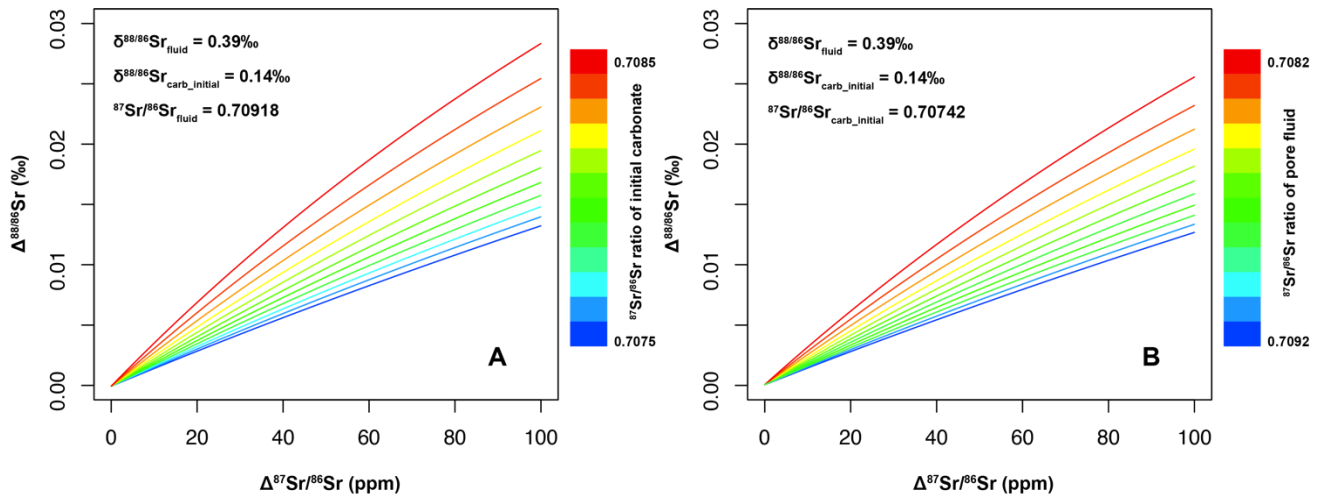


Figure AII-6 Sensitivity test for $\delta^{88/86}\text{Sr}$ response to early diagenetic $^{87}\text{Sr}/^{86}\text{Sr}$ shifts. A) $^{87}\text{Sr}/^{86}\text{Sr}_{\text{carb_initial}}$ values set to the range of ratios measured for the present dataset and all other

parameters set to modern values. B) $^{87}\text{Sr}/^{86}\text{Sr}_{\text{carb_initial}}$ set to the average for the present dataset, $^{87}\text{Sr}/^{86}\text{Sr}_{\text{fluid}}$ allowed to range from 0.7082 to 0.7092, and the remaining two parameters set to modern values.

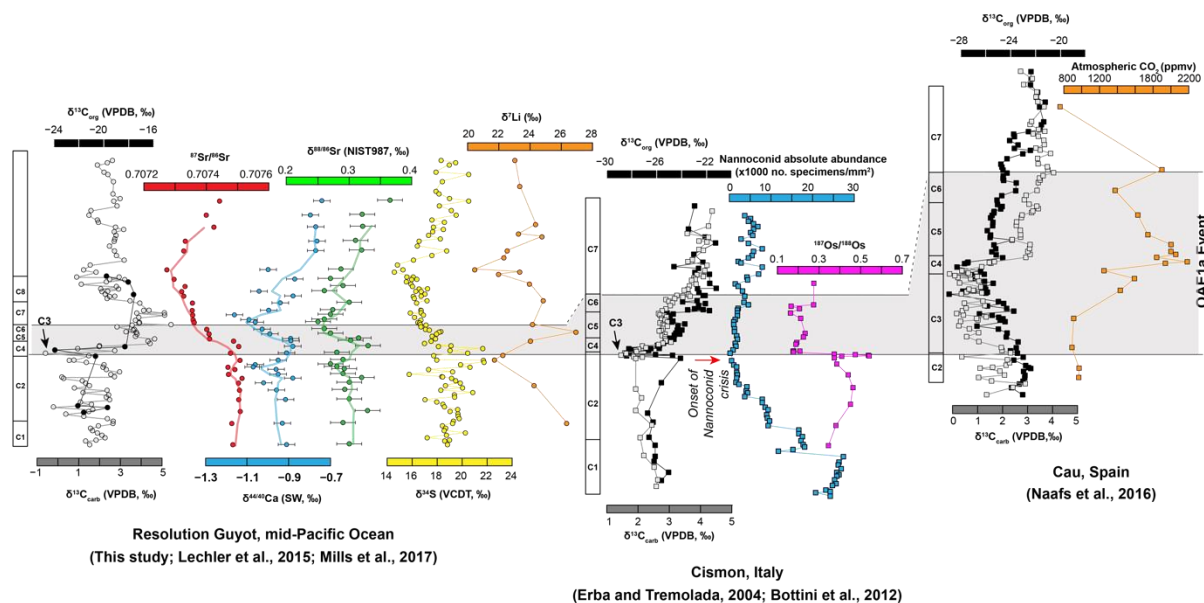


Figure AII-7 Stratigraphic correlation of various geochemical proxy data for the entire study interval. Figure 3-3 shows the OAE 1a interval.

Table AII-1 Elemental, C, O, Ca, and Sr isotope geochemistry of carbonate samples from Hole 866A, ODP Leg 143, Resolution Guyot, mid-Pacific

Depth (mbsf)	$\delta^{13}\text{C}$ (VPDB, ‰)	$\delta^{18}\text{O}$ (VPDB, ‰)	$\delta^{44/40}\text{Ca}$ (SW, ‰)	$\delta^{44/40}\text{Ca}$ (SW, ‰) Duplicate	$\delta^{88/86}\text{Sr}$ (NIST987, ‰)	$\delta^{88/86}\text{Sr}$ (NIST987, ‰) Duplicate
203.40	2.72	-1.61	-0.74		0.37	
261.33	1.34	-3.24	-0.80		0.32	0.33
309.25	2.77	-1.12	-0.77		0.32	
367.34	2.7	-2.36	-0.76		0.31	
405.83	2.68	-1.8	-0.77		0.32	
483.15	1.28	-3.41	-1.00	-0.99	0.29	0.28
521.4	2.6	-1.82	-0.87		0.27	

550.52	2.9	-2.68			0.29	
571.15	2.04	-2.21	-1.04	-1.01	0.26	
589.87	2.76	-1.96	-0.88			
618.34	4	-1.7	-0.94	-0.91	0.30	
648.40	4.2	-1.38	-1.00		0.27	0.28
666.82	5.12	-1.6	-1.16	-1.13	0.27	
686.30	3.7	-2.67	-1.09		0.26	
696.8	3.92	-2.37	-1.06		0.25	
725.1	3.68	-2.4	-1.03		0.26	
744.15	3.8	-2.08	-0.99		0.27	0.27
763.2	4.65	-1.98	-0.89	-0.86	0.32	
772.65	4.32	-2.43	-0.89		0.30	
794.45	2	-1.72	-0.88	-0.87	0.33	
821.6	-0.64	-1.3	-0.91		0.28	0.29
850.81	0.52	-2.3	-0.95		0.29	
868.9	2.22	-2.31	-1.06		0.27	
878.8	2.17	-2.86	-1.07	-1.04	0.28	0.29
888.17	2.3	-2.4	-0.96		0.29	
907.85	2.54	-2.87	-0.95	-0.95	0.29	
924	0.31	-2.54	-0.88		0.32	
943.13	1.33	-2.51	-1.02		0.30	
972.33	2.4	-2.25	-0.96		0.29	
1010.93	2.53	-1.81	-0.91	-0.88	0.30	
1058.20	1.5	-2.59			0.33	0.32
1107.2	2.65	-2.27	-0.93		0.29	
1193.75	1.49	-2.84	-0.91	-0.90	0.30	

Table AII-1 Continued.

$^{87}\text{Sr}/^{86}\text{Sr}$	$^{87}\text{Sr}/^{86}\text{Sr}$ Duplicate	Ca ($\mu\text{mol/g}$)	Na ($\mu\text{mol/g}$)	Mg ($\mu\text{mol/g}$)	Sr (nmol/g)	Mn (nmol/g)
0.70744		9841	36	124	2328	582
0.70740		9847	35	134	2362	692
0.70742		9544	36	124	2066	564
0.70733	0.70733	9681	31	129	2328	692
0.70733		9656	44	118	2077	983
0.70727	0.70727	9848	64	173	2667	710
0.70730		8559	73	138	2905	746
0.70733		9170	108	159	3012	783
0.70732		9315	100	181	3609	837
0.70733		9859	57	175	2943	564
0.70736		9443	63	188	3297	764
0.70735		9452	61	199	3770	1656
0.70736	0.70735	9882	69	163	4314	783
0.70736		9859	65	159	4394	673
0.70736		9602	51	179	4580	710
0.70740		9911	47	169	3938	764
0.70741		9719	45	156	4314	710
0.70741		9574	54	146	4212	564
0.70749		9151	49	151	3045	582
0.70750		9339	54	147	4085	673
0.70748	0.70748	9274	98	196	4607	1129
0.70751		9239	89	234	4924	710
0.70747		9606	70	236	4599	601
0.70747		9631	67	191	4499	710

0.70749		9887	30	176	4147	564
0.70747		9878	24	246	3553	710
0.70751		9564	87	249	4463	983
0.70750	0.70750	9493	88	261	5126	637
0.70751		9643	66	357	3041	655
0.70750		9518	39	240	4211	764
0.70751		9640	59	376	2571	637
0.70748		9557	63	655	3804	528
0.70748		8454	24	513	4305	582

Table AII-2 Slopes, intercepts, coefficients of determination, and p-values of datasets examined in Figure 3-2

	Dataset	Slope	Intercept	R^2	p -value	Reference
$\delta^{44/40}\text{Ca}$ vs [Sr] (Figure 3-2A)	OAE 1a carbonate	-0.00091 ± 0.00018	-0.64 ± 0.06	0.47	2.1×10^{-5}	This study
	Inorganic calcite	-0.00094 ± 0.00005	-0.85 ± 0.05	0.91	2.2×10^{-16}	Tang et al. (2008)
	Silurian carbonate	-0.00097 ± 0.00017	-0.92 ± 0.09	0.53	1.1×10^{-6}	Farkaš et al. (2016)
	P-Tr carbonate	-0.00025 ± 0.00003	-1.21 ± 0.02	0.35	3.1×10^{-5}	Wang et al. (2019)
$\delta^{44/40}\text{Ca}$ vs $\delta^{88/86}\text{Sr}$ (Figure 3-2B)	OAE 1a carbonate	0.194 ± 0.027	0.475 ± 0.025	0.66	7.7×10^{-8}	This study
	Inorganic calcite	0.185 ± 0.019	0.286 ± 0.033	0.96	6.0×10^{-4}	Böhm et al. (2012)
	P-Tr carbonate	0.131 ± 0.082	0.560 ± 0.109	0.07	0.12	Wang et al. (2019)

APPENDIX III

Geological settings, lithology, leaching experiments, and data for Marinoan cap carbonate samples

Geological settings and lithology

The globally distributed Marinoan cap-carbonate sequences (e.g. Hoffman and Li, 2009) comprising thick dolomite and limestone sequences overlie glacial deposits and correlative sequence boundaries of the ca. 635Ma Marinoan glaciation. The base is marked by the deposition laterally extensive cap dolostone consisting of abundant macropeloids, low-angle cross-stratification, and giant wave ripple structures (Allen and Hoffman, 2005; Hoffman et al., 2011). A flooding surface at the top of the cap dolostone coincides with an abrupt shift to either limestone or shale (e.g. Hoffman and Schrag, 2002; Halverson et al., 2004; Halverson et al., 2005; Hoffman et al., 2011). In Namibia, carbonate continues after the cap dolostone (Figure 4-1) making it a favorable choice for seawater geochemistry study. The present study focuses exclusively on the Namibian Marinoan cap carbonate sequences.

During Cryogenian and early Ediacaran, the northern Namibia is thought to be a marine carbonate platform situated in subtropical latitudes (Li et al., 2008). The convergence of Congo and Kalahari cratons of Africa and their collision with cratons of South America caused the regional subsidence (Stanistreet et al., 1991; Passchier et al., 2002; Goscombe & Gray, 2008; Oyhantc,abal et al., 2009) and formed the Otavi platform with a south-dipping foreslope (Halverson et al., 2002; Hoffman, 2005; Hoffman and Halverson, 2008). The Otavi Group comprises four Subgroups, namely Ombombo, Ugab, Abenab, and Tsumeb Subgroups (Hoffman and Prave, 1996). The Ghuab Formation at the base of Tsumeb Subgroup consists predominantly

of carbonate matrix diamictite with clasts derived from the underlying Abenab Subgroup and is interpreted to be glacial deposits of Marinoan glaciation (e.g. Hoffmann et al., 2004). The overlying Meieberg Formation comprising a ~250–400 m thick transgressive-high stand sequence is the cap carbonate to the Marinoan glacials and is divided into three members: the basal Keilberg Member (cap dolostone), a middle member comprising limestone and dolomite rhythmite, and an upper member consisting of dolomite grainstone (Hoffman and Halverson, 2008; Hoffman et al., 2011). Two sections, Arbeitsgenot (19°35.8'S, 16°53.9'E) and Ombaatjie (19°18.9'S, 13°59.3'E), were measured for Ca and Sr isotope (Figure 4-2) and elemental geochemistry (Figure AIII-1 and Table AIII-1) in this study. The Maieberg Formation at Arbeitsgenot, containing ~28 m of micritic cap dolostone with columnar stromatolitic structures and wave ripples, ~95 m of limestone rhythmites, and ~80m of dolomite grainstones, is interpreted to be deposited in the outer platform setting (Hurtgen et al., 2006; Hoffman et al., 2011). Although the upper dolomite member of the Maieberg Formation at Ombaatjie is not accessible, the section is thought to represent the inner platform setting (Figure 4-1).

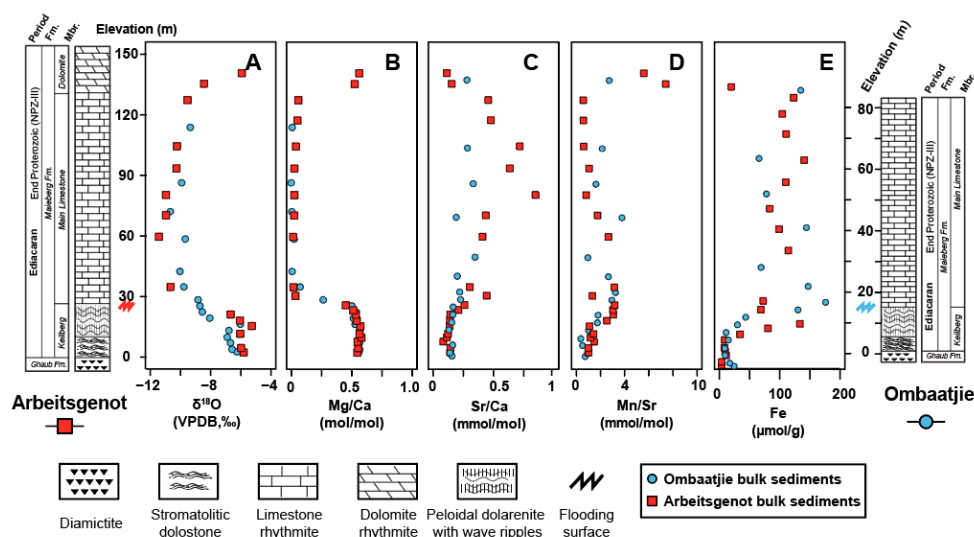


Figure AIII-1 Stratigraphic heights vs (A) $\delta^{18}\text{O}$, (B) Mg/Ca, (C) Sr/Ca, (D) Mn/Sr, and (E) Fe in

bulk carbonate samples from Arbeitsgenot and Ombaatjie sections.

Leaching experiments

The measured $^{87}\text{Sr}/^{86}\text{Sr}$ ratios are generally higher than reported seawater values (e.g. Halverson et al., 2010; Cox et al., 2016; Liu et al., 2018). Liu et al. (2013; 2014; 2018) reported that certain geochemical signatures (including Mg, Sr, C, and O) in cap carbonates can be contaminated by non-carbonate phases yielding high heterogeneity. Although most samples produced little to no residue after reaction with 5% HNO_3 , it is relevant to question whether different mineral phases (e.g. absorbed metals, recrystallized calcite, dolomite; Bailey et al., 2000; Liu et al., 2013) carry different geochemical signals. Another question is whether the dolomite preserves primary signatures or signals of diagenesis and carbonate alteration in burial environment. To address these questions, five samples from Ombaatjie section and five samples Arbeitsgenot section spanning across the measured sections were selected for a sequential leaching experiment, modified from Bailey et al. (2000) and Liu et al. (2013). Previous studies have shown that dilute acetic acid (HAc) can dissolve carbonate without affecting non-carbonate phases (e.g., Bailey et al., 2000; Bayon et al., 2002). We employed HAc solutions with concentrations of 0.25%, 1%, and 5%. Subsamples of micro-drilled powders (~200 mg/sample) were weighed into acid-cleaned 50 mL centrifuge tubes and first reacted with ~25 mL of 1N ammonium acetate (NH_4Ac , buffered to pH=8.2) to isolate surface-adsorbed phases and other exchangeable cations (Gao, 1990; Bailey et al., 2000). The remaining residues were then sequentially reacted with ~15 mL of 0.25%, 1%, and 5% HAc. For each step, mixtures were agitated in an ultrasonic bath for 15 min and then centrifuged at 3500 rpm for 15 min. The supernatants were filtered through 0.45 μm polypropylene syringe filters into acid cleaned Teflon vials, dried at 90°C, and re-dissolved in 5% HNO_3 . Before proceeding to the next step, the residues were rinsed with Milli-Q water, which was discarded after

centrifuging. Step-leachates along with all samples were analyzed for Ca and Sr (both radiogenic and stable) isotope compositions and elemental concentration, following the procedure presented in previous studies of the group (Lehn et al., 2013; Andrews et al., 2016; Wang et al., 2019).

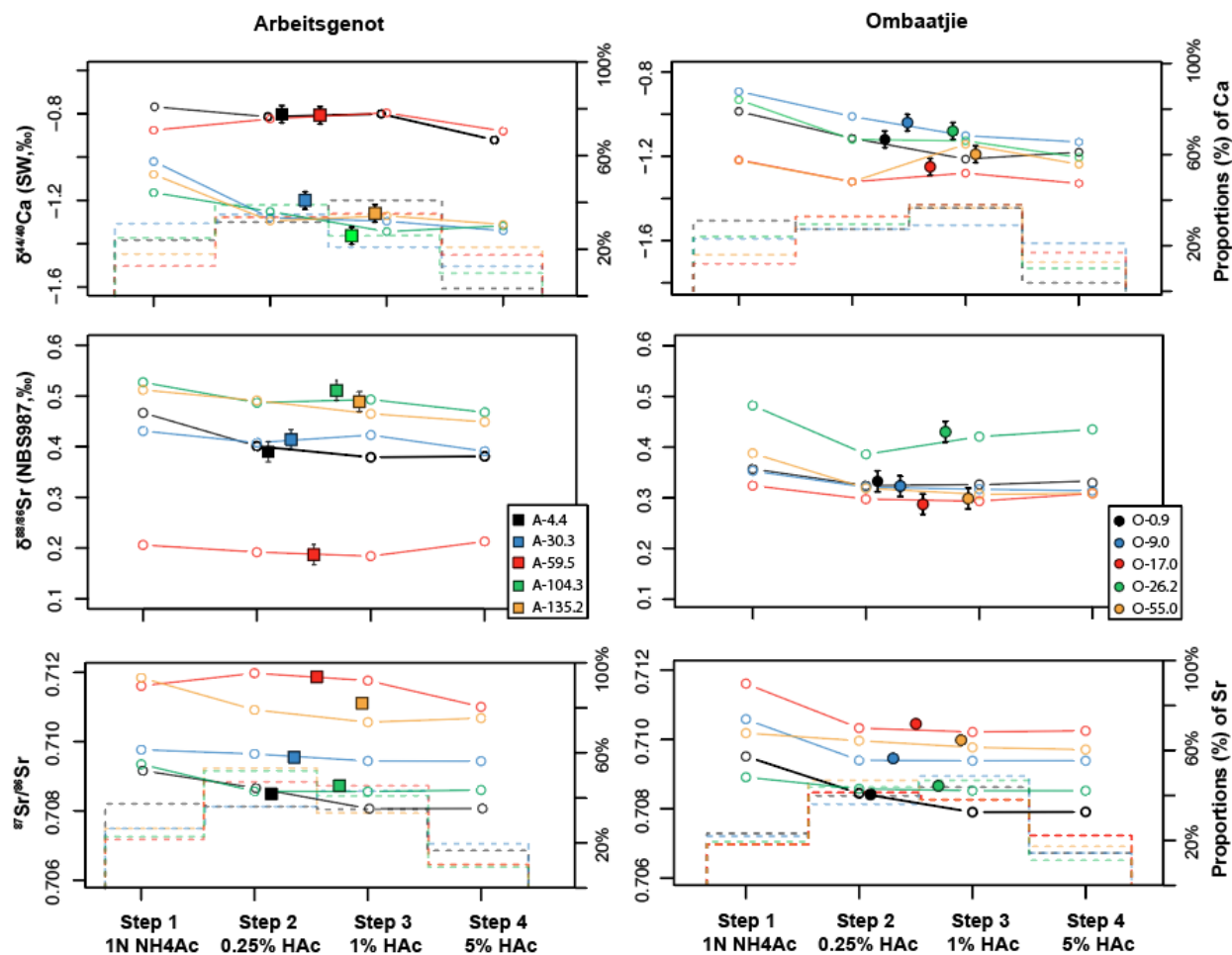


Figure AIII-2 Sequential leaching results of the cap carbonate rock from Arbeitsgenot (left) and Ombaatjie (right) sections. Open circles show $\delta^{44/40}\text{Ca}$, $^{87}\text{Sr}/^{86}\text{Sr}$, and $\delta^{88/86}\text{Sr}$ results of sequential leachates. Filled circles show data for the original 5% HNO_3 leachates. Dashed histograms show the proportions (%) of Ca and Sr obtained for each leaching step relative to the original 5% HNO_3 leachates.

The results are plotted in Figure AIII-2 and Table AIII-2 provides the data. Relative to the original 5% HNO_3 leachates, which we assume dissolved all of the carbonate and dolomite powders present, the four sequential leaching steps in total acquired >95% of the Ca and >95% of

the Sr for samples in both sections. Figure AIII-2 also compares the measured isotope ratios for each leachate with the isotope ratios determined for the original 5% HNO₃ leachates (filled circles), and Table AIII-2 provides the weighted average isotope ratios for all leachates combined, determined using the concentrations and isotope ratios of each step. The weighted average isotopic values determined for the sequential leachates agree with the values measured for the original 5% HNO₃ leachates. As shown in Figure AIII-2, the first step (1N NH₄Ac) exhibits the largest differences with values obtained from the original 5% HNO₃ leachates. Besides the first step, other sequential leaching steps did not reveal major discrepancies for $\delta^{44/40}\text{Ca}$ and $\delta^{88/86}\text{Sr}$ values.

Correlation of two sections

With the consideration that the cap carbonate sequence may have deposited diachronously (e.g. Hoffman et al., 2007), the correlation among different sections is conducted by the $\delta^{13}\text{C}$ chemostratigraphy, which involves the well-documented negative $\delta^{13}\text{C}$ excursion occurred in the Marinoan cap dolostone (e.g. Hoffman et al., 1998; Kennedy et al., 2001; Hoffman et al., 2007). The $\delta^{13}\text{C}$ records in two studied sections show broadly similar patterns. The Arbeitsgenot and Ombaatjie begins at subtly different values (Arbeitsgenot at -2.5‰ and Ombaatjie at -3.0‰) and reaches their minimums of -6‰ at the lower part of the main limestone, which are in good agreement with the records of the platform (Ombaatjie) and platform-edge (Arbeitsgenot) reported in Hoffman et al. (2007). The $\delta^{13}\text{C}$ at Arbeitsgenot then increases to 0‰ in the upper dolomite Mbr. of Maieberg Fm., while the Ombaatjie increases to -5‰ in the upper part of the main limestone Mbr. In the effort to avoid the diachronism and other biases, in Figure 4-1 and Figure 4-4, we employ the base of the cap dolostone as a first datum and the $\delta^{13}\text{C}$ minimum as second datum. Thus, the flooding surface (top of the cap dolostone) correlate despite different thickness in two cap dolostones (~26m at Arbeitsgenot v.s. ~17m at Ombaatjie) indicating fairly similar

depositional environment with different paleobathymetries.

Estimates of meltwater and seawater geochemistry

The shape of meltwater and seawater mixing is determined by the chemical and isotopic compositions of meltwater and seawater mixing members. Ideally, good estimates could be accomplished by direct measurements in well-preserved marine and freshwater fossil archives. However, the present study focuses on a relatively abrupt deglaciation process at the end of Neoproterozoic, which makes accurate estimation more challenging. Here, we rely on the modern measurements of glacial meltwater (Tranter, 2003; Krabbenhöft et al., 2010; Tipper et al., 2010; Hindshaw et al., 2011; Stevenson et al., 2016) and numerical modeling fits of Marinoan seawater (e.g., Ahm et al., 2019; Wei et al., 2019) and summarize them in Table AIII-1.

		Value	Unit
Meltwater	[Ca]	16	ppm
	[Sr]	0.075	ppm
	$\delta^{44/40}\text{Ca}$	-0.4	‰
	$\delta^{88/86}\text{Sr}$	0.2	‰
Seawater	[Ca]	412	ppm
	[Sr]	7.9	ppm
	$\delta^{44/40}\text{Ca}$	-0.6	‰
	$\delta^{88/86}\text{Sr}$	0.7	‰

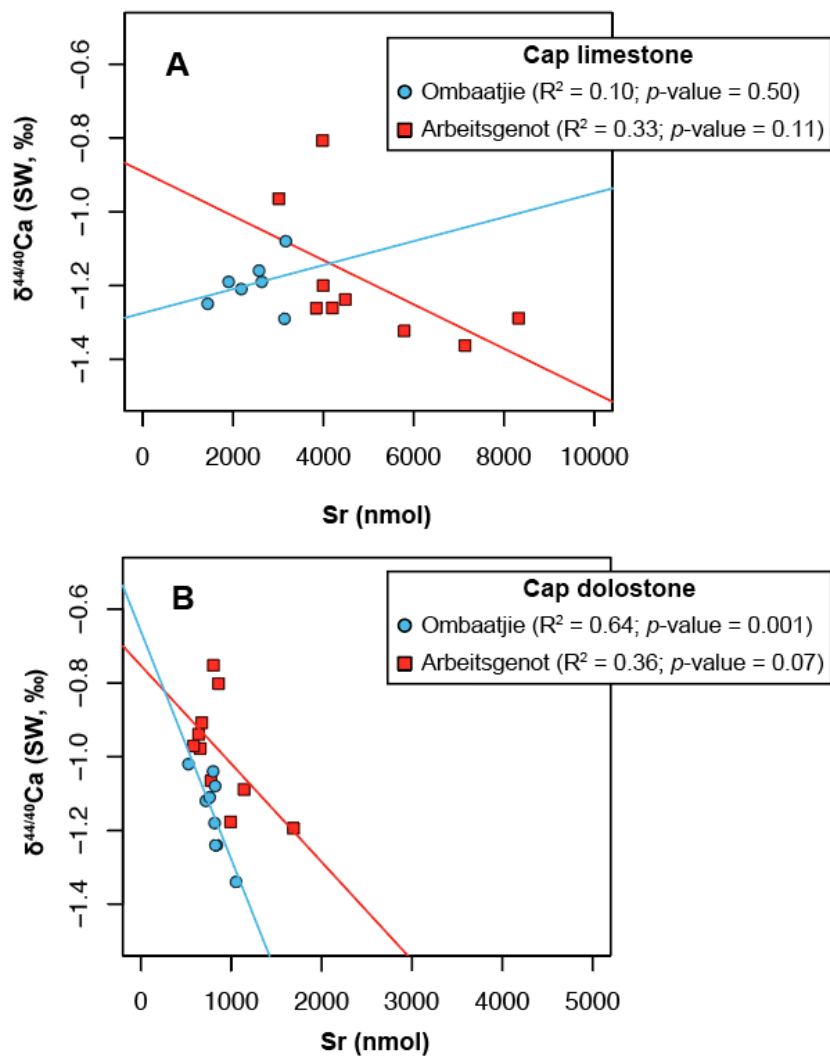


Figure AIII-3 Cross-plot of $\delta^{44/40}\text{Ca}$ vs Sr concentrations in the main limestone cap limestone (A) and the Keilberg cap dolostone (B).

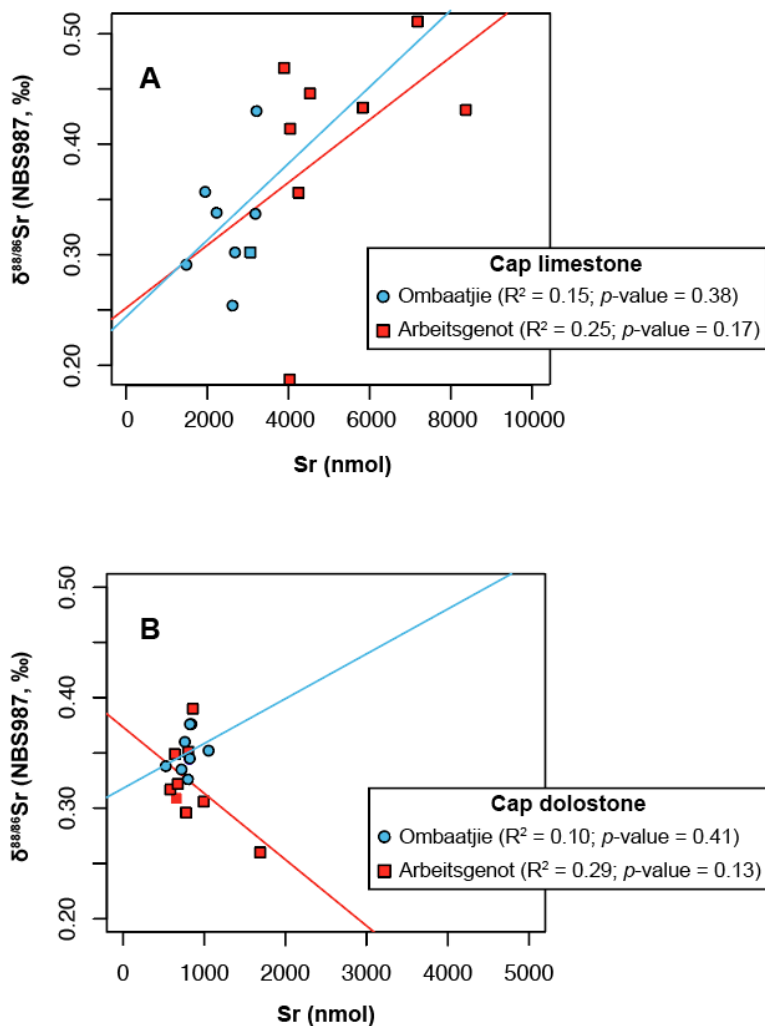


Figure AIII-4 Cross-plot of $\delta^{44/40}\text{Ca}$ vs Sr concentrations in the main limestone (A) and the Keilberg cap dolostone (B)

Table AIII-1 Elemental, C, O, Ca, and Sr isotope geochemistry of Marinoan cap carbonate

Elevation (m)	$^{87}\text{Sr}/^{86}\text{Sr}$	$^{87}\text{Sr}/^{86}\text{Sr}$ Dup.	$\delta^{88/86}\text{Sr}$ (‰)	$\delta^{88/86}\text{Sr}$ Dup. (‰)	$\delta^{44/40}\text{Ca}$ (‰)	$\delta^{44/40}\text{Ca}$ Dup. (‰)	$\delta^{44/40}\text{Ca}$ ^{48}Ca - ^{43}Ca spike (‰)	$\delta^{44/42}\text{Ca}$ ^{48}Ca - ^{43}Ca spike (‰)
Arbeitsgenot								
2.2	0.70845		0.35		-0.75			
4.4	0.70849		0.39	0.36	-0.80			
7.6	0.70854	0.70855	0.31		-0.98			

9.6	0.70856		0.32	0.32	-0.97			
11.4	0.70868		0.35		-0.94			
15.3	0.70845		0.32	0.32	-0.91			
18	0.70976	0.70976	0.30	0.30	-1.07			
21	0.70981		0.31		-1.18	-1.21	-1.20	-0.64
23.2					-1.09			
25.7	0.71008		0.26		-1.19	-1.21	-1.21	-0.66
30.3	0.70954	0.70955	0.41		-1.20			
34.6	0.71145		0.30		-0.97	-1.01	-1.05	-0.57
59.5	0.71187		0.19	0.19	-0.81			
70.1	0.71026		0.36		-1.26			
80.2	0.70856		0.43		-1.29		-1.28	-0.66
93.4	0.70985		0.43	0.42	-1.32			
104.3	0.70873	0.70872	0.51		-1.36			
117.2	0.70855		0.47		-1.26			
127.2	0.70887		0.45		-1.24			
135.2	0.71106	0.71106	0.49		-1.26	-1.24	-1.25	-0.67
140.5	0.70931		0.32		-1.30			
Ombaatjie								
0.1	0.70872		0.34		-1.18			
0.9	0.70841		0.34		-1.12			
3	0.70901		0.35		-1.08	-1.08		
4.8	0.70864	0.70863	0.34		-1.02	-1.05		
7	0.70857		0.36		-1.11			
9	0.70945	0.70944	0.33	0.33	-1.04	-1.07		
11	0.70953		0.38		-1.24			
13	0.70960		0.38		-1.24			
15	0.71014	0.71017	0.35	0.35	-1.34		-1.33	-0.70

17	0.71040	0.71037	0.29	0.29	-1.25		-1.24	-0.67
21.2	0.70952	0.70955	0.36	0.36	-1.19	-1.17		
26.2	0.70866	0.70866	0.43	0.42	-1.08			
36.7	0.70948	0.70944	0.34	0.34	-1.21		-1.25	-0.66
45.6	0.70922		0.34		-1.29			
55	0.70998	0.70997	0.30	0.30	-1.19	-1.21	-1.16	-0.64
73	0.71048		0.25		-1.16			

Table AIII-1 Continued.

CaCO ₃	Ca	Mg	Mn	Sr	Al	Ba	Fe	K	Na
(%)	($\mu\text{mol/g}$)	($\mu\text{mol/g}$)	(nmol/g)	(nmol/g)	($\mu\text{mol/g}$)	(nmol/g)	($\mu\text{mol/g}$)	($\mu\text{mol/g}$)	($\mu\text{mol/g}$)
93.9	5971	5369	602	802	13	44	4	8	7
90.6	6284	5728	642	859	15	44	4	9	13
97.8	5880	5312	847	657	15	80	11	9	11
96.9	5465	5221	967	582	17	126	10	8	9
98	5425	5047	920	639	15	0	8	8	21
95.4	5182	4883	728	673	15	73	9	11	18
91.4	5853	5227	1966	776	19	96	34	11	31
89.3	7290	6404	3040	993	20	73	80	9	16
86.7	5612	4730	3458	1141	14	86	134	9	28
80.4	6693	4966	5370	1689	20	95	231	14	22
83	9138	494	5224	3995	27	86	69	14	25
	1011					87	73		5
85.8	9	278	9483	3013	22			26	
			1061			73	114		9
85.2	9869	237	2	3983	24			28	
87.5	9776	360	7354	4200	26	66	99	12	3

85	9889	400	6789	8320	17	153	83	16	21
84.4	9207	370	6080	5786	16	87	110	15	22
	1005					92	141		24
83.4	5	623	4296	7133	19			17	
83.5	8157	664	2239	3846	16	73	111	9	14
85.4	9976	952	2548	4485	17	0	104	12	25
86.6	5685	4914	6171	833	22	87	123	34	17
95.3	5526	5110	3313	593	13	144	20	15	26
98.1	5605	5268	584	817	11	44	26	10	6
98.8	5588	5309	764	721	12	77	18	9	8
99.7	5414	5122	437	823	11	80	11	8	17
99.4	5350	5074	200	526	13	66	10	9	14
86.2	6235	5906	783	761	15	99	16	8	27
97.8	5556	4933	1402	800	18	271	12	11	19
96.4	5502	4752	1529	840	19	153	31	10	20
92.5	5293	4779	2567	824	20	371	45	12	14
82.1	4853	4099	3113	1052	21	283	131	17	13
87	6847	3100	4696	1439	23	160	177	21	18
74.2	9989	1365	5097	1904	19	371	148	7	15
92.8	9400	254	3076	3166	19	248	70	6	16
	1206								
70.8	0	657	8300	2182	15	291	145	9	58
86.2	9751	238	5151	3139	12	363	79	6	22
83.1	9638	143	5697	2639	22	563	67	18	24
72.6	9541	270	7044	2575	21	291	136	21	22

Table AIII-2 Ca and Sr isotope geochemistry of leachates from sequential leaching experiment

Sample	Leaching Step	Ca	$\delta^{44/40}\text{Ca}$	$\delta^{44/40}\text{Ca}$ Weigh. Ave.	Sr	$^{87}\text{Sr}/^{86}\text{Sr}$	$^{87}\text{Sr}/^{86}\text{Sr}$ Weigh. Ave.	$\delta^{88/86}\text{Sr}$	$\delta^{88/86}\text{Sr}$ Weigh. Ave.
		%	(‰)	(‰)	%			(‰)	(‰)
A4.4	1N NH ₄ Ac	24%	-0.77		30%	0.70913		0.47	
	0.25% HAc	32%	-0.81	-0.80	29%	0.70863	0.70854	0.40	0.41
	1% HAc	41%	-0.80		28%	0.70803		0.38	
	5% HAc	3%	-0.92		13%	0.70804		0.38	
1N NH ₄ Ac	31%	-1.02	21%		0.70976	0.43			
A30.3	0.25% HAc	35%	-1.28	-1.21	29%	0.70964	0.70957	0.41	0.42
	1% HAc	21%	-1.30		35%	0.70944		0.42	
	5% HAc	13%	-1.34		15%	0.70943		0.39	
	1N NH ₄ Ac	13%	-0.88		17%	0.71161		0.21	
A59.5	0.25% HAc	34%	-0.82	-0.83	38%	0.71197	0.71155	0.19	0.19
	1% HAc	35%	-0.80		37%	0.71176		0.18	
	5% HAc	18%	-0.88		8%	0.71100		0.21	
	1N NH ₄ Ac	25%	-1.16		18%	0.70935		0.53	
A104.3	0.25% HAc	39%	-1.25	-1.26	42%	0.70857	0.70871	0.49	0.50
	1% HAc	26%	-1.34		33%	0.70856		0.49	
	5% HAc	10%	-1.32		7%	0.70860		0.47	
	1N NH ₄ Ac	18%	-1.08		21%	0.71189		0.51	
A135.2	0.25% HAc	27%	-1.30	-1.25	43%	0.71096	0.71110	0.49	0.49
	1% HAc	34%	-1.27		27%	0.71061		0.47	
	5% HAc	21%	-1.31		9%	0.71072		0.45	
	1N NH ₄ Ac	18%	-1.08		21%	0.71189		0.51	

Table AIII-2 Continued.

Sample	Leaching Step	Ca	$\delta^{44/40}\text{Ca}$	$\delta^{44/40}\text{Ca}$ Weigh. Ave.	Sr	$^{87}\text{Sr}/^{86}\text{Sr}$	$^{87}\text{Sr}/^{86}\text{Sr}$ Weigh. Ave.	$\delta^{88/86}\text{Sr}$	$\delta^{88/86}\text{Sr}$ Weigh. Ave.
--------	---------------	----	---------------------------	---	----	---------------------------------	---	---------------------------	---

		%	(‰)	(‰)	%		(‰)	(‰)
O0.9	1N NH ₄ Ac	31%	-0.99		19%	0.70951	0.36	
	0.25% HAc	28%	-1.11	-1.11	33%	0.70845	0.33	0.70839
	1% HAc	37%	-1.21		36%	0.70790	0.33	
	5% HAc	4%	-1.18		12%	0.70791	0.33	
1N NH ₄ Ac	23%	-0.89	18%		0.71058	0.36		
O9	0.25% HAc	27%	-1.01	-1.04	30%	0.70940	0.32	0.70960
	1% HAc	29%	-1.10		40%	0.70938	0.32	
	5% HAc	21%	-1.13		12%	0.70939	0.32	
	1N NH ₄ Ac	12%	-1.22		15%	0.71166	0.33	
O17	0.25% HAc	32%	-1.32	-1.29	34%	0.71037	0.30	0.71051
	1% HAc	38%	-1.28		32%	0.71026	0.30	
	5% HAc	18%	-1.33		19%	0.71030	0.31	
	1N NH ₄ Ac	24%	-0.93		16%	0.70891	0.48	
O26.2	0.25% HAc	29%	-1.12	-1.09	36%	0.70857	0.39	0.70860
	1% HAc	37%	-1.13		39%	0.70852	0.42	
	5% HAc	10%	-1.21		9%	0.70852	0.44	
	1N NH ₄ Ac	16%	-1.22		15%	0.71018	0.39	
O55	0.25% HAc	34%	-1.32	-1.23	39%	0.70996	0.32	0.70990
	1% HAc	37%	-1.14		32%	0.70977	0.31	
	5% HAc	13%	-1.24		14%	0.70971	0.31	
	1N NH ₄ Ac	16%	-1.22		15%	0.71018	0.39	

REFERENCES

- Adams, J.E. and Rhodes, M.L. (1960) Dolomitization by seepage refluxion. AAPG Bull. 44, 1912-1920.
- Ahm, A.-S.C., Bjerrum, C.J., Blättler, C.L., Swart, P.K. and Higgins, J.A. (2018) Quantifying early marine diagenesis in shallow-water carbonate sediments. *Geochim. Cosmochim. Acta* 236, 140-159.
- Ahm, A.-S.C., Maloof, A.C., Macdonald, F.A., Hoffman, P.F., Bjerrum, C.J., Bold, U., Rose, C.V., Strauss, J.V. and Higgins, J.A. (2019) An early diagenetic deglacial origin for basal Ediacaran “cap dolostones”. *Earth Plan. Sci. Lett.* 506, 292-307.
- AlKhatib, M. and Eisenhauer, A. (2017a) Calcium and strontium isotope fractionation in aqueous solutions as a function of temperature and reaction rate; I. Calcite. *Geochim. Cosmochim. Acta* 209, 296-319.
- AlKhatib, M. and Eisenhauer, A. (2017b) Calcium and strontium isotope fractionation during precipitation from aqueous solutions as a function of temperature and reaction rate; II. Aragonite. *Geochim. Cosmochim. Acta* 209, 320-342.
- Allan, J. and Matthews, R. (1982) Isotope signatures associated with early meteoric diagenesis. *Sedimentology* 29, 797-817.
- Andrews, M.G. and Jacobson, A.D. (2017) The radiogenic and stable Sr isotope geochemistry of basalt weathering in Iceland: Role of hydrothermal calcite and implications for long-term climate regulation. *Geochim. Cosmochim. Acta* 215, 247-262.
- Andrews, M.G., Jacobson, A.D., Lehn, G.O., Horton, T.W. and Craw, D. (2016) Radiogenic and stable Sr isotope ratios ($^{87}\text{Sr}/^{86}\text{Sr}$, $\delta^{88/86}\text{Sr}$) as tracers of riverine cation sources and biogeochemical cycling in the Milford Sound region of Fiordland, New Zealand. *Geochim. Cosmochim. Acta* 173, 284-303.
- Bailey, T., McArthur, J., Prince, H. and Thirlwall, M. (2000) Dissolution methods for strontium isotope stratigraphy: whole rock analysis. *Chem. Geol.* 167, 313-319.
- Baker, P.A. and Kastner, M. (1981) Constraints on the formation of sedimentary dolomite. *Science* 213, 214-216.

- Baker, P.A., Gieskes, J.M. and Elderfield, H. (1982) Diagenesis of carbonates in deep-sea sediments; evidence from Sr/Ca ratios and interstitial dissolved Sr²⁺ data. *J Sediment Res* 52, 71-82.
- Bambach, R.K. (2006) Phanerozoic biodiversity mass extinctions. *Annu. Rev. Earth Planet. Sci.* 34, 127-155.
- Banner, J.L. and Hanson, G.N. (1990) Calculation of Simultaneous Isotopic and Trace-Element Variations during Water-Rock Interaction with Applications to Carbonate Diagenesis. *Geochim. Cosmochim. Acta* 54, 3123-3137.
- Banner, J.L. (1995) Application of the Trace-Element and Isotope Geochemistry of Strontium to Studies of Carbonate Diagenesis. *Sedimentology* 42, 805-824.
- Baresel, B., Bucher, H., Bagherpour, B., Brosse, M., Guodun, K. and Schaltegger, U. (2017) Timing of global regression and microbial bloom linked with the Permian-Triassic boundary mass extinction: implications for driving mechanisms. *Sci. Rep.* 7, 43630.
- Bathurst, R.G. (1972) *Carbonate sediments and their diagenesis*. Elsevier.
- Bayon, G., German, C., Boella, R., Milton, J., Taylor, R. and Nesbitt, R. (2002) An improved method for extracting marine sediment fractions and its application to Sr and Nd isotopic analysis. *Chem. Geol.* 187, 179-199.
- Berner, R.A., and Caldeira, K., 1997, The need for mass balance and feedback in the geochemical carbon cycle: *Geology*, v. 25, p. 955, doi:10.1130/0091-7613(1997)025<0955:TNFMBA>2.3.CO;2.
- Blättler, C.L., Jenkyns, H.C., Reynard, L.M. and Henderson, G.M. (2011) Significant increases in global weathering during Oceanic Anoxic Events 1a and 2 indicated by calcium isotopes. *Earth Plan. Sci. Lett.* 309, 77-88.
- Blättler, C.L., Henderson, G.M. and Jenkyns, H.C. (2012) Explaining the Phanerozoic Ca isotope history of seawater. *Geology* 40, 843-846.
- Blättler, C.L., Miller, N.R. and Higgins, J.A. (2015) Mg and Ca isotope signatures of authigenic dolomite in siliceous deep-sea sediments. *Earth Plan. Sci. Lett.* 419, 32-42.
- Blättler, C.L., and Higgins, J.A., (2017) Testing Urey's carbonate-silicate cycle using the calcium isotopic composition of sedimentary carbonates: *Earth and Planetary Science Letters*, v. 479, p. 241–251, doi:10.1016/j.epsl.2017.09.033.

Böhm, F., Eisenhauer, A., Tang, J., Dietzel, M., Krabbenhöft, A., Kiskakürek, B. and Horn, C. (2012) Strontium isotope fractionation of planktic foraminifera and inorganic calcite. *Geochim. Cosmochim. Acta* 93, 300-314.

Bottini, C., Cohen, A.S., Erba, E., Jenkyns, H.C., and Coe, A.L. (2012) Osmium-isotope evidence for volcanism, weathering, and ocean mixing during the early Aptian OAE 1a: *Geology*, v. 40, p. 583–586, doi:10.1130/G33140.1.

Boudreau, B.P., Middelburg, J.J., and Luo, Y., 2018, The role of calcification in carbonate compensation: *Nature Geoscience*, v. 11, p. 894–900, doi:10.1038/s41561-018-0259-5.

Bowring, S.A., Erwin, D., Jin, Y., Martin, M., Davidek, K. and Wang, W. (1998) U/Pb zircon geochronology and tempo of the end-Permian mass extinction. *Science* 280, 1039-1045.

Bradbury, H. J., & Turchyn, A. V. (2018). Calcium isotope fractionation in sedimentary pore fluids from ODP Leg 175: Resolving carbonate recrystallization. *Geochim. Cosmochim. Acta* 236, 121-139.

Brand, U. and Veizer, J. (1980) Chemical diagenesis of a multicomponent carbonate system; 1, Trace elements. *J. Sediment. Res.* 50, 1219-1236.

Brand, U. and Veizer, J. (1981) Chemical diagenesis of a multicomponent carbonate system; 2, Stable isotopes. *J. Sediment. Res.* 51, 987-997.

Brosse, M., Bucher, H. and Goudemand, N. (2016) Quantitative biochronology of the Permian–Triassic boundary in South China based on conodont unitary associations. *Earth-Sci. Rev.* 155, 153-171.

Burgess, S.D., Bowring, S. and Shen, S.Z. (2014) High-precision timeline for Earth's most severe extinction. *Proc. Nat. Acad. Sci. U.S.A.* 111, 3316-3321.

Burgess, S.D. and Bowring, S.A., (2015). High-precision geochronology confirms voluminous magmatism before, during, and after Earth's most severe extinction. *Science Advances*, 1(7), p.e1500470.

Burgess, S.D., Muirhead, J.D. and Bowring, S.A., (2017). Initial pulse of Siberian Traps sills as the trigger of the end-Permian mass extinction. *Nat. Commun.* 8(1), p.164.

Campbell, I., Czamanske, G., Fedorenko, V., Hill, R. and Stepanov, V. (1992) Synchronism of the Siberian Traps and the Permian-Triassic boundary. *Science* 258, 1760-1763.

Cao, C. and Zheng, Q. (2007) High-resolution lithostratigraphy of the Changhsingian stage in Meishan section D, Zhejiang. *J. of Strati.* 31, 14-22.

Cao, C. and Zheng, Q. (2009) Geological event sequences of the Permian-Triassic transition recorded in the microfacies in Meishan section. *Sci. in Chin. Ser. D: Earth Sci.* 52, 1529.

Chaudhuri, S. and Brookins, D.G. (1979) The Rb- Sr systematics in acid-leached clay minerals. *Chem. Geol.* 24, 231-242.

Chen, Z.-Q., Yang, H., Luo, M., Benton, M.J., Kaiho, K., Zhao, L., Huang, Y., Zhang, K., Fang, Y. and Jiang, H. (2015) Complete biotic and sedimentary records of the Permian–Triassic transition from Meishan section, South China: ecologically assessing mass extinction and its aftermath. *Earth-Sci. Rev.* 149, 67-107.

Clapham, M.E. and Payne, J.L. (2011) Acidification, anoxia, and extinction: A multiple logistic regression analysis of extinction selectivity during the Middle and Late Permian. *Geology* 39, 1059-1062.

Clapham, M. E., & Renne, P. R. (2019). Flood Basalts and Mass Extinctions. *Annu. Rev. Earth Planet. Sci.* 47.

Clauer, N., Chaudhuri, S., Kralik, M. and Bonnot-Courtois, C. (1993) Effects of experimental leaching on Rb-Sr and K-Ar isotopic systems and REE contents of diagenetic illite. *Chem. Geol.* 103, 1-16.

Corsetti, F.A., Baud, A., Marengo, P.J. and Richoz, S. (2005) Summary of Early Triassic carbon isotope records. *C. R. Palevol* 4, 473-486.

Creveling, J.R., and Mitrovica, J.X., 2014, The sea-level fingerprint of a Snowball Earth deglaciation: *Earth and Planetary Science Letters*, v. 399, p. 74–85, doi:10.1016/j.epsl.2014.04.029.

Cui, H., Kaufman, A.J., Xiao, S., Zhou, C. and Liu, X.-M. (2017) Was the Ediacaran Shuram Excursion a globally synchronized early diagenetic event? Insights from methane-derived authigenic carbonates in the uppermost Doushantuo Formation, South China. *Chem. Geol.* 450, 59-80.

Cui, Y., Kump, L.R. and Ridgwell, A. (2013) Initial assessment of the carbon emission rate and climatic consequences during the end-Permian mass extinction. *Palaeogeogr. Palaeoclimatol. Palaeoecol.* 389, 128-136.

Davis, A.C., Bickle, M.J. and Teagle, D.A. (2003) Imbalance in the oceanic strontium budget. *Earth Plan. Sci. Lett.* 211, 173-187.

De La Rocha, C.L. and DePaolo, D.J. (2000) Isotopic evidence for variations in the marine calcium cycle over the Cenozoic. *Science* 289, 1176-1178.

Deng, B., Wang, Y., Woods, A., Li, S., Li, G. and Chen, W. (2017) Evidence for rapid precipitation of calcium carbonate in South China at the beginning of Early Triassic. *Palaeogeogr. Palaeoclimatol. Palaeoecol.* 474, 187-197.

DePaolo, D.J. (2011) Surface kinetic model for isotopic and trace element fractionation during precipitation of calcite from aqueous solutions. *Geochim. Cosmochim. Acta* 75, 1039-1056.

Derry, L.A. (2010) A burial diagenesis origin for the Ediacaran Shuram–Wonoka carbon isotope anomaly. *Earth Plan. Sci. Lett.* 294, 152-162.

Dickson, J. and Coleman, M. (1980) Changes in carbon and oxygen isotope composition during limestone diagenesis. *Sedimentology* 27, 107-118.

Doney, S.C., Fabry, V.J., Feely, R.A. and Kleypas, J.A. (2009) Ocean acidification: the other CO₂ problem.

Du Vivier, A.D., Jacobson, A.D., Lehn, G.O., Selby, D., Hurtgen, M.T. and Sageman, B.B. (2015) Ca isotope stratigraphy across the Cenomanian–Turonian OAE 2: links between volcanism, seawater geochemistry, and the carbonate fractionation factor. *Earth Plan. Sci. Lett.* 416, 121-131.

Dudás, F.Ö., Yuan, D.-X., Shen, S.-Z. and Bowring, S.A. (2017) A conodont-based revision of the ⁸⁷Sr/⁸⁶Sr seawater curve across the Permian-Triassic boundary. *Palaeogeogr. Palaeoclimatol. Palaeoecol.* 470, 40-53.

Erba, E., and Tremolada, F., 2004, Nannofossil carbonate fluxes during the Early Cretaceous: Phytoplankton response to nutrification episodes, atmospheric CO₂, and anoxia. *Paleoceanography*, 19(1). doi:10.1029/2003pa000884.

Erba, E., Bottini, C., Weissert, H.J., and Keller, C.E., 2010, Calcareous Nannoplankton Response to Surface-Water Acidification Around Oceanic Anoxic Event 1a: *Science*, v. 329, p. 428–432, doi:10.1126/science.1188886.

Erwin, D. (1990) The end-Permian mass extinction. *Annu. Rev. Ecol. Evol. Syst.* 21, 69-91.

Erwin, D.H. (1994) The Permo–Triassic extinction. *Nature* 367, 231.

Erwin, D.H. (2015) *Extinction: How Life on Earth Nearly Ended 250 Million Years Ago-Updated Edition*. Princeton University Press.

Eugster, O., Tera, F. and Wasserburg, G. (1969) Isotopic analyses of barium in meteorites and in terrestrial samples. *J. Geophys. Res.* 74, 3897-3908.

Fabre, S., and Berger, G., 2012, How tillite weathering during the snowball Earth aftermath induced cap carbonate deposition: *Geology*, v. 40, p. 1027–1030, doi:10.1130/G33340.1.

Fantle, M.S. and DePaolo, D.J. (2005) Variations in the marine Ca cycle over the past 20 million years. *Earth Plan. Sci. Lett.* 237, 102-117.

Fantle, M.S. and DePaolo, D.J. (2007) Ca isotopes in carbonate sediment and pore fluid from ODP Site 807A: The $\text{Ca}^{2+}_{(\text{aq})}$ -calcite equilibrium fractionation factor and calcite recrystallization rates in Pleistocene sediments. *Geochim. Cosmochim. Acta* 71, 2524-2546.

Fantle, M.S. and Bullen, T.D. (2009) Essentials of iron, chromium, and calcium isotope analysis of natural materials by thermal ionization mass spectrometry. *Chem. Geol.* 258, 50-64.

Fantle, M., Maher, K. and DePaolo, D. (2010) Isotopic approaches for quantifying the rates of marine burial diagenesis. *Rev. Geophys.* 48, RG3002.

Fantle, M.S. (2010) Evaluating the Ca isotope proxy. *Am. J. Sci.* 310, 194-230.

Fantle, M.S. and Higgins, J. (2014) The effects of diagenesis and dolomitization on Ca and Mg isotopes in marine platform carbonates: Implications for the geochemical cycles of Ca and Mg. *Geochim. Cosmochim. Acta* 142, 458-481.

Fantle, M.S. and Tipper, E.T. (2014) Calcium isotopes in the global biogeochemical Ca cycle: Implications for development of a Ca isotope proxy. *Earth-Sci. Rev.* 129, 148-177.

Fantle, M.S. (2015) Calcium isotopic evidence for rapid recrystallization of bulk marine carbonates and implications for geochemical proxies. *Geochim. Cosmochim. Acta* 148, 378-401.

Farkaš, J., Böhm, F., Wallmann, K., Blenkinsop, J., Eisenhauer, A., Van Geldern, R., Munnecke, A., Voigt, S. and Veizer, J. (2007) Calcium isotope record of Phanerozoic oceans: Implications for chemical evolution of seawater and its causative mechanisms. *Geochim. Cosmochim. Acta* 71, 5117-5134.

Farkaš, J., Frýda, J. and Holmden, C. (2016) Calcium isotope constraints on the marine carbon cycle and CaCO_3 deposition during the late Silurian (Ludfordian) positive $\delta^{13}\text{C}$ excursion. *Earth Plan. Sci. Lett.* 451, 31-40.

Fietzke, J. and Eisenhauer, A. (2006) Determination of temperature-dependent stable strontium isotope ($^{88}\text{Sr}/^{86}\text{Sr}$) fractionation via bracketing standard MC-ICP-MS. *Geochem. Geophys. Geosyst.* 7. p.Q08009.

Finch, A.A. and Allison, N. (2007) Coordination of Sr and Mg in calcite and aragonite. *Mineral. Mag.* 71, 539-552.

Flügel, E. (2013) *Microfacies of carbonate rocks: analysis, interpretation and application.* Springer Science & Business Media.

Folk, R.L. (1965) Some aspects of recrystallization in ancient limestones. *S.E.P.M.*, Sp 13.

Forney, G.G. (1975) Permo-Triassic sea level change. *J. Geol.* 83, 773-779.

Fruchter, N., Eisenhauer, A., Dietzel, M., Fietzke, J., Böhm, F., Montagna, P., Stein, M., Lazar, B., Rodolfo-Metalpa, R. and Erez, J. (2016) $^{88}\text{Sr}/^{86}\text{Sr}$ fractionation in inorganic aragonite and in corals. *Geochim. Cosmochim. Acta* 178, 268-280.

Gammon, P., McKirdy, D. and Smith, H. (2012) The paragenetic history of a Marinoan cap carbonate. *Sediment. Geol.* 243, 1-16.

Gao, G. (1990) Geochemical and isotopic constraints on the diagenetic history of a massive stratal, late Cambrian (Royer) dolomite, Lower Arbuckle Group, Slick Hills, SW Oklahoma, USA. *Geochim. Cosmochim. Acta* 54, 1979-1989.

Graf, D.L. and Goldsmith, J.R. (1956) Some hydrothermal syntheses of dolomite and protodolomite. *J. Geol.* 64, 173-186.

Gregg, J.M., Howard, S.A. and Mazzullo, S.J. (1992) Early diagenetic recrystallization of Holocene (< 3000 years old) peritidal dolomites, Ambergris Cay, Belize. *Sedimentology* 39, 143-160.

Grice, K., Cao, C., Love, G.D., Böttcher, M.E., Twitchett, R.J., Grosjean, E., Summons, R.E., Turgeon, S.C., Dunning, W. and Jin, Y. (2005) Photic zone euxinia during the Permian-Triassic superanoxic event. *Science* 307, 706-709.

Grice, K., Nabbefeld, B. and Maslen, E. (2007) Source and significance of selected polycyclic aromatic hydrocarbons in sediments (Hovea-3 well, Perth Basin, Western Australia) spanning the Permian–Triassic boundary. *Org Geochem.* 38, 1795-1803.

Griffith, E.M., Fantle, M.S., Eisenhauer, A., Paytan, A. and Bullen, T.D. (2015) Effects of ocean acidification on the marine calcium isotope record at the Paleocene–Eocene Thermal Maximum. *Earth Plan. Sci. Lett.* 419, 81-92.

Grotzinger, J.P., and Knoll, A.H., 1995, Anomalous Carbonate Precipitates: Is the Precambrian the Key to the Permian? *Palaios*, v. 10, p. 578, doi:10.2307/3515096.

Gussone, N., Böhm, F., Eisenhauer, A., Dietzel, M., Heuser, A., Teichert, B.M.A., Reitner, J., Wörheide, G. and Dullo, W.-C. (2005) Calcium isotope fractionation in calcite and aragonite. *Geochim. Cosmochim. Acta* 69, 4485-4494.

Gussone, N. and Filipsson, H.L. (2010) Calcium isotope ratios in calcitic tests of benthic foraminifers. *Earth Plan. Sci. Lett.* 290, 108-117.

Gussone, N., Schmitt, A.-D., Heuser, A., Wombacher, F., Dietzel, M., Tipper, E., Schiller, M. and Bohm, F. (2016) Calcium stable isotope geochemistry. Springer.

Gussone, N. and Greifelt, T. (2019) Incorporation of Ca isotopes in carapaxes of marine ostracods. *Chem. Geol.*, 130-139.

Halicz, L., Segal, I., Fruchter, N., Stein, M. and Lazar, B. (2008) Strontium stable isotopes fractionate in the soil environments? *Earth Plan. Sci. Lett.* 272, 406-411.

Hallam, A. (1992) Phanerozoic sea level changes. Columbia University Press.

Halverson, G.P., Hoffman, P.F., Schrag, D.P., Maloof, A.C., and Rice, A.H.N., 2005, Toward a Neoproterozoic composite carbon-isotope record: *Bulletin of the Geological Society of America*, v. 117, p. 1181–1207, doi:10.1130/B25630.1.

Halverson, G.P., Dudás, F.Ö., Maloof, A.C., and Bowring, S.A., 2007, Evolution of the $^{87}\text{Sr}/^{86}\text{Sr}$ composition of Neoproterozoic seawater: *Palaeogeography, Palaeoclimatology, Palaeoecology*, v. 256, p. 103–129, doi:10.1016/j.palaeo.2007.02.028.

Halverson, G.P., Wade, B.P., Hurtgen, M.T., and Barovich, K.M., 2010, Neoproterozoic chemostratigraphy: *Precambrian Research*, v. 182, p. 337–350, doi:10.1016/j.precamres.2010.04.007.

Hanshaw, B.B., Back, W. and Deike, R.G. (1971) A geochemical hypothesis for dolomitization by ground water. *Econ. Geol.* 66, 710-724.

Haq, B.U. and Schutter, S.R. (2008) A chronology of Paleozoic sea level changes. *Science* 322, 64-68.

Haq, B.U., Hardenbol, J. and Vail, P.R. (1987) Chronology of fluctuating sea levels since the Triassic. *Science* 235, 1156-1167.

He, Y., Wang, Y., Zhu, C., Huang, S. and Li, S. (2017) Mass-independent and mass-dependent Ca isotopic compositions of thirteen geological reference materials measured by thermal ionisation mass spectrometry. *Geostand. Geoanal. Res.* 41, 283-302.

Heinemann, A., Fietzke, J., Eisenhauer, A. and Zumholz, K. (2008) Modification of Ca isotope and trace metal composition of the major matrices involved in shell formation of *Mytilus edulis*. *Geochem. Geophys. Geosyst.* 9.

Higgins, J.A. and Schrag, D.P. (2003) Aftermath of a snowball Earth. *Geochem. Geophys. Geosyst.* 4 (3).

Higgins, J.A., Blättler, C.L., Lundstrom, E.A., Santiago-Ramos, D.P., Akhtar, A.A., Crüger Ahm, A.S., Bialik, O., Holmden, C., Bradbury, H., Murray, S.T. and Swart, P.K. (2018) Mineralogy, early marine diagenesis, and the chemistry of shallow-water carbonate sediments. *Geochim. Cosmochim. Acta* 220, 512-534.

Hinojosa, J.L., Brown, S.T., Chen, J., DePaolo, D.J., Paytan, A., Shen, S.-Z. and Payne, J.L. (2012) Evidence for end-Permian ocean acidification from calcium isotopes in biogenic apatite. *Geology* 40, 743-746.

Hoffman, P.F. et al., 2017, Snowball Earth climate dynamics and Cryogenian geology-geobiology: *Science Advances*, v. 3, doi:10.1126/sciadv.1600983.

Hoffman, P.F., 2011, Glaciogenic and associated strata of the Otavi carbonate platform and foreslope, northern Namibia: Evidence for large base-level and glacioeustatic changes: *Geological Society Memoir*, v. 36, p. 195–209, doi:10.1144/M36.14.

Hoffman, P.F., and Li, Z.X., 2009, A palaeogeographic context for Neoproterozoic glaciation: *Palaeogeography, Palaeoclimatology, Palaeoecology*, v. 277, p. 158–172, doi:10.1016/j.palaeo.2009.03.013.

Hoffman, P.F., and Schrag, D.P., 2002, The snowball Earth hypothesis: testing the limits of global change: *Terra Nova*, v. 14, p. 129–155, doi:10.1046/j.1365-3121.2002.00408.x.

Hoffman, P.F., Halverson, G.P., Domack, E.W., Husson, J.M., Higgins, J.A., and Schrag, D.P., 2007, Are basal Ediacaran (635 Ma) post-glacial “cap dolostones” diachronous? *Earth and Planetary Science Letters*, v. 258, p. 114–131, doi:10.1016/j.epsl.2007.03.032.

Hoffman, P.F., Kaufman, A.J., Halverson, G.P., and Schrag, D.P., 1998, A neoproterozoic snowball earth: *Science*, v. 281, p. 1342–1346, doi:10.1126/science.281.5381.1342.

Holmden, C. and Bélanger, N. (2010) Ca isotope cycling in a forested ecosystem. *Geochim. Cosmochim. Acta* 74, 995-1015.

Holmden, C., Papanastassiou, D.A., Blanchon, P. and Evans, S. (2012) $\delta^{44/40}\text{Ca}$ variability in shallow water carbonates and the impact of submarine groundwater discharge on Ca-cycling in marine environments. *Geochim. Cosmochim. Acta* 83, 179-194.

Holser, W.T., and Magaritz, M. (1987) Events near the Permian-Triassic boundary. *Mod. Geol.*, v. 11, p. 155–180.

Holser, W.T., Schonlaub, H.P., Attrep, M., Boeckelmann, K., Klein, P., Magaritz, M., Orth, C.J., Fenninger, A., Jenny, C., Kralik, M., Mauritsch, H., Pak, E., Schramm, J.M., Statterger, K. and Schmoller, R. (1989) A Unique Geochemical Record at the Permian Triassic Boundary. *Nature* 337, 39-44.

Hönisch, B., Ridgwell, A., Schmidt, D.N., Thomas, E., Gibbs, S.J., Sluijs, A., Zeebe, R., Kump, L., Martindale, R.C. and Greene, S.E. (2012) The geological record of ocean acidification. *Science* 335, 1058-1063.

Hotinski, R.M., Bice, K.L., Kump, L.R., Najjar, R.G. and Arthur, M.A. (2001) Ocean stagnation and end-Permian anoxia. *Geology* 29, 7-10.

Hurtgen, M.T., Halverson, G.P., Arthur, M.A., and Hoffman, P.F., (2006) Sulfur cycling in the aftermath of a 635-Ma snowball glaciation: Evidence for a syn-glacial sulfidic deep ocean: *Earth and Planetary Science Letters*, v. 245, p. 551–570, doi:10.1016/j.epsl.2006.03.026.

Husson, J.M., Higgins, J.A., Maloof, A.C., and Schoene, B., (2015) Ca and Mg isotope constraints on the origin of Earth's deepest $\delta^{13}\text{C}$ excursion: *Geochimica et Cosmochimica Acta*, v. 160, p. 243–266, doi:10.1016/j.gca.2015.03.012.

Irie, Y., Nakada, M., Okuno, J., and Bao, H., (2019) Nonmonotonic Postdeglacial Relative Sea Level Changes at the Aftermath of Marinoan (635 Ma) Snowball Earth Meltdown: *Journal of Geophysical Research: Solid Earth*, v. 124, p. 9373–9394, doi:10.1029/2018JB017260.

Jacobson, A.D. and Holmden, C. (2008) $\delta^{44}\text{Ca}$ evolution in a carbonate aquifer and its bearing on the equilibrium isotope fractionation factor for calcite. *Earth Plan. Sci. Lett.* 270, 349-353.

James, N.P., Narbonne, G.M., and Kyser, T.K., 2001, Late Neoproterozoic cap carbonates: Mackenzie Mountains, northwestern Canada: Precipitation and global glacial meltdown: *Canadian Journal of Earth Sciences*, v. 38, p. 1229–1262, doi:10.1139/e01-046.

Jenkyns, H.C., and Strasser, A., 1995, Lower Cretaceous oolites from the Mid-Pacific Mountains (Resolution Guyot, Site 866): *Proc., scientific results, ODP, Leg 143, northwest Pacific atolls and guyots*, p. 111–118, doi:10.2973/odp.proc.sr.143.211.1995.

Jenkyns, H.C., and Wilson, P.A., 1999, Stratigraphy, paleoceanography, and evolution of Cretaceous Pacific guyots: Relics from a greenhouse Earth: *American Journal of Science*, v. 299, p. 341–392, doi:10.2475/ajs.299.5.341.

Jiang, H., Lai, X., Sun, Y., Wignall, P.B., Liu, J. and Yan, C. (2014) Permian-Triassic conodonts from Dajiang (Guizhou, South China) and their implication for the age of microbialite deposition in the aftermath of the End-Permian mass extinction. *J Earth Sci.* 25, 413-430.

Jin, Y. G., Wang, Y., Wang, W., Shang, Q. H., Cao, C. Q., and Erwin, D. H. (2000). Pattern of marine mass extinction near the Permian-Triassic boundary in South China. *Science*, 289(5478), 432-436.

Jost, A.B., Bachan, A., van de Schootbrugge, B., Brown, S.T., DePaolo, D.J. and Payne, J.L. (2017) Additive effects of acidification and mineralogy on calcium isotopes in Triassic/Jurassic boundary limestones. *Geochem. Geophys. Geosyst.* 18, 113-124.

Kasemann, S.A., Hawkesworth, C.J., Prave, A.R., Fallick, A.E., and Pearson, P.N., (2005) Boron and calcium isotope composition in Neoproterozoic carbonate rocks from Namibia: Evidence for extreme environmental change: *Earth and Planetary Science Letters*, v. 231, p. 73–86, doi:10.1016/j.epsl.2004.12.006.

Kasemann, S.A., Prave, A.R., Fallick, A.E., Hawkesworth, C.J., and Hoffmann, K.H., (2010) Neoproterozoic ice ages, boron isotopes, and ocean acidification: Implications for a snowball Earth: *Geology*, v. 38, p. 775–778, doi:10.1130/G30851.1.

Kasemann, S.A., Pogge von Strandmann, P.A.E., Prave, A.R., Fallick, A.E., Elliott, T., and Hoffmann, K.H., (2014) Continental weathering following a Cryogenian glaciation: Evidence from calcium and magnesium isotopes: *Earth and Planetary Science Letters*, v. 396, p. 66–77, doi:10.1016/j.epsl.2014.03.048.

Kennedy, M.J., (1996) Stratigraphy, sedimentology, and isotopic geochemistry of Australian Neoproterozoic postglacial cap dolostones; deglaciation, delta 13 C excursions, and carbonate precipitation: *Journal of Sedimentary Research*, v. 66, p. 1050–1064, doi:10.2110/jsr.66.1050.

Kennedy, M.J., Christie-Blick, N., and Sohl, L.E., (2001) Are Proterozoic cap carbonates and isotopic excursions a record of gas hydrate destabilization following Earth's coldest intervals? *Geology*, v. 29, p. 443–446, doi:10.1130/0091-7613(2001)029<0443:APCCAI>2.0.CO;2.

Kennedy, M.J., and Christie-Blick, N., (2011) Condensation origin for Neoproterozoic cap carbonates during deglaciation: *Geology*, v. 39, p. 319–322, doi:10.1130/G31348.1.

Kershaw, S., Zhang, T. and Lan, G. (1999) A microbialite carbonate crust at the Permian–Triassic boundary in South China, and its palaeoenvironmental significance. *Palaeogeogr. Palaeoclimatol. Palaeoecol.* 146, 1-18.

Kershaw, S., Crasquin, S., Li, Y., Collin, P.Y., Forel, M.B., Mu, X., Baud, A., Wang, Y., Xie, S. and Maurer, F. (2012) Microbialites and global environmental change across the Permian–Triassic boundary: a synthesis. *Geobiology* 10, 25-47.

Kimmig, S.R. and Holmden, C. (2017) Multi-proxy geochemical evidence for primary aragonite precipitation in a tropical-shelf ‘calcite sea’ during the Hirnantian glaciation. *Geochim. Cosmochim. Acta* 206, 254-272.

Kinsman, D.J. (1969) Interpretation of Sr^{2+} concentrations in carbonate minerals and rocks. *J. Sediment. Res.* 39, 486-508.

Kısakürek, B., Eisenhauer, A., Böhm, F., Hathorne, E.C. and Erez, J. (2011) Controls on calcium isotope fractionation in cultured planktic foraminifera, *Globigerinoides ruber* and *Globigerinella siphonifera*. *Geochim. Cosmochim. Acta* 75, 427-443.

Knoll, A.H., Bambach, R., Canfield, D. and Grotzinger, J. (1996) Comparative Earth history and Late Permian mass extinction. *Science* 273, 452-457.

Knoll, A.H., Bambach, R.K., Payne, J.L., Pruss, S. and Fischer, W.W. (2007) Paleophysiology and end-Permian mass extinction. *Earth Plan. Sci. Lett.* 256, 295-313.

Komar, N. and Zeebe, R.E. (2016) Calcium and calcium isotope changes during carbon cycle perturbations at the end-Permian. *Paleoceanography* 31, 115-130.

Korte, C. and Kozur, H.W. (2010) Carbon-isotope stratigraphy across the Permian–Triassic boundary: A review. *J Asian Earth Sci.* 39, 215-235.

Krabbenhöft, A., Fietzke, J., Eisenhauer, A., Liebetrau, V., Böhm, F. and Vollstaedt, H. (2009) Determination of radiogenic and stable strontium isotope ratios ($^{87}\text{Sr}/^{86}\text{Sr}$; $\delta^{88/86}\text{Sr}$) by thermal ionization mass spectrometry applying an $^{87}\text{Sr}/^{84}\text{Sr}$ double spike. *J. Anal. At. Spectrom.* 24, 1267-1271.

Krabbenhöft, A., Eisenhauer, A., Böhm, F., Vollstaedt, H., Fietzke, J., Liebetrau, V., Augustin, N., Peucker-Ehrenbrink, B., Müller, M. and Horn, C. (2010) Constraining the marine strontium budget with natural strontium isotope fractionations ($^{87}\text{Sr}/^{86}\text{Sr}^*$, $\delta^{88/86}\text{Sr}$) of carbonates, hydrothermal solutions and river waters. *Geochim. Cosmochim. Acta* 74, 4097-4109.

Krull, E.S. and Retallack, G.J. (2000) $\delta^{13}\text{C}$ depth profiles from paleosols across the Permian-Triassic boundary: Evidence for methane release. *Geol. Soc. Am. Bull.* 112, 1459-1472.

Kump, L.R. (1989) Alternative modeling approaches to the geochemical cycles of carbon, sulfur, and strontium isotopes. *Am. J. Sci.* 289, 390-410.

Kump, L.R., Bralower, T.J. and Ridgwell, A. (2009) Ocean acidification in deep time. *Oceanography* 22, 94-107.

Kump, L.R. (2018) Prolonged Late Permian–Early Triassic hyperthermal: failure of climate regulation? *Philosophical Transactions of the Royal Society A: Mathematical, Physical and Engineering Sciences* 376, 20170078.

Lau, K.V., Maher, K., Brown, S.T., Jost, A.B., Altner, D., DePaolo, D.J., Eisenhauer, A., Kelley, B.M., Lehrmann, D.J., Paytan, A., Yu, M., Silva-Tamayo, J.C. and Payne, J.L. (2017) The influence of seawater carbonate chemistry, mineralogy, and diagenesis on calcium isotope variations in Lower-Middle Triassic carbonate rocks. *Chem. Geol.* 471, 13-37.

Lechler, M., Pogge von Strandmann, P.A.E., Jenkyns, H.C., Prosser, G., and Parente, M., (2015) Lithium-isotope evidence for enhanced silicate weathering during OAE 1a (Early Aptian Selli event): *Earth and Planetary Science Letters*, v. 432, p. 210–222, doi:10.1016/j.epsl.2015.09.052.

Lehn, G.O. and Jacobson, A.D. (2015) Optimization of a ^{48}Ca – ^{43}Ca double-spike MC-TIMS method for measuring Ca isotope ratios ($\delta^{44/40}\text{Ca}$ and $\delta^{44/42}\text{Ca}$): limitations from filament reservoir mixing. *J. Anal. At. Spectrom.* 30, 1571-1581.

Lehn, G.O., Jacobson, A.D. and Holmden, C. (2013) Precise analysis of Ca isotope ratios ($\delta^{44/40}\text{Ca}$) using an optimized ^{43}Ca – ^{42}Ca double-spike MC-TIMS method. *International J. Mass Spectrom.* 351, 69-75.

Lehrmann, D.J., Payne, J.L., Felix, S.V., Dillett, P.M., Wang, H., Yu, Y. and Wei, J. (2003) Permian–Triassic boundary sections from shallow-marine carbonate platforms of the Nanpanjiang Basin, South China: implications for oceanic conditions associated with the end-Permian extinction and its aftermath. *Palaios* 18, 138-152.

Lehrmann, D.J., Payne, J.L., Pei, D., Enos, P., Druke, D., Steffen, K., Zhang, J., Wei, J., Orchard, M.J. and Ellwood, B. (2007) Record of the end-Permian extinction and Triassic biotic recovery in

the Chongzuo-Pingguo platform, southern Nanpanjiang basin, Guangxi, south China. *Palaeogeogr. Palaeoclimatol. Palaeoecol.* 252, 200-217.

Lehrmann, D.J., Bentz, J.M., Wood, T., Goers, A., Dhillon, R., Akin, S., Li, X., Payne, J.L., Kelley, B.M., Meyer, K.M., Schaal, E.K., Suarez, M.B., Yu, M., Qin, Y., Li, R., Minzoni, M. and Henderson, C.M. (2015) Environmental Controls on the Genesis of Marine Microbialites and Dissolution Surface Associated with the End-Permian Mass Extinction: New sections and Observations from the Nanpanjiang Basin, South China. *Palaios* 30, 529-552.

Li, R. and Jones, B. (2017) Diagenetic overprint on negative $\delta^{13}\text{C}$ excursions across the Permian/Triassic boundary: A case study from Meishan section, China. *Palaeogeogr. Palaeoclimatol. Palaeoecol.* 468, 18-33.

Linzmeier, B.J., Jacobson, A.D., Sageman, B.B., Hurtgen, M.T., Ankney, M.E., Petersen, S. V., Tobin, T.S., Kitch, G.D., and Wang, J., (2020) Calcium isotope evidence for environmental variability before and across the Cretaceous-Paleogene mass extinction: *Geology*, v. 48, p. 34–38, doi:10.1130/G46431.1.

Liu, C., Wang, Z. and Raub, T.D. (2013) Geochemical constraints on the origin of Marinoan cap dolostones from Nuccaleena Formation, South Australia. *Chem. Geol.* 351, 95-104.

Liu, C., Wang, Z., Raub, T.D., Macdonald, F.A., and Evans, D.A.D., (2014) Neoproterozoic cap-dolostone deposition in stratified glacial meltwater plume: *Earth and Planetary Science Letters*, v. 404, p. 22–32, doi:10.1016/j.epsl.2014.06.039.

Liu, C., Wang, Z. and Macdonald, F.A. (2018) Sr and Mg isotope geochemistry of the basal Ediacaran cap limestone sequence of Mongolia: Implications for carbonate diagenesis, mixing of glacial meltwaters, and seawater chemistry in the aftermath of Snowball Earth. *Chem. Geol.* 491, 1-13.

Lohmann, K.C. (1988) Geochemical patterns of meteoric diagenetic systems and their application to studies of paleokarst, *Paleokarst*. Springer, pp. 58-80.

McNutt, R.H., Frappe, S.K., Fritz, P., Jones, M.G. and MacDonald, I.M. (1990) The $^{87}\text{Sr}/^{86}\text{Sr}$ values of Canadian Shield brines and fracture minerals with applications to groundwater mixing, fracture history, and geochronology. *Geochim. Cosmochim. Acta* 54, 205-215.

Mejía, L.M., Paytan, A., Eisenhauer, A., Böhm, F., Kolevica, A., Bolton, C., Méndez-Vicente, A., Abrevaya, L., Isensee, K. and Stoll, H. (2018) Controls over $\delta^{44/40}\text{Ca}$ and Sr/Ca variations in coccoliths: New perspectives from laboratory cultures and cellular models. *Earth Plan. Sci. Lett.* 481, 48-60.

Melin, A.D., Crowley, B.E., Brown, S.T., Wheatley, P.V., Moritz, G.L., Yit Yu, F.T., Bernard, H., DePaolo, D.J., Jacobson, A.D. and Dominy, N.J. (2014) Calcium and carbon stable isotope ratios as paleodietary indicators. *Am. J. Phys. Anthropol.*, 154(4), pp.633-643

Meyer, K., Kump, L. and Ridgwell, A. (2008) Biogeochemical controls on photic-zone euxinia during the end-Permian mass extinction. *Geology* 36, 747-750.

Mills, J. V., Gomes, M. L., Kristall, B., Sageman, B. B., Jacobson, A. D., and Hurtgen, M. T., (2017) Massive volcanism, evaporite deposition, and the chemical evolution of the Early Cretaceous ocean. *Geology*, 45(5), 475–478. doi:10.1130/G38667.1

Mondal, S. and Chakrabarti, R. (2018) A novel sample loading method and protocol for monitoring sample fractionation for high precision Ca stable isotope ratio measurements using double-spike TIMS. *J. Anal. At. Spectrom.* 33, 141-150.

Moore, C.H. (1989) Carbonate diagenesis and porosity. Elsevier.

Müller, M.N., Krabbenhöft, A., Vollstaedt, H., Brandini, F. and Eisenhauer, A. (2018) Stable isotope fractionation of strontium in coccolithophore calcite: Influence of temperature and carbonate chemistry. *Geobiology* 16, 297-306.

Naafs, B.D.A., Castro, J.M., De Gea, G.A., Quijano, M.L., Schmidt, D.N., and Pancost, R.D., 2016, Gradual and sustained carbon dioxide release during Aptian Oceanic Anoxic Event 1a: *Nature Geoscience*, v. 9, p. 135–139, doi:10.1038/ngeo2627.

Nielsen, L.C., DePaolo, D.J. and De Yoreo, J.J. (2012) Self-consistent ion-by-ion growth model for kinetic isotopic fractionation during calcite precipitation. *Geochim. Cosmochim. Acta* 86, 166-181.

Ohr, M., Halliday, A.N. and Peacor, D.R. (1991) Sr and Nd isotopic evidence for punctuated clay diagenesis, Texas Gulf Coast. *Earth Plan. Sci. Lett.* 105, 110-126.

Opdyke, B.N. and Wilkinson, B.H. (1993) Carbonate mineral saturation state and cratonic limestone accumulation. *Am. J. Sci.* 293, 217-234.

Paquette, J. and Reeder, R.J. (1995) Relationship between surface structure, growth mechanism, and trace element incorporation in calcite. *Geochim. Cosmochim. Acta* 59, 735-749.

Paull, C.K., Fullagar, P.D., Bralower, T.J., and Rohl, U., (1995) Seawater ventilation of mid-Pacific guyots drilled during Leg 143: Proc., scientific results, ODP, Leg 143, northwest Pacific atolls and guyots, v. 143, p. 231–241, doi:10.2973/odp.proc.sr.143.222.1995.

Payne, J.L., Lehrmann, D.J., Wei, J. and Knoll, A.H. (2006) The pattern and timing of biotic recovery from the end-Permian extinction on the Great Bank of Guizhou, Guizhou Province, China. *Palaeos* 21, 63-85.

Payne, J.L. and Kump, L.R. (2007) Evidence for recurrent Early Triassic massive volcanism from quantitative interpretation of carbon isotope fluctuations. *Earth Plan. Sci. Lett.* 256, 264-277.

Payne, J.L. and Clapham, M.E. (2012) End-Permian Mass Extinction in the Oceans: An Ancient
Payne, J.L., Turchyn, A.V., Paytan, A., Depaolo, D.J., Lehrmann, D.J., Yu, M. and Wei, J. (2010) Calcium isotope constraints on the end-Permian mass extinction. *Proc. Nat. Acad. Sci. U.S.A.* 107, 8543-8548.

Analog for the Twenty-First Century? *Annu. Rev. Earth Planet. Sci.* 40, 89-111.

Pearce, C.R., Parkinson, I.J., Gaillardet, J., Charlier, B.L., Mokadem, F. and Burton, K.W. (2015) Reassessing the stable ($\delta^{88/86}\text{Sr}$) and radiogenic ($^{87}\text{Sr}/^{86}\text{Sr}$) strontium isotopic composition of marine inputs. *Geochim. Cosmochim. Acta* 157, 125-146.

Penman, D.E., Kirtland-Turner, S., Sexton, P.F., Norris, R.D. and Dickson, A.J. An abyssal carbonate compensation depth overshoot in the aftermath of the Palaeocene–Eocene Thermal Maximum. *Nat. Geosc.* 9, 575–580.

Peters, S.E. and Husson, J.M. (2017) Sediment cycling on continental and oceanic crust. *Geology* 45, 323-326.

Pierrehumbert, R.T., Abbot, D.S., Voigt, A., and Koll, D., 2011, Climate of the Neoproterozoic: Annual Review of Earth and Planetary Sciences, v. 39, p. 417–460, doi:10.1146/annurev-earth-040809-152447.

Pingitore, N.E., Lytle, F.W., Davies, B.M., Eastman, M.P., Eller, P.G., and Larson, E.M., 1992, Mode of incorporation of Sr^{2+} in calcite: Determination by X-ray absorption spectroscopy: *Geochimica et Cosmochimica Acta*, v. 56, p. 1531–1538, doi:10.1016/0016-7037(92)90222-5.

Pomar, L. and Hallock, P. (2008) Carbonate factories: a conundrum in sedimentary geology. *Earth-Sci. Rev.* 87, 134-169.

Pruss, S.B., Blättler, C.L., Macdonald, F.A. and Higgins, J.A. (2018) Calcium isotope evidence that the earliest metazoan biomineralizers formed aragonite shells. *Geology* 46, 763-766.

Raddatz, J., Liebetrau, V., Rüggeberg, A., Hathorne, E., Krabbenhöft, A., Eisenhauer, A., Böhm, F., Vollstaedt, H., Fietzke, J. and Correa, M.L. (2013) Stable Sr-isotope, Sr/Ca, Mg/Ca, Li/Ca and Mg/Li ratios in the scleractinian cold-water coral *Lophelia pertusa*. *Chem. Geol.* 352, 143-152.

Rampino, M.R. and Caldeira, K. (2005) Major perturbation of ocean chemistry and a 'Strangelove Ocean' after the end-Permian mass extinction. *Terra Nova* 17, 554-559.

Rampino, M.R., Caldeira, K., and Prokoph, A., (2019) What causes mass extinctions? Large asteroid/comet impacts, flood-basalt volcanism, and ocean anoxia - Correlations and cycles (C. Koeberl and D. M. Bice, Eds.): *250 Million Years of Earth History in Central Italy: Celebrating 25 Years of the Geological Observatory of Coldigioco*, v. 542, p. 0, doi:10.1130/2019.2542(14).

Rampino, M.R., Caldeira, K., and Prokoph, A., 2019, What causes mass extinctions? Large asteroid/comet impacts, flood-basalt volcanism, and ocean anoxia - Correlations and cycles (C. Koeberl and D. M. Bice, Eds.): *250 Million Years of Earth History in Central Italy: Celebrating 25 Years of the Geological Observatory of Coldigioco*, v. 542, p. 0, doi:10.1130/2019.2542(14).

Reinhardt, J.W. (1988) Uppermost Permian reefs and Permo-Triassic sedimentary facies from the southeastern margin of Sichuan Basin, China. *Facies* 18, 231-287.

Retallack, G.J., Veevers, J.J. and Morante, R. (1996) Global coal gap between Permian–Triassic extinction and Middle Triassic recovery of peat-forming plants. *Geol. Soc. Am. Bull.* 108, 195-207.

Retallack, G.J. and Jahren, A.H. (2008) Methane release from igneous intrusion of coal during Late Permian extinction events. *J. Geol.* 116, 1-20.

Riccardi, A., Kump, L.R., Arthur, M.A. and D'Hondt, S. (2007) Carbon isotopic evidence for chemocline upward excursions during the end-Permian event. *Palaeogeogr. Palaeoclimatol. Palaeoecol.* 248, 73-81.

Richter, F.M., and DePaolo, D.J., 1988, Diagenesis and Sr isotopic evolution of seawater using data from DSDP 590B and 575: *Earth and Planetary Science Letters*, v. 90, p. 382–394, doi:10.1016/0012-821X(88)90137-9.

Richter, F.M., and Liang, Y., 1993, The rate and consequences of Sr diagenesis in deep-sea carbonates: *Earth and Planetary Science Letters*, v. 117, p. 553–565, doi:10.1016/0012-821X(93)90102-F.

Romanek, C.S., Grossman, E.L. and Morse, J.W. (1992) Carbon isotopic fractionation in synthetic aragonite and calcite: effects of temperature and precipitation rate. *Geochim. Cosmochim. Acta* 56, 419-430.

Sandberg, P. A. (1983). An oscillating trend in Phanerozoic non-skeletal carbonate mineralogy. *Nature*, 305(5929), 19.

Sawaki, Y., Ohno, T., Tahata, M., Komiya, T., Hirata, T., Maruyama, S., Windley, B.F., Han, J., Shu, D., and Li, Y., 2010, The Ediacaran radiogenic Sr isotope excursion in the Doushantuo Formation in the Three Gorges area, South China: *Precambrian Research*, v. 176, p. 46–64, doi:10.1016/j.precamres.2009.10.006.

Schmitt, A.-D., Chabaux, F. and Stille, P. (2003) The calcium riverine and hydrothermal isotopic fluxes and the oceanic calcium mass balance. *Earth Plan. Sci. Lett.* 213, 503-518.

Scholle, P.A., Bebout, D.G. and Moore, C.H. (1983) *Carbonate Depositional Environments: AAPG Memoir 33. AAPG.*

Schobben, M., Stebbins, A., Ghaderi, A., Strauss, H., Korn, D. and Korte, C. (2015) Flourishing ocean drives the end-Permian marine mass extinction. *Proc. Nat. Acad. Sci. U.S.A.* 112, 10298-10303.

Schubert, J.K. and Bottjer, D.J. (1995) Aftermath of the Permian-Triassic mass extinction event: Paleoecology of Lower Triassic carbonates in the western USA. *Palaeogeogr. Palaeoclimatol. Palaeoecol.* 116, 1-39.

Sedlacek, A. R., Saltzman, M. R., Algeo, T. J., Horacek, M., Brandner, R., Foland, K., & Denniston, R. F. (2014). $^{87}\text{Sr}/^{86}\text{Sr}$ stratigraphy from the Early Triassic of Zal, Iran: Linking temperature to weathering rates and the tempo of ecosystem recovery. *Geology*, 42(9), 779-782.

Shao, Y., Farkaš, J., Holmden, C., Mosley, L., Kell-Duivesteyn, I., Izzo, C., Reis-Santos, P., Tyler, J., Törber, P. and Frýda, J. (2018) Calcium and strontium isotope systematics in the lagoon-estuarine environments of South Australia: Implications for water source mixing, carbonate fluxes and fish migration. *Geochim. Cosmochim. Acta* 239, 90-108.

Shen, J., Algeo, T.J., Hu, Q., Zhang, N., Zhou, L., Xia, W., Xie, S. and Feng, Q. (2012) Negative C-isotope excursions at the Permian-Triassic boundary linked to volcanism. *Geology* 40, 963-966.

Shen, S. Z., Ramezani, J., Chen, J., Cao, C. Q., Erwin, D. H., Zhang, H., Xiang, L., Schoepfer, S. D., Henderson, C. M., Zheng, Q. F., Bowring, S. A., Wang, Y., Li, X. H., Wang, X. D., Yuan, D. X., Zhang, Y. C., Mu, L., Wang, J., and Wu, Y. S. (2019) A sudden end-Permian mass extinction in South China: *Geol. Soc. Am. Bull.* 131, 205-223.

Shen, S.Z., Crowley, J.L., Wang, Y., Bowring, S.A., Erwin, D.H., Sadler, P.M., Cao, C.Q., Rothman, D.H., Henderson, C.M., Ramezani, J., Zhang, H., Shen, Y., Wang, X.D., Wang, W., Mu, L., Li, W.Z., Tang, Y.G., Liu, X.L., Liu, L.J., Zeng, Y., Jiang, Y.F. and Jin, Y.G. (2011) Calibrating the end-Permian mass extinction. *Science* 334, 1367-1372.

Shen, W., Lin, Y., Xu, L., Li, J., Wu, Y. and Sun, Y. (2007) Pyrite framboids in the Permian–Triassic boundary section at Meishan, China: evidence for dysoxic deposition. *Palaeogeogr. Palaeoclimatol. Palaeoecol.* 253, 323–331.

Shields, G.A., 2005, Neoproterozoic cap carbonates: A critical appraisal of existing models and the plumeworld hypothesis: *Terra Nova*, v. 17, p. 299–310, doi:10.1111/j.1365-3121.2005.00638.x.

Silva-Tamayo, J.C., Nägler, T.F., Sial, A.N., Nogueira, A., Kyser, K., Riccomini, C., James, N.P., Narbonne, G.M., and Villa, I.M., 2010, Global perturbation of the marine Ca isotopic composition in the aftermath of the Marinoan global glaciation: *Precambrian Research*, v. 182, p. 373–381, doi:10.1016/j.precamres.2010.06.015.

Silva-Tamayo, J.C., Lau, K.V., Jost, A.B., Payne, J.L., Wignall, P.B., Newton, R.J., Eisenhauer, A., Depaolo, D.J., Brown, S., Maher, K., Lehrmann, D.J., Altiner, D., Yu, M., Richoz, S. and Paytan, A. (2018) Global perturbation of the marine calcium cycle during the Permian-Triassic transition. *Geol. Soc. Am. Bull.* 130, 1323–1338.

Sime, N.G., De La Rocha, C.L., Tipper, E.T., Tripathi, A., Galy, A. and Bickle, M.J. (2007) Interpreting the Ca isotope record of marine biogenic carbonates. *Geochim. Cosmochim. Acta* 71, 3979–3989.

Sobolev, S.V., Sobolev, A.V., Kuzmin, D.V., Krivolutsкая, N.A., Petrunin, A.G., Arndt, N.T., Radko, V.A. and Vasiliev, Y.R. (2011) Linking mantle plumes, large igneous provinces and environmental catastrophes. *Nature* 477, 312.

Song, H., Tong, J., Chen, Z., Yang, H. and Wang, Y. (2009) End-Permian mass extinction of foraminifers in the Nanpanjiang Basin, South China. *J. Paleontol.* 83, 718–738.

Song, H., Tong, J., Xiong, Y., Sun, D., Tian, L. and Song, H. (2012) The large increase of $\delta^{13}\text{C}_{\text{carb}}$ -depth gradient and the end-Permian mass extinction. *Sci. China Earth Sci.* 55, 1101–1109.

Song, H., Wignall, P. B., Tong, J., & Yin, H. (2013). Two pulses of extinction during the Permian–Triassic crisis. *Nature Geoscience*, 6(1), 52.

Song, H., Wignall, P.B., Tong, J., Song, H., Chen, J., Chu, D., Tian, L., Luo, M., Zong, K., Chen, Y., Lai, X., Zhang, K. and Wang, H. (2015) Integrated Sr isotope variations and global environmental changes through the Late Permian to early Late Triassic. *Earth Plan. Sci. Lett.* 424, 140–147.

Stevenson, E.I., Hermoso, M., Rickaby, R.E., Tyler, J.J., Minoletti, F., Parkinson, I.J., Mokadem, F. and Burton, K.W. (2014) Controls on stable strontium isotope fractionation in coccolithophores with implications for the marine Sr cycle. *Geochim. Cosmochim. Acta* 128, 225-235.

Stewart, B.W., Chapman, E.C., Capo, R.C., Johnson, J.D., Graney, J.R., Kirby, C.S. and Schroeder, K.T. (2015) Origin of brines, salts and carbonate from shales of the Marcellus Formation: Evidence from geochemical and Sr isotope study of sequentially extracted fluids. *Appl. Geochem.* 60, 78-88.

Stoll, H.M. and Schrag, D.P. (1998) Effects of Quaternary sea level cycles on strontium in seawater. *Geochim. Cosmochim. Acta* 62, 1107-1118.

Strauss, J. V., and Tosca, N.J., 2020, Mineralogical constraints on Neoproterozoic pCO₂ and marine carbonate chemistry: *Geology*, v. 48, p. 599–603, doi:10.1130/G47506.1.

Stueber, A.M., Pushkar, P. and Hetherington, E.A. (1984) A strontium isotopic study of Smackover brines and associated solids, southern Arkansas. *Geochim. Cosmochim. Acta* 48, 1637-1649.

Stueber, A.M., Pushkar, P. and Hetherington, E.A. (1987) A strontium isotopic study of formation waters from the Illinois basin, USA. *Appl. Geochem.* 2, 477-494.

Sun, Y., Joachimski, M.M., Wignall, P.B., Yan, C., Chen, Y., Jiang, H., Wang, L. and Lai, X. (2012) Lethally hot temperatures during the Early Triassic greenhouse. *Science* 338, 366-370.

Svensen, H., Planke, S., Polozov, A.G., Schmidbauer, N., Corfu, F., Podladchikov, Y.Y. and Jamtveit, B. (2009) Siberian gas venting and the end-Permian environmental crisis. *Earth Plan. Sci. Lett.* 277, 490-500.

Swart, P.K. (2008) Global synchronous changes in the carbon isotopic composition of carbonate sediments unrelated to changes in the global carbon cycle. *Proc. Nat. Acad. Sci. U.S.A.* 105, 13741-13745.

Swart, P.K. (2015) The geochemistry of carbonate diagenesis: The past, present and future. *Sedimentology* 62, 1233-1304.

Tang, J., Dietzel, M., Böhm, F., Köhler, S.J., and Eisenhauer, A., 2008, Sr²⁺/Ca²⁺ and ⁴⁴Ca/⁴⁰Ca fractionation during inorganic calcite formation: II. Ca isotopes: *Geochimica et Cosmochimica Acta*, v. 72, p. 3733–3745, doi:10.1016/j.gca.2008.05.033.

Tang, J., Dietzel, M., Böhm, F., Köhler, S.J., and Eisenhauer, A., 2008, Sr²⁺/Ca²⁺ and ⁴⁴Ca/⁴⁰Ca fractionation during inorganic calcite formation: II. Ca isotopes: *Geochimica et Cosmochimica Acta*, v. 72, p. 3733–

3745, doi:10.1016/j.gca.2008.05.033.

Tang, J., Köhler, S.J. and Dietzel, M. (2008) Sr²⁺/Ca²⁺ and ⁴⁴Ca/⁴⁰Ca fractionation during inorganic calcite formation: I. Sr incorporation. *Geochim. Cosmochim. Acta* 72, 3718-3732.

Tejada, M.L.G., Suzuki, K., Kuroda, J., Coccioni, R., Mahoney, J.J., Ohkouchi, N., Sakamoto, T. and Tatsumi, Y., (2009) Ontong Java Plateau eruption as a trigger for the early Aptian oceanic anoxic event. *Geology*, 37(9), pp.855-858. doi: 10.1130/G25763A.1.

Tian, L., Tong, J., Bottjer, D., Chu, D., Liang, L., Song, H. and Song, H. (2015) Rapid carbonate depositional changes following the Permian-Triassic mass extinction: Sedimentary evidence from South China. *J Earth Sci.* 26, 166-180.

Turchyn, A.V. and DePaolo, D.J. (2011) Calcium isotope evidence for suppression of carbonate dissolution in carbonate-bearing organic-rich sediments. *Geochim. Cosmochim. Acta* 75, 7081-7098.

Voigt, J., Hathorne, E.C., Frank, M., Vollstaedt, H. and Eisenhauer, A. (2015) Variability of carbonate diagenesis in equatorial Pacific sediments deduced from radiogenic and stable Sr isotopes. *Geochim. Cosmochim. Acta* 148, 360-377.

Vollstaedt, H., Eisenhauer, A., Wallmann, K., Böhm, F., Fietzke, J., Liebetrau, V., Krabbenhöft, A., Farkaš, J., Tomašových, A. and Raddatz, J. (2014) The Phanerozoic δ 88/86 Sr record of seawater: New constraints on past changes in oceanic carbonate fluxes. *Geochim. Cosmochim. Acta* 128, 249-265.

Von Allmen, K., Nægler, T.F., Pettke, T., Hippler, D., Griesshaber, E., Logan, A., Eisenhauer, A. and Samankassou, E. (2010) Stable isotope profiles (Ca, O, C) through modern brachiopod shells of *T. septentrionalis* and *G. vitreus*: Implications for calcium isotope paleo-ocean chemistry. *Chem. Geol.* 269, 210-219.

Wallace, M.W., Hood, A. v. S., Fayle, J., Hordern, E.S., and O'Hare, T.F., 2019, Neoproterozoic marine dolomite hardgrounds and their relationship to cap dolomites: *Precambrian Research*, v. 328, p. 269–286, doi:10.1016/j.precamres.2019.04.026.

Wang, J., Jacobson, A.D., Zhang, H., Ramezani, J., Sageman, B.B., Hurtgen, M.T., Bowring, S.A., and Shen, S.-Z., (2019) Coupled $\delta^{44/40}\text{Ca}$, $\delta^{88/86}\text{Sr}$, and $^{87}\text{Sr}/^{86}\text{Sr}$ geochemistry across the end-Permian mass extinction event: *Geochimica et Cosmochimica Acta*, v. 262, p. 143–165, doi:10.1016/j.gca.2019.07.035.

Wang, J., Jacobson, A.D., Sageman, B.B., Hurtgen, M.T., (2020) Stable Ca and Sr isotopes support volcanically triggered biocalcification crisis during Oceanic Anoxic Event 1a: *Geology*, doi: 10.1130/G47945.1.

Wang, Y., Sadler, P.M., Shen, S.Z., Erwin, D.H., Zhang, Y.C., Wang, X.D., Wang, W., Crowley, J.L. and Henderson, C.M., 2014. Quantifying the process and abruptness of the end-Permian mass extinction. *Paleobiology*, 40(1), p.113.

Warren, J. (2000) Dolomite: occurrence, evolution and economically important associations. *Earth-Sci. Rev.* 52, 1-81.

Watkins, J.M., DePaolo, D.J. and Watson, E.B. (2017) Kinetic fractionation of non-traditional stable isotopes by diffusion and crystal growth reactions. *Rev. Mineral. Geochem.* 82, 85-125.

Wei, G.Y., vS Hood, A., Chen, X., Li, D., Wei, W., Wen, B., Gong, Z., Yang, T., Zhang, Z.-F. and Ling, H.-F. (2019) Ca and Sr isotope constraints on the formation of the Marinoan cap dolostones. *Earth Plan. Sci. Lett.* 511, 202-212.

Wignall, P. and Hallam, A. (1992) Anoxia as a cause of the Permian/Triassic mass extinction: facies evidence from northern Italy and the western United States. *Palaeogeogr. Palaeoclimatol. Palaeoecol.* 93, 21-46.

Wignall, P. and Hallam, A. (1993) Griesbachian (Earliest Triassic) palaeoenvironmental changes in the Salt Range, Pakistan and southeast China and their bearing on the Permo-Triassic mass extinction. *Palaeogeogr. Palaeoclimatol. Palaeoecol.* 102, 215-237.

Wignall, P.B. and Twitchett, R.J. (1996) Oceanic Anoxia and the End Permian Mass Extinction. *Science* 272, 1155-1158.

Woods, A.D., Bottjer, D.J., Mutti, M. and Morrison, J. (1999) Lower Triassic large sea-floor carbonate cements: Their origin and a mechanism for the prolonged biotic recovery from the end-Permian mass extinction. *Geology* 27, 645-648.

Xie, S., Pancost, R.D., Huang, J., Wignall, P.B., Yu, J., Tang, X., Chen, L., Huang, X. and Lai, X. (2007) Changes in the global carbon cycle occurred as two episodes during the Permian–Triassic crisis. *Geology* 35, 1083-1086.

Yang, H., Chen, Z., Wang, Y., Tong, J., Song, H. and Chen, J. (2011) Composition and structure of microbialite ecosystems following the end-Permian mass extinction in South China. *Palaeogeogr. Palaeoclimatol. Palaeoecol.* 308, 111-128.

Yang, J., Jansen, M.F., Macdonald, F.A., and Abbot, D.S., 2017, Persistence of a freshwater surface ocean after a snowball Earth: *Geology*, v. 45, p. 615–618, doi:10.1130/G38920.1.

Yin, H., Zhang, K., Tong, J., Yang, Z. and Wu, S. (2001) The global stratotype section and point (GSSP) of the Permian-Triassic boundary. *Episodes* 24, 102-114.

Yin, H., Jiang, H., Xia, W., Feng, Q., Zhang, N. and Shen, J. (2014) The end-Permian regression in South China and its implication on mass extinction. *Earth-Sci. Rev.* 137, 19-33.

Zeebe, R.E. (2012) History of seawater carbonate chemistry, atmospheric CO₂, and ocean acidification. *Annu. Rev. Earth Planet. Sci.* 40, 141-165.

Zhang, K., Tong, J., Yin, H. and Wu, S. (1996) Sequence stratigraphy of the Permian-Triassic boundary section of Changxing, Zhejiang. *Acta Geol. Sin.* 70, 270-281.

Zhao, X. and Tong, J. (2010) Two episodic changes of trace fossils through the Permian-Triassic transition in the Meishan cores, Zhejiang Province. *Sci. Chin. Earth Sci.* 53, 1885-1893.

Zheng, Q., Cao, C. and Zhang, M. (2013) Sedimentary features of the Permian-Triassic boundary sequence of the Meishan section in Changxing County, Zhejiang Province. *Sci. Chin. Earth Sci.* 56, 956-969.

Ziegler, A.M., Hulver, M.L., and Rowley, D.B. (1997) Permian world topography and climate, in Martini, I.P., ed., *Late glacial and postglacial environmental changes—Quaternary, Carboniferous-Permian and Proterozoic*. New York, Oxford University Press, p. 111–146.